



Eddy-current testing modeling of axisymmetric pieces with discontinuities along the axis by means of an integral equation approach

Konstantinos Pipis

► To cite this version:

Konstantinos Pipis. Eddy-current testing modeling of axisymmetric pieces with discontinuities along the axis by means of an integral equation approach. Electromagnetism. Université Paris Saclay (COmUE), 2015. English. NNT : 2015SACLIS176 . tel-01252801

HAL Id: tel-01252801

<https://theses.hal.science/tel-01252801>

Submitted on 8 Jan 2016

HAL is a multi-disciplinary open access archive for the deposit and dissemination of scientific research documents, whether they are published or not. The documents may come from teaching and research institutions in France or abroad, or from public or private research centers.

L'archive ouverte pluridisciplinaire **HAL**, est destinée au dépôt et à la diffusion de documents scientifiques de niveau recherche, publiés ou non, émanant des établissements d'enseignement et de recherche français ou étrangers, des laboratoires publics ou privés.

NNT : 2015SACLS176

**THESE DE DOCTORAT
DE L'UNIVERSITE PARIS-SACLAY,
préparée à l'Université Paris Sud**

ÉCOLE DOCTORALE N° 580
Sciences et technologies de l'information et de la communication

Spécialité de doctorat : Traitement du Signal et des Images

Par

M. Konstantinos Pipis

Modélisation du CND par courants de Foucault des pièces axisymétriques avec des discontinuités suivant l'axe à l'aide d'une formulation d'équation intégrale

Thèse présentée et soutenue à CEA DIGITEO, le 27 novembre 2015

Composition du Jury :

M. Antonello Tamburrino	Professeur, Università degli studi di Cassino e del Lazio Meridionale	Rapporteur
M. Gérard Granet	Professeur, Université Blaise-Pascal	Rapporteur
M. Theodoros Thodoulidis	Professeur, University of Western Macedonia	Examinateur
M. Thierry Sollier	Ingénieur Direction de la Sûreté des Réacteurs (IRSN)	Examinateur
M. Marc Lambert	Chargé de Recherche CNRS	Examinateur
M. Dominique Lesselier	Directeur de recherche CNRS	Directeur de thèse
M. Anastasios Skarlatos	Ingénieur-Chercheur, CEA LIST	Encadrant



Ίθάκη

Σὰ βγεῖς στὸν πηγαιμὸν γιὰ τὴν Ἰθάκη
νὰ εὕχεσαι ν̄αναι μακρὺς ὁ δρόμος
γεμάτος περιπέτειες, γεμάτος γνώσεις.

Τοὺς Λαιστρυγόνας καὶ τοὺς Κύκλωπας,
τὸν ψυμωμένο Ποσειδῶνα μὴ φοβᾶσαι,
τέτοια στὸν δρόμο σου ποτέ σου δὲν θὰ βρεῖς,
ἄν μέν' ἡ σκέψις σου ὑψηλή, ἄν εκλεκτὴ
συγκίνησις τὸ πνεῦμα καὶ τὸ σῶμα σου ἀγγί-
ζει.

Τοὺς Λαιστρυγόνας καὶ τοὺς Κύκλωπας,
τὸν ἄγριο Ποσειδῶνα δὲν θὰ συναντήσεις,
ἄν δὲν τοὺς κουβανεῖς μὲς στὴν ψυχή σου,
ἄν ἡ ψυχή σου δὲν τοὺς στήνει ἐμπρός σου.

Νὰ εὕχεσαι ν̄αναι μακρὺς ὁ δρόμος.
Πολλὰ τὰ καλοκαιρινὰ πρωιά νὰ εἰναι
ποὺ μὲ τί εὐχαρίστησι, μὲ τί χαρὰ
θὰ μπαίνεις σὲ λιμένας πρωτοειδομένους.

νὰ σταματήσεις σ' εμπορεῖα Φοινικικά,
καὶ τὲς καλὲς πραγμάτειες ν' ἀποκτήσεις,
σεντέφια καὶ κοράλλια, κεχριμπάρια κ' ἔβε-
νους,
καὶ ηδονικὰ μυρωδικὰ κάθε λογῆς,
ὅσο μπορεῖς πιὸ ἀφθονα ἡδονικα μυρωδικά.

Σὲ πόλεις Αἴγυπτιακὲς πολλὲς νὰ πᾶς,
νὰ μάθεις καὶ νὰ μάθεις ἀπ' τοὺς σπουδασμέ-
νους.

Πάντα στὸν νοῦ σου νάχεις τὴν Ἰθάκη.
Τὸ φθάσιμον ἔκει εἰν' ὁ προορισμὸς σου.

Ἄλλὰ μὴ βιάζεις τὸ ταξεῖδι διόλου.
Καλλίτερα χρόνια πολλὰ νὰ διαρκέσει·
καὶ γέρος πιὰ ν' ἀράξεις στὸ νησί,
πλούσιος μὲ ὅσα κέρδισες στὸν δρόμο,
μὴ προσδοκώντας πλούτη νὰ σε δώσῃ ἡ Ἰθά-
κη.

Ithaque

Lorsque tu mettras le cap sur Ithaque, fais de sorte que ton voyage soit long, plein d'aventures et d'expériences.

Les Lestrygons et les Cyclopes, et la colère de Poséidon ne crains, ils ne se trouveront point sur ton chemin si ta pensée reste élevée, si une émotion de qualité envahit ton esprit et ton corps.

Lestrygons, Cyclopes, et la fureur de Poséidon tu n'auras à affronter que si tu les portes en toi, si c'est ton âme qui les dresse devant toi.

Fais de sorte que ton parcours soit long. Que nombreux soient les matins o - avec quel délice et quelle joie! - tu découvriras des ports inconnus, des ports nouveaux pour toi,

et tu iras t'arrêter devant les échoppes Phéniciennes pour acquérir les belles marchandises nacres, coraux, ambres, ébènes et des parfums voluptueux, surtout beaucoup de parfums voluptueux;

et tu iras d'une ville Egyptienne à l'autre pour apprendre, et encore apprendre, de la bouche des savants. La pensée d'Ithaque ne doit pas te quitter. Elle sera toujours ta destination.

Mais n'écourt pas la durée du voyage. Il vaut mieux que cela prenne des longues années et que déjà vieux tu atteignes l'île, riche de tout ce que tu as acquis sur ton parcours et sans te dire qu'Ithaque t'amènera des richesses nouvelles.

Ἡ Ἰθάκη σ' ἔδωσε τ' ὥραῖο ταξεῖδι.
Χωρὶς αὐτὴν δὲν θᾶβγαινες στὸν δρόμο.
Ἄλλα δὲν ἔχει νὰ σε δώσει πιά.

Κι ἂν πτωχικὴ τὴν βρῆς, ἡ Ἰθάκη δὲν σε
γέλασε.
Ἐτσι σοφὸς ποὺ ἔγινες, μὲ τόση πείρα,
ἥδη θὰ τὸ κατάλαβες, ἡ Ἰθάκες τί σημαίνουν.

K.P. Καβάφης

Ithaque t'a offert le beau voyage. Sans elle,
tu n'aurais pas pris la route. Elle n'a plus
rien à te donner.

Et si tu la trouvais pauvre, Ithaque ne
t'a pas trompé. Sage à présent et plein
d'expérience, tu as certainement compris ce
que pour toi Ithaque signifie.

C.P. Cavafy

Remerciements

Je tiens à remercier ici tous les personnes qui ont contribué à la réalisation de cette thèse.

Tout d'abord, j'aimerais bien remercier Mme. Clarisse Poidevin, directrice du département (DISC), pour m'avoir accepté au département, où j'ai profité d'un environnement qui facilite la concentration à ma recherche.

Je remercie aussi M. Christophe Reboud, chef du laboratoire (LSME), qui m'a intégré dans le laboratoire et dont la disponibilité, le conseils et le support ont amélioré mon travail.

En outre, je voudrais exprimer mes remerciements au Pr. Dominique Lesselier qui a dirigé ma thèse. Ses conseils ont été toujours utiles et ils m'ont aidé à donné une importance à des aspects de la thèse que je sous-estimerais autrement comme secondaires. Je remercie aussi Pr. Theodoros Theodoulidis pour m'avoir encadré. Ses explications, en parlant toujours calmement et sans se dépêcher, m'ont beaucoup aidé et encouragé pendant tous les trois ans de cette thèse et notamment pendant mon séjour d'un mois à Kozani.

En plus, je tiens à remercier Mr. Anastassios Skarlatos, qui m'a encadré et conseillé quotidiennement. Sans ses explications patientes sur toutes mes questions mon travail serait totalement différent.

En fin, je remercie ma famille et mes amis Thenia, Akis, Efi, Giorgos, Ioanna, Anna, Audrey, François, Tomas, Vasso, et Zeta pour le soutien continu et parfois indispensable pendant ces trois ans.

Acknowledgements

I would like to thank everybody who has contributed either directly or indirectly to the realisation of this Ph.D. thesis.

I would like to thank Ms. Clarisse Poidevin, head of the department (DISC), for having given me the chance to carry out this work in the department, where I found a very supporting environment that allowed me to concentrate on my work.

I would also like to express my gratitude to Mr. Christophe Reboud, head of the laboratory (LSME), who integrated me in the laboratory, was always at my disposal and whose advice and support improved my work.

Furthermore, I express my thanks to Pr. Dominique Lesselier for supervising my Ph.D. thesis. His piece of advice was always useful for me, helping me to focus on important aspects of a Ph.D. which I would otherwise underestimate as secondary. I also thank Pr. Theodoros Theodoulidis for supervising my work. His guidance and explanations, speaking always calmly and never in a hurry, have been very useful and encouraging to me during the three years of my Ph.D. and especially during my one-month stay in Kozani.

I would also like to express my strong gratitude to Mr. Anastassios Skarlatos, for guiding me in a daily basis during all three years of this work. Without his scientifically complete and patient explanations on all of my queries this work would have been totally different.

Last but not least, I would address my thanks to my family and to my friends Thenia, Akis, Efi, Giorgos, Ioanna, Anna, Audrey, François, Tomas, Vasso and Zeta for their constant and sometimes indispensable support over all these three years.

Ευχαριστίες

Θα ήθελα να ευχαριστήσω όλους όσους βοήθησαν και συνέβαλαν στην ολοκλήρωση της διδακτορικής αυτής διατριβής.

Θα ήθελα πρωτίστως να ευχαριστήσω την κ. Κλαρις Πουαντεβάν, διευθύντρια του τμήματος (DISC), για τη δυνατότητα που μου παρείχε να διεξάγω τη διατριβή αυτή στο τμήμα, όπου έτυχα ενός περιβάλλοντος ιδανικού για την αποκλειστική συγκέντρωση σε ερευνητικές εργασίες.

Επίσης, θέλω να εκφράσω τις ευχαριστίες μου στον κ. Κριστόφ Ρεμπού, διευθυντή του εργαστηρίου (LSME), που με ενσωμάτωσε στο εργαστήριο, ήταν πάντοτε στη διάθεση μου και του οποίου οι συμβουλές και η υποστήριξη ήταν καθοριστικές για τη βελτίωση της εργασίας μου.

Επιπλέον, θέλω να εκφράσω την ευγνωμοσύνη μου στους δύο καθηγητές που επέβλεψαν και με καθοδήγησαν καθοριστικά κατά τη διδακτορική μου διατριβή: τον κ. Ντομινίκ Λεσελιέ, του οποίου οι συμβουλές και η καθοδήγηση εστίασαν σε όλα τα στοιχεία που συνθέτουν την πλήρη μαθητεία μίας διδακτορικής διατριβής, που διαφορετικά θα υποεκτιμούσα ως δευτερεύοντα, και τον κ. Θεόδωρο Θεοδουλίδη, του οποίου η ηρεμία στο λόγο με ενθάρρυνε ιδιαιτέρως καθόλη τη διάρκεια των τριών ετών της διατριβής και ιδιαιτέρως κατά τη διαμονή μου στην Κοζάνη.

Ιδιαίτερες ευχαριστίες θέλω επίσης να εκφράσω στον κ. Αναστάσιο Σκαρλάτο με τον οποίο εργάστηκα σε καθημερινή βάση όλα αυτά τα τρία χρόνια. Χωρίς τις πλήρεις και υπομονετικές του απαντήσεις και εξηγήσεις σε όλες μου τις δυσκολίες η εργασία αυτή θα ήταν εντελώς διαφορετική.

Τέλος, θέλω να ευχαριστήσω την οικογένεια μου, καθώς και τους φίλους μου Θένια, Άκη, Έφη, Γιώργο, Ιωάννα, Άννα, Οντρέ, Φρανσουά, Τόμας, Βάσω και Ζέτα για τη διαρκή και κάποιες φορές απαραίτητη υποστήριξη τους.

Contents

1	Introduction	1
1.1	Nondestructive testing	1
1.2	Eddy-current testing	2
1.3	ECT modelling in crack detection	2
1.4	Thesis structure	4
2	Electromagnetic foundation	7
2.1	Maxwell's equations	7
2.2	Boundary conditions	9
2.3	Second order vector potential	10
2.4	Separation of variables	11
2.5	Reciprocity theorem	13
2.6	Green's operator	14
3	Inspection of cylindrical geometries	17
3.1	Problem description	17
3.2	Primary field solution	18
3.2.1	Mathematical analysis	18
3.2.2	Excitation terms	26
3.2.3	Numerical treatment	27
3.2.4	Impedance change	28
3.2.5	Perspectives	29
3.3	Green's function	32
3.3.1	Electric dipole in conducting plate	32
3.3.2	Reflection of the radial interfaces	41
3.3.3	Numerical treatment	50
3.4	Eddy-current signal calculation	51
4	Numerical validations	55
4.1	Conducting plate with a borehole	55
4.1.1	Halfspace with a borehole and a crack	56
4.1.2	Plate with a borehole and a crack	58

4.2 Conducting tube	63
4.2.1 Flawless tube	64
4.2.2 Crack at the edge of the tube	66
5 Conclusion	69
5.1 Work recapitulation	69
5.2 Perspectives	70
6 Résumé	73
6.1 Introduction	73
6.2 Inspection des pièces cylindriques	74
6.2.1 Description du problème	74
6.2.2 Calcul du champ primaire	75
6.2.3 Fonction de Green	78
6.3 Signal courant de Foucault	84
6.4 Validations numériques	84
6.4.1 Demi-espace avec un alésage et un défaut	84
6.4.2 Plaque finie avec un alésage et un défaut	85
6.4.3 Tube infini avec un défaut à son bord	86
6.5 Conclusion	87

List of Figures

1.1	Cracks at the vicinity of rivet holes.	3
1.2	Steam generator tubes.	3
2.1	Surface with a charge density ρ_s or a surface current density J_s separating two media 1 and 2.	10
2.2	Probe excited with a $Ie^{j\omega t}$ current. The field in the domain in the presence of a conducting geometry C is \mathbf{E}' , \mathbf{H}'	14
2.3	Point source distribution in a volume V.	14
3.1	Inspection of a cylindrical conductor of different thickness and height with a cylindrical air inclusion and a crack at the vicinity of it. The inspection probe is located either over the work-piece or inside the air inclusion. . . .	17
3.2	ρ -z cross section of a semi-infinite tube.	19
3.3	Coil positions	27
3.4	Inspection of a tube of finite length by separating the problem in two subproblems with odd and even parity. The tube height is $2c$ and the $z = 0$ plane is a symmetry plane of the tube. The coils are symmetrically located on the two sides of the symmetry plane.	29
3.5	ρ -z cross section of a semi-infinite tube. Even parity.	30
3.6	Radial cross section of a tube of finite length. An electric dipole with φ orientation	32
3.7	Radial cross-section of a conducting plate of thickness $c_2 - c_1$, with an electric dipole of φ -orientation located at $(\rho', 0, z')$	33
3.8	Radial cross-section of an finite tube of thickness $b_2 - b_1$ and height $c_2 - c_1$. An initial field equal to this calculated in Section 3.3.1 is considered in region II.	42
3.9	Inspection of a conductor with a borehole and a crack breaking the wall of the borehole. The flaw surface is on the $\rho - z$ plane with a narrow azimuthal opening.	52
3.10	Crack discretisation in n cells.	53
3.11	Conical crack representation.	54
4.1	Half-space with borehole and a crack.	56

4.2	Impedance variation vs. coil position along a scan over the flawless work-piece.	57
4.3	Impedance variation owing to the crack in the presence of the borehole.	57
4.4	Impedance variation vs. coil position along a scan line passing above the borehole and the crack.	57
4.5	Simulation data for the real part vs. the imaginary part of the impedance variation due to the crack in the presence of the borehole. The coil is operated at 1 kHz.	58
4.6	2 mm-thick plate with borehole and a crack.	59
4.7	Impedance variation vs. coil position. The total signal simulated with VIM-SIM (circles) and SIM (solid line) as well as the hole signal as calculated with VIM-SIM (crosses) and SIM (dashed line) are illustrated.	59
4.8	Complex plane of the impedance variation due to the flawless piece and the piece with a crack at the vicinity of the borehole.	60
4.9	Complex plane representation of the impedance variation due to the crack in the presence of the borehole.	60
4.10	Theoretical and measured data for the impedance variation vs. coil position for the configuration of Table 6.2. The solid line represents the SIM results for the total signal, whereas the dashed line stands for the hole signal. The SIM results are compared against the measured signals in both cases (given by circle and cross markers, respectively).	62
4.11	Theoretical and measured data for the real part vs. the imaginary part of the impedance variation due to the crack in the presence of the borehole.	62
4.12	5mm-thick flawless tube.	64
4.13	Impedance variation vs. coil position along a scan line inside the flawless tube. The coil is operated at 1 kHz.	65
4.14	Impedance variation vs. coil position along a scan line inside the flawless tube. The coil is operated at 5 kHz.	65
4.15	Impedance variation vs. coil position along a scan line inside the flawless tube. The coil is operated at 10 kHz.	65
4.16	5 mm-thick tube with a 3 mm x 4 mm narrow crack located at the edge of the tube.	66
4.17	Impedance variation vs. coil position along a scan line inside the tube. The operation frequency is 1 kHz.	67
4.18	Impedance variation vs. coil position along a scan line inside the tube. The operation frequency is 5 kHz.	67
4.19	Impedance variation vs. coil position along a scan line inside the tube. The operation frequency is 10 kHz.	67
5.1	Model enhancement referring to the coils characteristics. Coil types (left), emission-reception coils (middle) and tilted coil (right).	70

5.2	Cross section of rivets. The rivet heads present an increasing diameter from the lower part to the top of the head.	70
5.3	Fastened rivet holes.	71
5.4	C-scan of a Rivet array.	71
5.5	Inspection of axially (left) and radially (right) stratified tubes.	71
6.1	Inspection d'une pièce cylindrique d'épaisseur axiale et radiale différentes avec une inclusion d'air et un défaut. Le capteur est localisé en dessus de la pièce inspectée ou dans l'inclusion d'air.	75
6.2	Coupe ρ - z d'un tube semi-infini.	76
6.3	Coupe radiale d'un tube fini. Un dipôle électrique d'orientation selon φ est situé dans le conducteur dans le tube.	78
6.4	Coupe radiale d'une plaque conductrice d'épaisseur $c_2 - c_1$ avec un dipôle électrique d'orientation selon φ situé à $(\rho', 0, z')$	79
6.5	Coupe radiale d'un tube fini d'épaisseur $b_2 - b_1$ et longueur $c_2 - c_1$. Le champ calculé dans le premier sous-problème est considéré comme un champ initial dans la région II.	81
6.6	Demi-espace avec un alésage et un défaut.	85
6.7	Variation de l'impédance vs. position du capteur suivant un scan sur l'ensemble alésage-défaut.	85
6.8	Plaque d'épaisseur 2 mm avec un alésage et un défaut.	85
6.9	Résultats de la méthode SIM et mesures expérimentales de la variation de l'impédance vs. la position du capteur pour la configuration de Table 6.2. La courbe pleine représente les résultats de SIM pour le signal total, la ligne pointillée correspond au signal de l'alésage. Les résultats de SIM sont comparés avec des résultats expérimentaux dans les deux cas (cercles et croix, respectivement).	86
6.10	Tube d'épaisseur 5 mm avec un défaut fin de dimensions 3 mm x 4 mm situé au bord du tube.	87
6.11	Variation de l'impédance vs. position du capteur suivant un scan dans le tube. La fréquence opérationnelle est 10 kHz.	87

Chapter 1

Introduction

1.1 Nondestructive testing

Nondestructive testing (NDT) refers, according to the American Society for Nondestructive Testing (ASNT), to the process of inspecting, testing, or evaluating materials, components or assemblies for discontinuities, or differences in characteristics without destroying the service ability of the part or system. In other words, when the inspection or test is completed the part or system can still be used.

The first attempts to apply nondestructive techniques in industry was a law passed in Connecticut in mid-nineteenth century imposing visual testing of boilers as well as the "Oil and Whitting" method of crack detection used in railroad industry in late nineteenth-early twentieth century in order to detect cracks in heavy steel parts. Since these attempts, which were the precursors of the methods used nowadays, NDT has been widely developed and used in the industry for quality control or material characterisation.

Nowadays, NDT comprises a number of general test categories according to their scientific principle. There are seven major test methods that are most frequently used: Magnetic Particle Testing, Liquid Penetrant Testing, Radiographic Testing, Ultrasonic Testing, Electromagnetic Testing, Visual Testing and Thermal/Infrared Testing.

Electromagnetic testing is a general test method that includes in particular Eddy Current testing, Alternating Current Field Measurement, Magnetic Flux Leakage and Remote Field testing. While magnetic particle testing is also an electromagnetic technique, due to its widespread use it is considered as a different NDT method rather than an electromagnetic testing technique. All of these techniques use the induction of an electric current or magnetic field into a conductive part, then the resulting effects are recorded and evaluated.

1.2 Eddy-current testing

Eddy-current testing (ECT) is a nondestructive method that uses the induction phenomenon, according to which an alternating current induces an electric current in a conducting piece around the magnetic field, the so-called eddy-currents, like a magnetic field is generated around an electric current.

Therefore, the principle of this method is described by the following phenomenon. An alternating current coil generates a magnetic field, the so-called primary field in the vicinity of the coil. Eddy-currents are created around the magnetic flux in the inspected piece, which in their own turn generate a secondary magnetic field that opposes the primary field. The value of the impedance measured in the presence of the inspected piece and far from any discontinuity of it is usually the reference impedance value. When the eddy-currents encounter a discontinuity in the inspected piece, the current density is affected and this change is reflected in the secondary magnetic field and it is finally detected as an impedance change of the coil. Thus, a discontinuity of the test-piece can be detected and characterised.

The eddy-current method is used in detecting and sizing of defects in test-pieces, measuring the electrical and geometrical properties of pieces, etc. The operation frequencies of this method vary within a range from 100Hz to 10MHz that is defined by the desired penetration of the field in the inspected piece.

Industrial applications of this method can be found in aeronautics, nuclear technology, petrochemical industry, metallurgy, etc. An important advantage is the simple and easily transportable instrumentation and, as a consequence, this makes it an economic method.

An important branch of the research in this method is modelling the signals produced in crack detection. Rapid and accurate models are needed in order to assist the controls performed with this method, the development and optimisation of new probes, the calculation of probability of detection (POD) curves or the solution of the inverse problem.

1.3 ECT modelling in crack detection

Crack detection is a major NDT application in industry. Quality control of parts as well as security standards imposed in all sectors of human activities, such as in industry, transportation, etc., demand accurate and rapid models of inspection.

Important research has been carried out on ECT modelling owing to the importance of the industrial applications which has led to the development of several models so far. The principal task of an ECT model consists in calculating the probe signal due to a defect, may the defect be fatigue cracks, stress corrosion cracks or corrosion pitting. The measured signal can be the impedance variation in case of a coil or the magnetic field change at the probe location when magnetic sensors (Hall effect, GMR, etc.) are used.

Two major model categories frequently used for such geometries are the Finite Element

Method (FEM) models and the Integral Equation Method (IM) models. Both models present different advantages and disadvantages. On the one hand, the main advantage of IM models is the computational efficiency that they provide. The computational time of the IM models is considerably smaller compared to the FEM models, which are generally slow. On the other hand, IM models cannot provide a solution for complex geometries of the test-pieces, which, on the other hand, can be achieved with FEM models.

FEM models divide the domain of the problem in a number of subdivisions, the finite elements. Next, the solution of the eddy-current problem in each element leads to a set of element equations which, recombined in a global equation system of all the element equations, gives the total solution of the eddy-current problem. Several works have treated the eddy-current problem with FEM [AR97].

The Volume Integral Method (VIM) in the context of ECT was introduced in [Dun85] and verified in several works afterwards [Dun88][SPL⁺08] models a flaw as a distribution of electric dipoles within the flaw volume. The electric field is determined by an integral equation relating the field due to an electric dipole to the total field due to the entire flaw. When the flaw is a crack with a very narrow opening compared to the size of the probe and the skin depth it can be modelled as a surface distribution of electric dipoles as proposed in [Bow94]. This limiting case of the general volumetric cracks is treated with the Surface Integral Method (SIM), which requires the integration over the surface of the flaw instead of a volume [BTXJ12][KA04][KA09][PL06][The10, MRT⁺13].

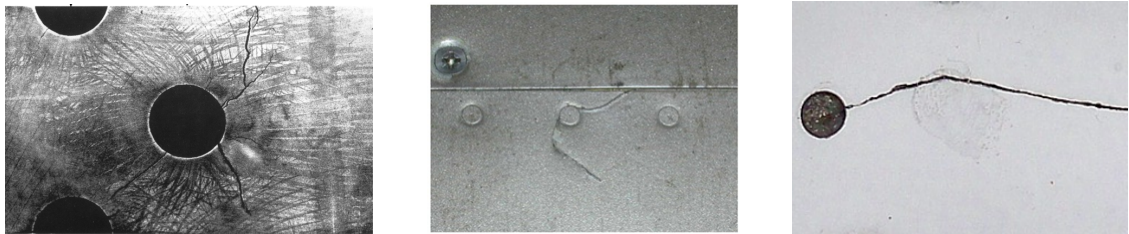


Figure 1.1: Cracks at the vicinity of rivet holes.



Figure 1.2: Steam generator tubes.

IM models require the construction of a Green's kernel dedicated to the flawless piece in order to solve the integral equation attributed to the problem. The present work deals with the modelling of cylindrical geometries inspection that are affected by narrow cracks.

Cracks often develop at the vicinity of aircraft rivets (Fig. 1.1) or at the edges of tubes (Fig. 1.2). These two limiting cases are examined as application cases. The interest in

both applications has been demonstrated by a number of recent contributions as sketched below.

As far as the fastener holes are concerned, studies have been carried out during the past years both at experimental [YZD⁺12][KLL14] and simulation level [MRTV08]. Furthermore, [KA04][KA09, PCP⁺08] handle the problem of a crack next to a fastener hole using the VIM, whereas [BTXJ12][BT09] model it with SIM. Additionally, [MRT⁺14b] proposes an hybrid integral equation approach, which uses the VIM in order to treat the fastener hole and applies the SIM to model the contribution of the crack. This is the so-called VIM-SIM model, which has led to improved computational efficiency.

In the present work an integral equation approach is presented, where the crack is modelled using SIM using a Green's kernel that takes into account the presence of the borehole, following the procedure proposed in [BTP12]. The truncated region eigenfunction expansion (TREE) method will be used for the derivation of the Green's kernel [TK06]. This method is a powerful tool for producing semi-analytical solutions and it will be presented thoroughly later in this manuscript. Finally, the contribution of the hole itself (in the absence of a crack) is determined as proposed in [ST15] or following the procedure of [TB08] extended in order to take into account tubular test-pieces.

1.4 Thesis structure

This thesis is organised in five chapters. A summary of each following chapter is proposed below.

Chapter 2 gives a brief overview of some electromagnetic and mathematical prerequisites, which are important for the analysis presented in the next chapters. First, a short presentation of the Maxwell's equations and the conditions of the field applied at the boundary between two media is given. The notion of the second order vector potential is introduced and a demonstration of the separation of variables method comes after. Furthermore, a presentation of the reciprocity theorem is given and a brief reference to the Green's operator notion is done to close the chapter.

In Chapter 3 a thorough analysis of the proposed model for the inspection of cylindrically layered geometries is given. The analysis is carried out in three steps. The first step consists in the analysis of the induction problem solution. Thus, the electromagnetic problem for a coil excited with an alternating current and located in a tubular test-piece is solved and the coil impedance change due to the presence of the test-piece is calculated. In the second step, the Green's function for this geometry, considering a dipole located in the conductor, is constructed. Finally, the integral equation solution in order to calculate the ECT signal is demonstrated.

In Chapter 4 the results for two applicative cases of the model are given: the ECT signal calculated for the case of a conducting plate with a borehole and a crack at the vicinity of the borehole and for the case of a conducting tube with an edge-crack is com-

pared with simulations of the FEM and the VIM-SIM models as well as with experimental measurements in order to validate the model.

Finally, the thesis concludes in Chapter 5 with a recapitulation of the work presented, and some perspectives for future improvements and developments are proposed.

Chapter 2

Electromagnetic foundation

Several electromagnetic and mathematical tools are frequently used in this work. The goal of this chapter is to briefly present and summarise the most important ones in order for the reader to recall or consult them when needed in this manuscript. First, Maxwell's equations and the boundary conditions between two media are presented. Afterwards, the second order vector potential is introduced, and the Helmholtz equation is formally solved using the method of separation of variables. Finally, the chapter concludes with a brief overview of the reciprocity theorem and the Green's operator.

2.1 Maxwell's equations

Before Maxwell's work the theoretical concepts of electrodynamics were described by equations [Str41]

$$\nabla \cdot \mathbf{D}(\mathbf{r}, t) = \rho(\mathbf{r}, t) \quad (\text{Gauss law}) \quad (2.1)$$

$$\nabla \cdot \mathbf{B}(\mathbf{r}, t) = 0 \quad (2.2)$$

$$\nabla \times \mathbf{E}(\mathbf{r}, t) = -\frac{\partial}{\partial t} \mathbf{B}(\mathbf{r}, t) \quad (\text{Faraday law}) \quad (2.3)$$

$$\nabla \times \mathbf{H} = \mathbf{J}(\mathbf{r}, t) \quad (\text{Ampere law}), \quad (2.4)$$

where \mathbf{D} is the electric displacement, \mathbf{E} is the electric field, \mathbf{B} the magnetic flux density, \mathbf{H} the magnetic field, \mathbf{J} the current density and ρ the volumetric charge density.

These equations seemed to be validated by any usual electromagnetic experiment in magnetostatics. However, the Ampere law did not respect the mathematical rule that suggests a zero divergence of a vector curl. In order to correct the Ampere law, Maxwell added the displacement current term $\frac{\partial}{\partial t} \mathbf{D}(\mathbf{r}, t)$, which finally transformed the equations

(2.1) - (2.4) into what we now call Maxwell's equations

$$\nabla \cdot \mathbf{D}(\mathbf{r}, t) = \rho(\mathbf{r}, t) \quad (2.5)$$

$$\nabla \cdot \mathbf{B}(\mathbf{r}, t) = 0 \quad (2.6)$$

$$\nabla \times \mathbf{E}(\mathbf{r}, t) = -\frac{\partial}{\partial t} \mathbf{B}(\mathbf{r}, t) \quad (2.7)$$

$$\nabla \times \mathbf{H}(\mathbf{r}, t) = \mathbf{J}(\mathbf{r}, t) + \frac{\partial}{\partial t} \mathbf{D}(\mathbf{r}, t). \quad (2.8)$$

Maxwell's theory was validated by Hertz's experiments on the electromagnetic waves transmission. However, for very low frequencies, the quasi-static approximation allows to neglect the displacement current term and, in this case, (2.1) - (2.4) form an approximation of Maxwell's equations.

Eqs. (2.5)-(2.8) are completed by the constitutive equations

$$\mathbf{D}(\mathbf{r}, t) = \varepsilon(\mathbf{r}, t) \mathbf{E}(\mathbf{r}, t) \quad (2.9)$$

$$\mathbf{B}(\mathbf{r}, t) = \mu(\mathbf{r}, t) \mathbf{H}(\mathbf{r}, t), \quad (2.10)$$

where ε is the permittivity and μ the permeability of the medium.

Additionally, the continuity equation and the equation relating the current density and the electric field are cited below

$$\nabla \cdot \mathbf{J} + \rho(\mathbf{r}, t) = 0 \quad (2.11)$$

$$\mathbf{J}(\mathbf{r}, t) = \sigma(\mathbf{r}, t) \mathbf{E}(\mathbf{r}, t), \quad (2.12)$$

where σ is the conductivity of the isotropic medium.

It can be noticed that for a linear, time-invariant and isotropic medium $\varepsilon(\mathbf{r}) = \varepsilon = \varepsilon_0 \varepsilon_r$, $\mu(\mathbf{r}) = \mu = \mu_0 \mu_r$ and $\sigma(\mathbf{r}) = \sigma$, where ε_0 and μ_0 are the permittivity and permeability of air, respectively, whereas ε_r and μ_r are the relative permittivity and permeability, respectively. In this thesis we work exclusively with linear and isotropic media. Hence, the notation ε and μ will be directly used from now on.

Furthermore, use of complex forms is more convenient when we deal with alternating electromagnetic field. Let us denote the time-harmonic expression of the electric and magnetic field by

$$\mathbf{E}(\mathbf{r}, t) = \Re(\mathbf{E}(\mathbf{r}) e^{j\omega t}) \quad (2.13)$$

$$\mathbf{H}(\mathbf{r}, t) = \Re(\mathbf{H}(\mathbf{r}) e^{j\omega t}), \quad (2.14)$$

where ω is the angular frequency. In this work, the analysis is presented in the time-

harmonic regime, in which Maxwell's equations are expressed as

$$\nabla \cdot \mathbf{D}(\mathbf{r}) = \rho(\mathbf{r}) \quad (2.15)$$

$$\nabla \cdot \mathbf{B}(\mathbf{r}) = 0 \quad (2.16)$$

$$\nabla \times \mathbf{E}(\mathbf{r}) = -j\omega \mathbf{B}(\mathbf{r}) \quad (2.17)$$

$$\nabla \times \mathbf{H} = \mathbf{J}(\mathbf{r}) + j\omega \mathbf{D}(\mathbf{r}) \quad (2.18)$$

and the constitutive equations take the form

$$\mathbf{D}(\mathbf{r}) = \epsilon(\mathbf{r})\mathbf{E}(\mathbf{r}) \quad (2.19)$$

$$\mathbf{B}(\mathbf{r}) = \mu(\mathbf{r})\mathbf{H}(\mathbf{r}). \quad (2.20)$$

2.2 Boundary conditions

\mathbf{E} , \mathbf{D} , \mathbf{B} , \mathbf{H} and \mathbf{J} are, in general, discontinuous at the boundary of two different media 1 and 2 or at a surface with a charge density ρ_s or a surface current density J_s (Fig. 2.1). The relations of the fields at such a boundary read [Gri99, Bal89]

$$\mathbf{n} \times (\mathbf{E}_2 - \mathbf{E}_1) = 0 \quad (2.21)$$

$$\mathbf{n} \times (\mathbf{H}_2 - \mathbf{H}_1) = \mathbf{J}_s \quad (2.22)$$

$$\mathbf{n} \cdot (\mathbf{D}_2 - \mathbf{D}_1) = \rho_s \quad (2.23)$$

$$\mathbf{n} \cdot (\mathbf{B}_2 - \mathbf{B}_1) = 0 \quad (2.24)$$

$$\mathbf{n} \cdot (\mathbf{J}_2 - \mathbf{J}_1) = -j\omega\rho_s, \quad (2.25)$$

where the subscripts 1,2 denote the two different media, \mathbf{n} is a unit vector normal to the surface between the two media with direction from medium 1 to medium 2. Eqs. (2.21) and (2.22) express the discontinuity of the field components tangential to the boundary, whereas (2.23) and (2.24) describe the discontinuity of the normal components. Eq. (2.25) derives from the charge conservation principle and corresponds to the continuity equation (2.11).

The surface current density is always zero, unless the conductivity in one of the two media is considered infinite. Additionally, the surface charge density is never zero, unless

$$\frac{\sigma_1}{\sigma_2} = \frac{\epsilon_1}{\epsilon_2} \quad (2.26)$$

as it occurs from (2.23) and (2.25).

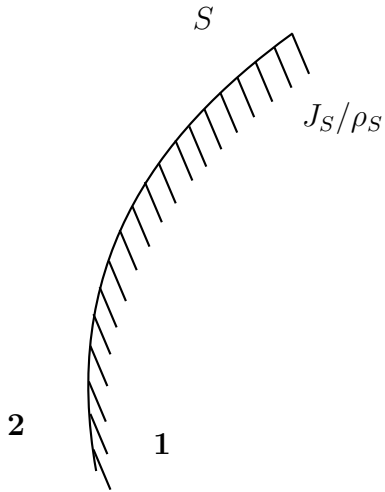


Figure 2.1: Surface with a charge density ρ_s or a surface current density J_s separating two media 1 and 2.

2.3 Second order vector potential

The solution of many electromagnetic problems can be significantly simplified by introducing the scalar potential ψ and the magnetic vector potential \mathbf{A} [Jac98] so as

$$\mathbf{B} = \nabla \times \mathbf{A} \quad (2.27)$$

and

$$\mathbf{E} = -\nabla\psi - \frac{\partial\mathbf{A}}{\partial t}. \quad (2.28)$$

\mathbf{A} is chosen to be divergence free. Furthermore, \mathbf{E} must satisfy the Helmholtz equation $\nabla^2\mathbf{E}(\mathbf{r}) + k^2\mathbf{E}(\mathbf{r}) = 0$, which for non-conductive regions ($k = 0$) transforms to the Laplace equation $\nabla^2\mathbf{E}(\mathbf{r}) = 0$. Consequently, the potentials ψ and \mathbf{A} must satisfy the Laplace and the Helmholtz equation, respectively. As far as the continuity of the field is concerned, one needs to specify at the interfaces of interest all three scalar components expressions of a vector field and thus, of the vector potential that expresses it. However, this work treats cylindrical geometries and thus, the analysis is carried out in the cylindrical coordinate system, where the components of the magnetic vector potential are coupled and cannot yield separated Helmholtz equations for each component. In order to overcome this difficulty a second order vector potential (SOVP) \mathbf{W} is introduced [TK06] related to the magnetic vector potential by

$$\mathbf{A} = \nabla \times \mathbf{W}. \quad (2.29)$$

The second order potential in the case of cylindrical coordinates reads as $\mathbf{W} = W_a \hat{\mathbf{z}} + \hat{\mathbf{z}} \times \nabla W_b$, where W_a corresponds to the transverse electric (TE) solution and W_b to the

transverse magnetic (TM) solution. W_a and W_b satisfy the Helmholtz equation

$$\frac{\partial^2 W_{a,b}}{\partial \rho^2} + \frac{1}{\rho} \frac{\partial W_{a,b}}{\partial \rho} + \frac{1}{\rho^2} \frac{\partial^2 W_{a,b}}{\partial \varphi^2} + \frac{\partial^2 W_{a,b}}{\partial z^2} = k^2 W_{a,b} ; \quad k^2 = j\omega\mu_0\sigma. \quad (2.30)$$

Additionally, a TEM term may appear which satisfies the Laplace equation

$$\frac{\partial^2 W_{TEM}}{\partial \rho^2} + \frac{1}{\rho} \frac{\partial W_{TEM}}{\partial \rho} + \frac{1}{\rho^2} \frac{\partial^2 W_{TEM}}{\partial \varphi^2} + \frac{\partial^2 W_{TEM}}{\partial z^2} = 0. \quad (2.31)$$

By definition of the potentials \mathbf{W} and \mathbf{A} the magnetic flux density is now expressed as $\mathbf{B} = \nabla \times \nabla \times \mathbf{W}$. The components of the field are written as follows:

$$B_\rho = \frac{k^2}{\rho} \frac{\partial W_b}{\partial \varphi} + \frac{\partial^2 W_a}{\partial \rho \partial z} \quad (2.32)$$

$$B_\varphi = -k^2 \frac{\partial W_b}{\partial \rho} + \frac{1}{\rho} \frac{\partial^2 W_a}{\partial \varphi \partial z} \quad (2.33)$$

$$B_z = -k^2 W_a + \frac{\partial^2 W_a}{\partial z^2} \quad (2.34)$$

$$E_\rho = -j\omega \left[\frac{1}{\rho} \frac{\partial W_a}{\partial \varphi} - \frac{\partial^2 W_b}{\partial \rho \partial z} \right] \quad (2.35)$$

$$E_\varphi = -j\omega \left[-\frac{\partial W_a}{\partial \rho} - \frac{1}{\rho} \frac{\partial^2 W_b}{\partial \varphi \partial z} \right] \quad (2.36)$$

$$E_z = -j\omega \left[k^2 W_b - \frac{\partial^2 W_b}{\partial z^2} \right]. \quad (2.37)$$

Regarding (2.32)-(2.37), in the non-conducting regions ($\sigma = 0$) the expression of the magnetic flux density reduces to the expression

$$\mathbf{B} = \nabla \left(\frac{\partial W_a}{\partial z} \right). \quad (2.38)$$

A scalar potential $\phi = \frac{\partial W_a}{\partial z}$ can be introduced for the expression of the field in these regions. Thus, the magnetic flux density in air regions reads $\mathbf{B} = \nabla \phi$, where ϕ satisfies the Laplace equation.

2.4 Separation of variables

With the introduction of the SOVP the electromagnetic problem is scalarised by means of two scalar potentials. Hence, (2.30) and (2.31) can be solved using the method of separation of variables as follows.

The general form of the Helmholtz equation is

$$\left(\frac{\partial^2}{\partial \rho^2} + \frac{1}{\rho} \frac{\partial}{\partial \rho} + \frac{1}{\rho^2} \frac{\partial^2}{\partial \varphi^2} + \frac{\partial^2}{\partial z^2} - k^2 \right) w = 0, \quad (2.39)$$

where the scalar function $w(\rho, \varphi, z)$ stands for the potentials W_a, W_b and ϕ . According to the separation of variables method, w is expressed as

$$w(\rho, \varphi, z) = R(\rho)\Phi(\varphi)Z(z). \quad (2.40)$$

The solution of (2.39) can be decomposed into the solution of three ordinary differential equations:

$$\left(\frac{d^2}{dz^2} - \mu^2 \right) Z(z) = 0 \quad (2.41)$$

$$\left(\frac{d^2}{d\varphi^2} - \nu^2 \right) \Phi(\varphi) = 0 \quad (2.42)$$

$$\left[\frac{d}{d\rho} \left(\rho \frac{d}{d\rho} \right) + \rho \left(-k^2 + \mu^2 + \frac{\nu^2}{\rho^2} \right) R(\rho) \right] = 0, \quad (2.43)$$

one for each coordinate. μ and ν are two arbitrary constants.

(2.41) has the general solution

$$Z(z) = A_1 e^{\mu z} + A_2 e^{-\mu z}, \quad (2.44)$$

where A_1, A_2 are arbitrary constants. An equivalent solution of (2.44) reads

$$Z(z) = A_1 \cosh(\mu z) + A_2 \sinh(\mu z). \quad (2.45)$$

Replacing $\mu = jm$, $m \in \mathbb{Z}$ the following form is obtained

$$Z(z) = A_1 \cos(mz) + A_2 \sin(mz). \quad (2.46)$$

It is noticed that the notation A_1 and A_2 is used in all (2.44) - (2.46) for sake of economy. Nonetheless, they bear not the same values for every solution.

Similarly the solutions of (2.42) can be written as

$$\Phi(\varphi) = B_1 e^{\nu\varphi} + B_2 e^{-\nu\varphi}, \quad (2.47)$$

$$\Phi(\varphi) = B_1 \cosh(\nu\varphi) + B_2 \sinh(\nu\varphi). \quad (2.48)$$

$$\Phi(\varphi) = B_1 \cos(n\varphi) + B_2 \sin(n\varphi). \quad (2.49)$$

where B_1, B_2 are again arbitrary constants and $\nu = jn$. In many problems with cylindrical configurations there is azimuthal symmetry $\Phi(\varphi + 2\pi) = \Phi(\varphi)$. This symmetry requires

$\nu \in \mathbb{I}$. In case of azimuthal symmetry (2.43) is transformed in

$$\left[\frac{d}{d\rho} \left(\rho \frac{d}{d\rho} \right) + \rho(\beta^2 \rho^2 - n^2) R(\rho) \right] = 0, \quad (2.50)$$

with $\beta = \sqrt{-k^2 + \mu^2}$.

The solution of (2.50) is a linear superposition of Bessel functions

$$R(\rho) = C_1 J_n(\beta\rho) + C_2 Y_n(\beta\rho), \quad (2.51)$$

or Hankel functions

$$R(\rho) = C_1 H_n^{(1)}(\beta\rho) + C_2 H_n^{(2)}(\beta\rho), \quad (2.52)$$

or modified Bessel functions when β is purely imaginary. Consequently, a general solution of the Helmholtz equation is given as

$$W_{a,b} = \sum_{\nu} \sum_m (A_1 e^{jm\varphi} + A_2 e^{-jm\varphi}) [B_1 \cosh(\nu z) + B_2 \sinh(\nu z)] [C_1 J_n(\beta\rho) + C_2 Y_n(\beta\rho)]. \quad (2.53)$$

This solution assumes a finite region. In case of infinite solution region the sum over ν should be replaced by an integral.

2.5 Reciprocity theorem

The reciprocity of the electromagnetic field plays a key role in the function of detection systems as it defines the electromagnetic behaviour of a scatterer when the emission and reception positions are interchanged. A necessary condition for a correct solution of any electromagnetic problem is the satisfaction of the reciprocity principle described by the Lorentz reciprocity relation

$$\nabla \cdot (\mathbf{E} \times \mathbf{H}' - \mathbf{E}' \times \mathbf{H}) = 0, \quad (2.54)$$

where \mathbf{E}, \mathbf{H} and \mathbf{E}', \mathbf{H}' are two arbitrary solutions of the Maxwell's equations. In the context of this work the emitter of the electromagnetic field is a probe and the inspected geometry is the scatterer. Beginning with (2.54) the impedance change ΔZ of the probe due to the presence of a conductor (scatterer) can be calculated from the relation [AMW81]

$$\Delta Z = \frac{1}{I^2} \oint_S (\mathbf{E} \times \mathbf{H}' - \mathbf{E}' \times \mathbf{H}) \cdot \hat{\mathbf{n}} dS, \quad (2.55)$$

where I is the rms value of the probe excitation current, \mathbf{E} , \mathbf{H} are the electric and magnetic field in the absence of the conductor and \mathbf{E}' , \mathbf{H}' are the corresponding fields in the presence of the conductor. The integration is performed over a surface S that encloses the probe and $\hat{\mathbf{n}}$ is the unit vector normal to S pointing outwards (Fig. 2.2).

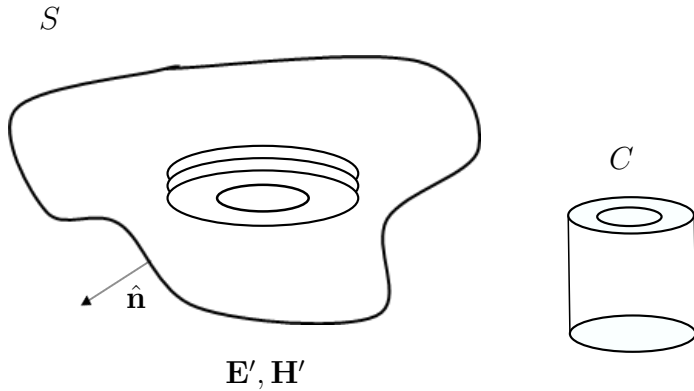


Figure 2.2: Probe excited with a $Ie^{j\omega t}$ current. The field in the domain in the presence of a conducting geometry C is \mathbf{E}', \mathbf{H}' .

2.6 Green's operator

An electric-electric Green's operator $\bar{\mathbf{G}}$ is a tensor that relates the electric field (\mathbf{E}) to a vector point electric source (\mathbf{J}). Each element of this tensor is an electric-electric Green's function. If the Green's function of a point source is known, then the field due to a finite source (Fig. 2.3) can be obtained by application of the linear superposition principle. The radiation of a point source that oscillates according to the harmonic convention $e^{j\omega t}$ at the position (\mathbf{r}) in an unbounded, homogeneous medium is written with the general form [Che95]

$$g(\mathbf{r}, \mathbf{r}') = \frac{e^{-jk|\mathbf{r}-\mathbf{r}'|}}{4\pi|\mathbf{r}-\mathbf{r}'|}, \quad (2.56)$$

considering that the source is located at \mathbf{r}' . The electrical properties of the medium are incorporated in the wave number $k = \omega/c = \omega\sqrt{\mu\epsilon}$, which also contains the information for the oscillation frequency of the source. Then, the solution of the wave equation

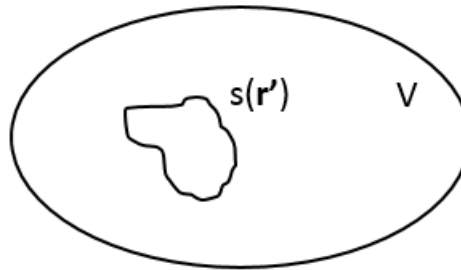


Figure 2.3: Point source distribution in a volume V .

$(\nabla^2 + k^2)\psi(\mathbf{r}) = s(\mathbf{r})$ considering a point source distribution $s(\mathbf{r})$ is calculated, by taking (2.56) into account, as

$$\psi(\mathbf{r}) = - \int_V g(\mathbf{r}, \mathbf{r}') s(\mathbf{r}') d\mathbf{r}'. \quad (2.57)$$

Eq. (2.56) can be used to calculate the dyadic Green's function in a homogeneous, isotropic medium which reads

$$\bar{\mathbf{G}}(\mathbf{r}, \mathbf{r}') = \left[\bar{\mathbf{I}} + \frac{\nabla' \nabla'}{k^2} \right] g(\mathbf{r}, \mathbf{r}') \quad (2.58)$$

Similarly, the Green's function for media with different geometries can be constructed. It is noticed that Green's functions for simple geometries have only been derived so far. In this work we expand the cases where we can derive an analytical expression of the Green's operator for cylindrically symmetric geometries. More precisely, we deal with homogeneous, cylindrically symmetric, conductive media. Moreover, we are interested in the φ -component of \mathbf{E} radiated by an electric dipole in the φ -direction. To be specific, we are limiting our work to the derivation of the $\bar{\mathbf{G}}^{\varphi\varphi}$ component of the Green's dyad.

Chapter 3

Inspection of cylindrical geometries

3.1 Problem description

In this chapter the analysis of the eddy-current problem for conducting, cylindrically layered geometries is presented. Fig. 6.1 shows the general configuration of the treated problem

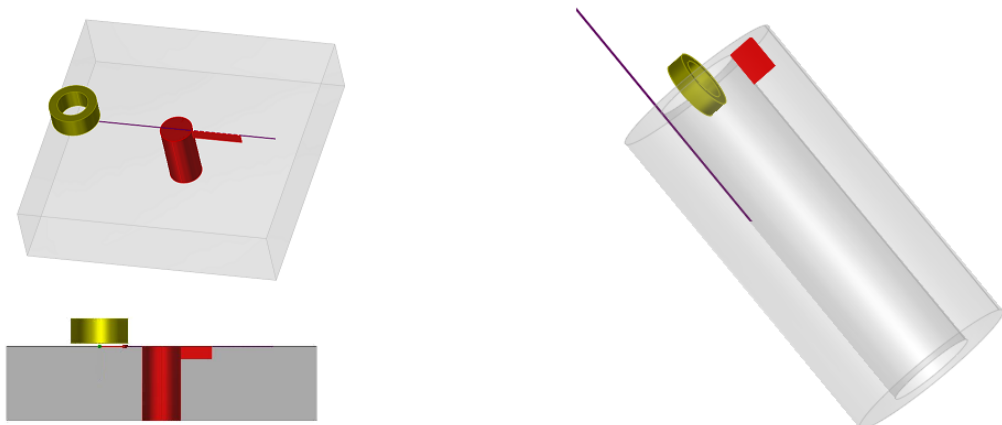


Figure 3.1: Inspection of a cylindrical conductor of different thickness and height with a cylindrical air inclusion and a crack at the vicinity of it. The inspection probe is located either over the work-piece or inside the air inclusion.

The geometry consists of a conducting, non-magnetic, cylindrical work-piece with a cylindrical air inclusion. The work-piece is homogeneous with conductivity σ and permeability equal to the permeability of air μ_0 . A thin crack is located in the conducting part of the work-piece. A thin crack is defined as a flaw of a very small opening compared to the size of the probe and the skin depth, which acts as a perfect current barrier [Bow94, BNH94]. This allows the representation of the flaw behaviour by a surface distribution of electric dipoles when eddy-currents are induced in the work-piece. The geometry is inspected by a single-coil probe excited by harmonic current $Ie^{j\omega t}$, which scans over the work-piece or in the borehole.

The solution of the eddy-current problem consists in calculating the eddy-current

signal, namely the impedance change of the coil for different positions with respect to the inspected work-piece. This is achieved in three different steps.

The first step is the solution of the induction problem in the absence of the crack. In this step the eddy-current field in the flawless piece due to the induction coil is calculated. Additionally, the impedance change of the coil due to this flawless piece is calculated for different positions of the coil. This change records the effect of geometrical discontinuities of the test-piece, i.e. a borehole or the edge of a tube. The second step concerns the construction of the Green's function corresponding to the inspected geometry. Finally, in the third step the integral equation associated to the eddy-current problem examined is solved and the coil impedance variation due to the defect is calculated using the reciprocity theorem.

3.2 Primary field solution

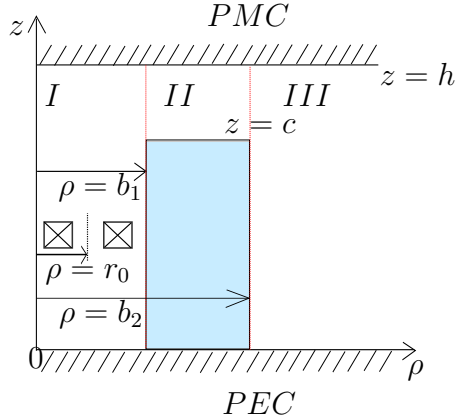
3.2.1 Mathematical analysis

The solution of the primary field problem is the first task towards the simulation of the eddy-current inspection. The goal of this step is the calculation of the primary field in the flawless piece in order to apply an integral equation formulation. Furthermore, in this step the impedance change due to the discontinuities of the piece is calculated.

In the recent years, research has been carried out on the primary field problem for several geometries [ST15, ST12, TB08, BT06]. [ST15] presents a modal solution of the induction problem for a conducting, non-magnetic, finite-thickness plate containing a cylindrical hole, when a coil moves above the piece. In this section a modal solution for the case of a semi-infinite cylindrical tube of inner radius b_1 and outer radius b_2 is presented for a coil inside the borehole. The truncation eigenfunction expansion (TREE) [TK06] approach is used. The TREE technique uses the rapid decrease of the field in order to truncate the region of interest at a distance where the field is seen as negligible enough. The truncation allows the expression of the field as a modal expansion with a discrete spectrum of modes rather than a continuous span that would occur in the case of an unbounded domain.

It is noted that the following analysis is also applicable for a semi-infinite plate with a borehole, provided that a sufficiently thick tube is considered with respect to the penetration depth ($b_2 - b_1 \gg \delta$, where δ is the penetration depth).

Fig. 6.2 shows a cross-section of the tube in the $\rho - z$ plane. An offset coil of inner and outer radius r_a and r_b , respectively, height H_c and N number of turns scans in the hole. The distance between the z -axis of the coil and the one of the hole is r_0 . The region of interest is truncated at $z = 0$ and $z = h$, where conditions of zero tangential electric field (perfect electric conductor -PEC condition) and zero tangential magnetic flux density (perfect magnetic conductor - PMC condition) are considered, respectively.

Figure 3.2: ρ - z cross section of a semi-infinite tube.

One can select either PMC or PEC conditions at the truncation boundaries without affecting the solution. However, as it will be clarified from the following mathematical analysis, our selection leads to simpler expressions of the field since some terms vanish. The entire domain is also separated in three subregions, where the field is expressed differently. In all air regions, where only TE terms appear, a scalar potential formulation is followed. The TE scalar potentials include the contributions from the source (coil) ϕ^s and from a perturbation term from induced currents in the conductor ϕ^{per} . Moreover, in the conducting part of region II the field is due to the induced currents. TE, TM and TEM terms can appear and thus, the field is expressed with the formulation of a second order vector potential decomposed in a TE (W_a) and a TM (W_b) scalar potential. All potentials, ϕ , W_a and W_b satisfy the general Helmholtz equation (2.39) which is solved with the method of separation of variables. Therefore, the potentials are expressed as in (2.40). In [FN93] one can find a summary table (Table 3.1) of all possible solutions of the scalar Helmholtz equation in cylindrical coordinates using the modified Bessel functions I and K

		$R_m(p, \rho)$	$\Phi_m(\varphi)$	$Z(z)$
TE	$m \neq 0, q \neq 0$	$I_m(p\rho), K_m(p\rho)$	$e^{jm\varphi}, e^{-jm\varphi}$	e^{jqz}, e^{-jqz}
and	$m \neq 0, q = 0, k \neq 0$	$I_m(k\rho), K_m(k\rho)$	$e^{jm\varphi}, e^{-jm\varphi}$	const, z
TM	$m \neq 0, q = 0, k = 0$	ρ^m, ρ^{-m}	$e^{jm\varphi}, e^{-jm\varphi}$	const, z
	$m = 0, q = 0, k = 0$	$\ln(\rho)$	1	const, z
TEM	$p = 0, m \neq 0$	ρ^m, ρ^{-m}	$e^{jm\varphi}, e^{-jm\varphi}$	$\cosh(kz), \sinh(kz)$
	$p = 0, m = 0$	$\ln(\rho)$	1	$\cosh(kz), \sinh(kz)$

Table 3.1: Solution functions of the scalar Helmholtz equation in cylindrical coordinates.

Hence, with regard to Table 3.1 the potentials in each region are written:

Region I

$$\begin{aligned}\phi^s = & \sum_{m=-\infty}^{m=\infty} \sum_{n=1}^{\infty} [S_{mn}^s \sin(w_n z) + A_{mn}^s \cos(w_n z)] K_m(w_n \rho) e^{jm\varphi} \\ & + \sum_{m=-\infty}^{m=\infty} (B_m^s z + C_m^s) \rho^{-m} e^{jm\varphi}\end{aligned}\quad (3.1)$$

$$\begin{aligned}\phi^I = & \sum_{m=-\infty}^{m=\infty} \sum_{n=1}^{\infty} [F_{mn} \sin(w_n z) + A_{mn} \cos(w_n z)] I_m(w_n \rho) e^{jm\varphi} \\ & + \sum_{m=-\infty}^{m=\infty} (D_m^{(0)} z + E_m^{(0)}) \rho^m e^{jm\varphi}\end{aligned}\quad (3.2)$$

Region II In region *II* the total field is the superposition of a field vanishing for $\rho \rightarrow \infty$ (denoted by the superscript $\rho^>$) and of a field vanishing for $\rho \rightarrow 0$ (denoted by the superscript $\rho^<$). The former represents the source field and the perturbation due to the interface $\rho = b_1$ and it is expressed by K_m Bessel functions and the ρ^{-m} function, whereas the latter represents the perturbation due to the interface $\rho = b_2$ and is expressed by I_m Bessel functions and the ρ^m function. For the sake of simplicity this superposition will be represented hereinafter by $\left\{ \right\}$ and the notations $\rho^>$ and $\rho^<$ will be merged in ρ^{\leq} .

$$\begin{aligned}\phi^{II} = & \sum_{m=-\infty}^{m=\infty} \sum_{n=1}^{\infty} \left[B_{mn}^{\rho^{\leq}} \sin(p_n(h-z)) + L_{mn}^{\rho^{\leq}} \cos(p_n(h-z)) \right] \left\{ \begin{array}{l} K_m(p_n \rho) \\ I_m(p_n \rho) \end{array} \right\} e^{jm\varphi} \\ & + \sum_{m=-\infty}^{m=\infty} \left[F_m^{\rho^{\leq}(0)} z + L_m^{\rho^{\leq}(0)} \right] \left\{ \begin{array}{l} \rho^{-m} \\ \rho^m \end{array} \right\} e^{jm\varphi} \quad ; \quad c \leq z \leq h\end{aligned}\quad (3.3)$$

$$\begin{aligned}W_a^{II} = & \sum_{m=-\infty}^{m=\infty} \sum_{n=1}^{\infty} \left[C_{mn}^{\rho^{\leq}} \sin(q_n z) + M_{mn}^{\rho^{\leq}} \cos(q_n z) \right] \left\{ \begin{array}{l} K_m(p_n \rho) \\ I_m(p_n \rho) \end{array} \right\} e^{jm\varphi} \\ & + \sum_{m=-\infty}^{m=\infty} \left[M_m^{\rho^{\leq}(0)} z + N_m^{\rho^{\leq}(0)} \right] \left\{ \begin{array}{l} K_m(k \rho) \\ I_m(k \rho) \end{array} \right\} e^{jm\varphi} \quad ; \quad 0 \leq z \leq c\end{aligned}\quad (3.4)$$

$$\begin{aligned}W_b^{II} = & \sum_{m=-\infty}^{m=\infty} \sum_{n=1}^{\infty} \left[N_{mn}^{\rho^{\leq}} \sin(\nu_n z) + D_{mn}^{\rho^{\leq}} \cos(\nu_n z) \right] \left\{ \begin{array}{l} K_m(\xi_n \rho) \\ I_m(\xi_n \rho) \end{array} \right\} e^{jm\varphi} \\ & + \sum_{m=-\infty}^{m=\infty} \left[O_m^{\rho^{\leq}(0)} z + P_m^{\rho^{\leq}(0)} \right] \left\{ \begin{array}{l} K_m(k \rho) \\ I_m(k \rho) \end{array} \right\} e^{jm\varphi} \\ & + \sum_{m=-\infty}^{m=\infty} \left[Q_m^{\rho^{\leq}(0)} \sinh(kz) + R_m^{\rho^{\leq}(0)} \cosh(kz) \right] \left\{ \begin{array}{l} \rho^{-m} \\ \rho^m \end{array} \right\} e^{jm\varphi} \quad ; \quad 0 \leq z \leq c,\end{aligned}\quad (3.5)$$

where $p_n^2 = q_n^2 + k^2$ and $\xi_n^2 = \nu_n^2 + k^2$.

Region III

$$\begin{aligned}\phi^{III} = & \sum_{m=-\infty}^{m=\infty} \sum_{n=1}^{\infty} [O_{mn} \sin(w_n z) + E_{mn} \cos(w_n z)] K_m(w_n \rho) e^{jm\varphi} \\ & + \sum_{m=-\infty}^{m=\infty} [S_m^{(0)} z + T_m^{(0)}] \rho^{-m} e^{jm\varphi}.\end{aligned}\quad (3.6)$$

In order to calculate the field in all regions, one must calculate the unknown coefficients of the z -depending functions $Z(z)$ for each potential (i.e. $A_{mn}^s, S_{mn}^s, B_m^s$ and C_m^s in (3.1)) as well as the eigenvalues w_n, p_n and ξ_n . This is achieved by applying the PMC and PEC conditions at the truncation interfaces and the field continuity conditions at the conductor-air interfaces $\rho = b_1, \rho = b_2$ and $z = c$. For the sake of brevity, all conditions applied in the analysis of this section are presented after having multiplied all terms by $e^{-jm\varphi}$ and integrating over φ from 0 to 2π ($\int_0^{2\pi} \dots e^{-jm\varphi} d\varphi$), in order to make use of the orthogonality of the $e^{-jm\varphi}$ functions. Moreover, the superscripts I, II or III on a quantity denote the region to which it refers.

The first conditions applied are the PEC and PMC conditions at the truncation interfaces. At $z = 0$ the PEC condition is considered in every region, in other words, the tangential electric field is considered zero. Consequently, the normal magnetic flux density is also zero. In **region I** the PEC condition gives

$$B_z^I|_{z=0} = 0 \Leftrightarrow \sum_{n=1}^{\infty} [S_{mn}^s w_n K_m(w_n \rho) + F_{mn} w_n I_m(w_n \rho)] + B_m^s \rho^{-m} + D_m^{(0)} \rho^m = 0. \quad (3.7)$$

Since (3.7) holds for every ρ

$$\boxed{S_{mn}^s = F_{mn} = B_m^s = D_m^{(0)} = 0}. \quad (3.8)$$

Similarly in **region II**

$$\begin{aligned}B_z^{II}|_{z=0} = 0 \Leftrightarrow & - \sum_{n=1}^{\infty} M_{mn}^{\rho \leqslant} p_n^2 \begin{Bmatrix} K_m(p_n \rho) \\ I_m(p_n \rho) \end{Bmatrix} + N_m^{\rho \leqslant(0)} k^2 \begin{Bmatrix} K_m(k \rho) \\ I_m(k \rho) \end{Bmatrix} = 0 \Leftrightarrow \\ & \boxed{M_{mn}^{\rho \leqslant} = N_m^{\rho \leqslant(0)} = 0} \quad (3.9)\end{aligned}$$

$$\begin{aligned}E_{\phi}^{II}|_{z=0} = 0 \stackrel{(3.9)}{\Leftrightarrow} & - \frac{\omega m}{\rho} \sum_{n=1}^{\infty} N_{mn}^{\rho \leqslant} \begin{Bmatrix} K_m(p_n \rho) \\ I_m(p_n \rho) \end{Bmatrix} + O_m^{\rho \leqslant(0)} \begin{Bmatrix} K_m(k \rho) \\ I_m(k \rho) \end{Bmatrix} + Q_m^{\rho \leqslant(0)} k \begin{Bmatrix} \rho^{-m} \\ \rho^m \end{Bmatrix} = 0 \Leftrightarrow \\ & \boxed{N_{mn}^{\rho \leqslant} = O_m^{\rho \leqslant(0)} = Q_m^{\rho \leqslant(0)} = 0}. \quad (3.10)\end{aligned}$$

Also in **region III**

$$B_z^{III}|_{z=0} = 0 \Leftrightarrow \sum_{n=1}^{\infty} O_{mn} w_n K_m(w_n \rho) + S_m^{(0)} \rho^{-m} = 0 \Leftrightarrow \\ O_{mn} = S_m^{(0)} = 0. \quad (3.11)$$

Additionally, at $z = h$ the PMC condition is considered, which implies zero tangential magnetic flux density. Hence, taking into account (3.8) and (3.11) we obtain for the different regions

Region I

$$B_\rho^I|_{z=h} = 0 \Leftrightarrow \\ \sum_{n=1}^{\infty} w_n \cos(w_n h) [A_{mn}^s K'_m(w_n \rho) + A_{mn} I'_m(w_n \rho)] - m [C_m^s \rho^{-m-1} + E_m^{(0)} \rho^{m-1}] = 0 \Leftrightarrow \\ \cos(w_n h) = 0 \Leftrightarrow w_n = \frac{(2n-1)\pi}{2h} \quad \text{and} \quad C_m^s = E_m^{(0)} = 0. \quad (3.12)$$

Region II

$$B_\rho^{II}|_{z=0} = 0 \Leftrightarrow \sum_{n=1}^{\infty} L_{mn}^{\rho \leqslant} p_n \left\{ \begin{array}{l} K'_m(p_n \rho) \\ I'_m(p_n \rho) \end{array} \right\} + (F_m^{\rho \leqslant(0)} h + L_m^{\rho \leqslant(0)}) \left\{ \begin{array}{l} m \rho^{-m-1} \\ -m \rho^{m-1} \end{array} \right\} = 0 \Leftrightarrow \\ L_{mn}^{\rho \leqslant} = 0 \quad \text{and} \quad F_m^{\rho \leqslant(0)} h + L_m^{\rho \leqslant(0)} = 0 \quad (3.13)$$

Region III

$$B_\rho^{III}|_{z=h} = 0 \Leftrightarrow \sum_{n=1}^{\infty} w_n \cos(w_n h) E_{mn} K'_m(w_n \rho) - T_m^{(0)} m \rho^{-m-1} = 0$$

and taking (6.8) into account it becomes

$$T_m^{(0)} = 0. \quad (3.14)$$

The second applied set of conditions is the boundary conditions at the horizontal interface $z = c$. As this is an air-conductor interface the normal current density is zero.

$$J_z|_{z=c} = -j\omega\sigma[\nabla \times W]_z = -j\omega\sigma(k^2 W_b - \frac{\partial^2 W_b}{\partial z^2}) = 0 \Leftrightarrow \\ -j\omega\sigma \left(\sum_{n=1}^{\infty} D_{mn}^{\rho \leqslant} \xi_i^2 \cos(\nu_n c) \left\{ \begin{array}{l} K_m(\xi_n \rho) \\ I_m(\xi_n \rho) \end{array} \right\} + k^2 P_m^{\rho \leqslant(0)} \left\{ \begin{array}{l} K_m(k \rho) \\ I_m(k \rho) \end{array} \right\} \right) = 0,$$

which holds for every ρ , and thus we obtain for the eigenvalues

$$\cos(\nu_n c) = 0 \Leftrightarrow \left[\nu_n = \frac{(2n-1)\pi}{2c} \right] \quad \text{and} \quad \left[P_m^{\rho \leq 0} = 0 \right]. \quad (3.15)$$

In addition, combination of the H_ρ and B_z continuity accross the air-conductor interface leads to a transcendental equation, the solution of which provides the p_n eigenvalues.

$$\begin{aligned} H_\rho^{II}|_{z=c^-} &= H_\rho^{II}|_{z=c^+} \Leftrightarrow \\ \sum_{n=1}^{\infty} C_{mn}^{\rho \leq 0} p_n q_n \cos(q_n c) &\left\{ \begin{array}{l} K'_m(p_n \rho) \\ I'_m(p_n \rho) \end{array} \right\} + M_m^{\rho \leq 0} k \left\{ \begin{array}{l} K'_m(k \rho) \\ I'_m(k \rho) \end{array} \right\} + \frac{k^2 j m}{\rho} R_m^{\rho \leq 0} \cosh(k c) \left\{ \begin{array}{l} \rho^{-m} \\ \rho^m \end{array} \right\} \\ &= \sum_{n=1}^{\infty} B_{mn}^{\rho \leq 0} p_n \sin(p_n(h-c)) \left\{ \begin{array}{l} K'_m(p_n \rho) \\ I'_m(p_n \rho) \end{array} \right\} + (F_m^{\rho \leq 0} c + L_m^{\rho \leq 0}) \left\{ \begin{array}{l} m \rho^{-m-1} \\ -m \rho^{m-1} \end{array} \right\} \Leftrightarrow \\ B_{mn}^{\rho \leq 0} &= \frac{q_n \cos(q_n c)}{\sin(p_n(h-c))} C_{mn}^{\rho \leq 0} \quad \text{and} \quad \left[M_m^{\rho \leq 0} = F_m^{\rho \leq 0} c + L_m^{\rho \leq 0} = 0 \right], \end{aligned} \quad (3.16)$$

where $\alpha_n = \frac{q_n \cos(q_n c)}{\sin(p_n(h-c))}$. From (3.13) and (3.16) we conclude that

$$\left[F_m^{\rho \leq 0} = L_m^{\rho \leq 0} = 0 \right]. \quad (3.17)$$

$$\begin{aligned} B_z^{II}|_{z=c^-} &= B_z^{II}|_{z=c^+} \Leftrightarrow \\ - \sum_{n=1}^{\infty} C_{mn}^{\rho \leq 0} p_n^2 \sin(q_n c) &\left\{ \begin{array}{l} K_m(p_n \rho) \\ I_m(p_n \rho) \end{array} \right\} = - \sum_{n=1}^{\infty} B_{mn}^{\rho \leq 0} p_n \cos(p_n(h-c)) \left\{ \begin{array}{l} K_m(p_n \rho) \\ I_m(p_n \rho) \end{array} \right\} \Leftrightarrow \\ B_{mn}^{\rho \leq 0} &= \frac{p_n \sin(q_n c)}{\cos(p_n(h-c))} C_{mn}^{\rho \leq 0}. \end{aligned} \quad (3.18)$$

By combining (3.16) and (3.18) we obtain the transcendental equation

$$\frac{q_n \cos(q_n c)}{\sin(p_n(h-c))} = \frac{p_n \sin(q_n c)}{\cos(p_n(h-c))} \Leftrightarrow \left[q_n \cot(q_n c) = p_n \tan(p_n(h-c)) \right]. \quad (3.19)$$

We recapitulate here for convenience of the reader the expressions for the potentials as they result after taking (3.8) - (3.17) into consideration.

$$\phi^s = \sum_{m=-\infty}^{m=\infty} \sum_{n=1}^{\infty} A_{mn}^s \cos(w_n z) K_m(w_n \rho) e^{j m \varphi} \quad (3.20)$$

$$\phi^I = \sum_{m=-\infty}^{m=\infty} \sum_{n=1}^{\infty} A_{mn}^I \cos(w_n z) I_m(w_n \rho) e^{j m \varphi} \quad (3.21)$$

$$\phi^{II} = \sum_{m=-\infty}^{m=\infty} \sum_{n=1}^{\infty} B_{mn}^{\rho \lessgtr} \sin(p_n(h-z)) \begin{Bmatrix} K_m(p_n\rho) \\ I_m(p_n\rho) \end{Bmatrix} e^{jm\varphi} ; \quad c \leq z \leq h \quad (3.22)$$

$$W_a^{II} = \sum_{m=-\infty}^{m=\infty} \sum_{n=1}^{\infty} C_{mn}^{\rho \lessgtr} \sin(q_n z) \begin{Bmatrix} K_m(p_n\rho) \\ I_m(p_n\rho) \end{Bmatrix} e^{jm\varphi} ; \quad 0 \leq z \leq c \quad (3.23)$$

$$W_b^{II} = \sum_{m=-\infty}^{m=\infty} \sum_{n=1}^{\infty} D_{mn}^{\rho \lessgtr} \cos(\nu_n z) \begin{Bmatrix} K_m(\xi_n\rho) \\ I_m(\xi_n\rho) \end{Bmatrix} e^{jm\varphi} ; \quad 0 \leq z \leq c \quad (3.24)$$

$$\phi^{III} = \sum_{m=-\infty}^{m=\infty} \sum_{n=1}^{\infty} E_{mn} \cos(w_n z) K_m(w_n \rho) e^{jm\varphi}. \quad (3.25)$$

Finally, matching the field at the radial interfaces results into a system of equations, the solution of which yields the expansion coefficients. Therefore, at $\rho = b_1$

$$\begin{aligned} H_\rho^I|_{\rho=b_1} = H_\rho^{II}|_{\rho=b_1} \Leftrightarrow & \sum_{n=1}^{\infty} w_n \cos(w_n z) [A_{mn}^s K'_m(w_n b_1) + A_{mn} I'_m(w_n b_1)] = \\ & u(z-c) \sum_{n=1}^{\infty} B_{mn}^{\rho \lessgtr} p_n \sin(p_n(h-z)) \begin{Bmatrix} K'_m(p_n b_1) \\ I'_m(p_n b_1) \end{Bmatrix} \\ & + [u(z)-u(z-c)] \sum_{n=1}^{\infty} C_{mn}^{\rho \lessgtr} p_n q_n \cos(q_n z) \begin{Bmatrix} K'_m(p_n b_1) \\ I'_m(p_n b_1) \end{Bmatrix} \\ & + [u(z)-u(z-c)] \sum_{n=1}^{\infty} D_{mn}^{\rho \lessgtr} \frac{k^2 jm}{b} \cos(\nu_n z) \begin{Bmatrix} K_m(\xi_n b_1) \\ I_m(\xi_n b_1) \end{Bmatrix} \end{aligned} \quad (3.26)$$

$$\begin{aligned} H_\phi^I|_{\rho=b_1} = H_\phi^{II}|_{\rho=b_1} \Leftrightarrow & \sum_{n=1}^{\infty} \frac{jm}{b_1} \cos(w_n z) [A_{mn}^s K_m(w_n b_1) + A_{mn} I_m(w_n b_1)] = \\ & u(z-c) \sum_{n=1}^{\infty} B_{mn}^{\rho \lessgtr} \frac{jm}{b_1} \sin(p_n(h-z)) \begin{Bmatrix} K_m(p_n b_1) \\ I_m(p_n b_1) \end{Bmatrix} \\ & + [u(z)-u(z-c)] \sum_{n=1}^{\infty} C_{mn}^{\rho \lessgtr} \frac{jm}{b_1} q_n \cos(q_n z) \begin{Bmatrix} K_m(p_n b_1) \\ I_m(p_n b_1) \end{Bmatrix} \\ & - [u(z)-u(z-c)] \sum_{n=1}^{\infty} D_{mn}^{\rho \lessgtr} k \xi_n \cos(\nu_n z) \begin{Bmatrix} K'_m(\xi_n b_1) \\ I'_m(\xi_n b_1) \end{Bmatrix} \end{aligned} \quad (3.27)$$

and

$$\begin{aligned} B_z^I|_{\rho=b_1} = B_z^{II}|_{\rho=b_1} \Leftrightarrow & - \sum_{n=1}^{\infty} w_n \sin(w_n z) [A_{mn}^s K_m(w_n b_1) + A_{mn} I_m(w_n b_1)] = \\ & - u(z-c) \sum_{n=1}^{\infty} B_{mn}^{\rho \lessgtr} p_n \cos(p_n(h-z)) \begin{Bmatrix} K_m(p_n b_1) \\ I_m(p_n b_1) \end{Bmatrix} \\ & + [u(z)-u(z-c)] \sum_{n=1}^{\infty} C_{mn}^{\rho \lessgtr} p_n^2 \sin(q_n z) \begin{Bmatrix} K_m(p_n b_1) \\ I_m(p_n b_1) \end{Bmatrix}. \end{aligned} \quad (3.28)$$

The continuity equations (3.26), (3.27) are weighted with $\cos(w_l z)$ and (3.28) with $\sin(w_l z)$, and taking into account the orthogonality of the trigonometric functions

$$\int_0^h \sin(u_l z) \sin(u_n z) dz = \int_0^h \cos(u_l z) \cos(u_n z) dz = \delta_{l,n} \frac{h}{2}, \quad (3.29)$$

where δ is the Dirac delta function, as well as (3.16), it is obtained

$$\begin{aligned} w_n I'_m(w_n b_1) A_{mn} &= M_c(l, n) p_n \left\{ \begin{array}{c} K'_m(p_n b_1) \\ I'_m(p_n b_1) \end{array} \right\} C_{mn}^{\rho \lessgtr} + \frac{k^2 j m}{b} M_r(l, n) \left\{ \begin{array}{c} K_m(\xi_n b_1) \\ I_m(\xi_n b_1) \end{array} \right\} D_{mn}^{\rho \lessgtr} \\ &\quad - w_n K'_m(w_n b_1) A_{mn}^s \end{aligned} \quad (3.30)$$

$$\begin{aligned} \frac{j m}{b_1} I_m(w_n b_1) A_{mn} &= M_c(l, n) \frac{j m}{b_1} \left\{ \begin{array}{c} K_m(p_n b_1) \\ I_m(p_n b_1) \end{array} \right\} C_{mn}^{\rho \lessgtr} - k^2 \xi_n M_r(l, n) \left\{ \begin{array}{c} K'_m(\xi_n b_1) \\ I'_m(\xi_n b_1) \end{array} \right\} D_{mn}^{\rho \lessgtr} \\ &\quad - \frac{j m}{b_1} K_m(w_n b_1) A_{mn}^s \end{aligned} \quad (3.31)$$

and

$$w_n I_m(w_n b_1) A_{mn} = M_s(l, n) p_n \left\{ \begin{array}{c} K_m(p_n b_1) \\ I_m(p_n b_1) \end{array} \right\} C_{mn}^{\rho \lessgtr} - w_n K_m(w_n b_1) A_{mn}^s, \quad (3.32)$$

where

$$M_c(l, n) = \frac{2}{h} [q_n \int_0^c \cos(q_n z) \cos(w_l z) dz + \alpha_n \int_c^h \sin(p_n(h-z)) \cos(w_l z) dz] \quad (3.33)$$

$$M_s(l, n) = \frac{2}{h} [p_n \int_0^c \sin(q_n z) \sin(w_l z) dz - \alpha_n \int_c^h \cos(p_n(h-z)) \sin(w_l z) dz] \quad (3.34)$$

$$M_r(l, n) = \frac{2}{h} \int_0^c \cos(\nu_n z) \cos(w_l z) dz. \quad (3.35)$$

In the same fashion, the application of the continuity conditions at $\rho = b_2$ yields

$$\begin{aligned} H_\rho^{II} \Big|_{\rho=b_2} &= H_\rho^{III} \Big|_{\rho=b_2} \Leftrightarrow \\ \sum_{n=1}^{\infty} E_{mn} w_n \cos(w_n z) K'_m(w_n b_2) &= u(z-c) \sum_{n=1}^{\infty} B_{mn}^{\rho \lessgtr} p_n \sin(p_n(h-z)) \left\{ \begin{array}{c} K'_m(p_n b_2) \\ I'_m(p_n b_2) \end{array} \right\} \\ &\quad + [u(z) - u(z-c)] \sum_{n=1}^{\infty} C_{mn}^{\rho \lessgtr} p_n q_n \cos(q_n z) \left\{ \begin{array}{c} K'_m(p_n b_2) \\ I'_m(p_n b_2) \end{array} \right\} \\ &\quad + [u(z) - u(z-c)] \sum_{n=1}^{\infty} D_{mn}^{\rho \lessgtr} \frac{k^2 j m}{b} \cos(\nu_n z) \left\{ \begin{array}{c} K_m(\xi_n b_2) \\ I_m(\xi_n b_2) \end{array} \right\} \end{aligned} \quad (3.36)$$

$$\begin{aligned}
H_{\phi}^{II}\Big|_{\rho=b_2} = H_{\phi}^{III}\Big|_{\rho=b_2} \Leftrightarrow \\
\sum_{n=1}^{\infty} \frac{jm}{b_2} \cos(w_n z) E_{mn} K_m(w_n b_2) = u(z-c) \sum_{n=1}^{\infty} B_{mn}^{\rho \leq} \frac{jm}{b_2} \sin(p_n(h-z)) \left\{ \begin{array}{l} K_m(p_n b_2) \\ I_m(p_n b_2) \end{array} \right\} \\
+ [u(z) - u(z-c)] \sum_{n=1}^{\infty} C_{mn}^{\rho \leq} \frac{jm}{b_2} q_n \cos(q_n z) \left\{ \begin{array}{l} K_m(p_n b_2) \\ I_m(p_n b_2) \end{array} \right\} \\
- [u(z) - u(z-c)] \sum_{n=1}^{\infty} D_{mn}^{\rho \leq} k \xi_n \cos(\nu_n z) \left\{ \begin{array}{l} K'_m(\xi_n b_2) \\ I'_m(\xi_n b_2) \end{array} \right\}
\end{aligned} \tag{3.37}$$

and

$$\begin{aligned}
B_z^{II}\Big|_{\rho=b_2} = B_z^{III}\Big|_{\rho=b_2} \Leftrightarrow \\
-\sum_{n=1}^{\infty} w_n \sin(w_n z) E_{mn} K_m(w_n b_2) = -u(z-c) \sum_{n=1}^{\infty} B_{mn}^{\rho \leq} p_n \cos(p_n(h-z)) \left\{ \begin{array}{l} K_m(p_n b_2) \\ I_m(p_n b_2) \end{array} \right\} \\
+ [u(z) - u(z-c)] \sum_{n=1}^{\infty} C_{mn}^{\rho \leq} p_n^2 \sin(q_n z) \left\{ \begin{array}{l} K_m(p_n b_2) \\ I_m(p_n b_2) \end{array} \right\}.
\end{aligned} \tag{3.38}$$

Weighting again (3.36) and (3.37) with $\cos(w_l z)$, (3.38) with $\sin(w_l z)$, and considering (3.16) we obtain the following expressions

$$w_n I'_m(w_n b_1) E_{mn} = M_c(l, n) p_n \left\{ \begin{array}{l} K'_m(p_n b_1) \\ I'_m(p_n b_1) \end{array} \right\} C_{mn}^{\rho \leq} + \frac{k^2 jm}{b} M_r(l, n) \left\{ \begin{array}{l} K_m(\xi_n b_1) \\ I_m(\xi_n b_1) \end{array} \right\} D_{mn}^{\rho \leq} \tag{3.39}$$

$$\frac{jm}{b_1} I_m(w_n b_1) E_{mn} = M_c(l, n) \frac{jm}{b_1} \left\{ \begin{array}{l} K_m(p_n b_1) \\ I_m(p_n b_1) \end{array} \right\} C_{mn}^{\rho \leq} - k^2 \xi_n M_r(l, n) \left\{ \begin{array}{l} K'_m(\xi_n b_1) \\ I'_m(\xi_n b_1) \end{array} \right\} D_{mn}^{\rho \leq} \tag{3.40}$$

$$w_n I_m(w_n b_1) E_{mn} = M_s(l, n) p_n \left\{ \begin{array}{l} K_m(p_n b_1) \\ I_m(p_n b_1) \end{array} \right\} C_{mn}^{\rho \leq}. \tag{3.41}$$

3.2.2 Excitation terms

The expansion coefficients A_{mn}^s depend only on the probe geometry and position. In this work we are interested in cylindrical coils. Fig. 3.3 shows two possible orientations of a cylindrical coil in a hole of radius b ; when the axis of the coil is parallel to the tube axis (Fig. 3.3a), the so called "offset coil", and when it is perpendicular (Fig. 3.3b) to the hole surface, known as "rotary coil".

In the case of an offset coil the expansion coefficients are given in [TB08]

$$A_{mn}^s = \frac{2\mu_0 NI}{h H_c} \frac{\cos(w_n z_1) - \cos(w_n z_2)}{w_n^3} \times \Phi(w_n r_b, w_n r_a) K_m(w_n b_1) I_m(w_n r_0), \tag{3.42}$$

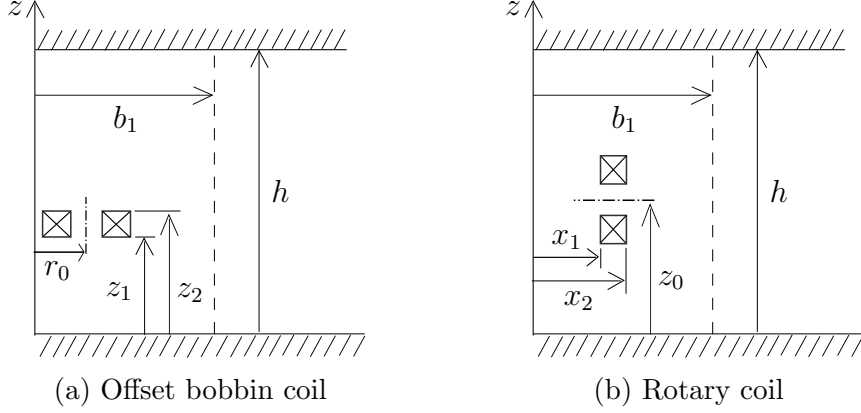


Figure 3.3: Coil positions

where

$$\Phi(\alpha_2, \alpha_1) = \int_{\alpha_1}^{\alpha_2} I_1(x) x dx. \quad (3.43)$$

As far as the rotary coil is concerned, the expansion coefficients read [TB08]

$$A_{mn}^s = -\frac{4\mu_0 NI}{\pi h H_c} \cos(w_n z' \frac{m}{w_n^3}) \sin(m \frac{\pi}{2}) K_m(w_n b_1) \times \sum_{i=-\infty}^{\infty} \Psi_{m-i}(w_n x_2, w_n x_1) \Xi_i(w_n r_b, w_n r_a), \quad (3.44)$$

where

$$\Psi(\alpha_2, \alpha_1) = \int_{\alpha_1}^{\alpha_2} I_m(x) dx \quad (3.45)$$

and

$$\Xi_i(v_2, v_1) = \int_{v_1}^{v_2} \int_0^v \frac{1}{\xi} I_i(\xi) \sin(\sqrt{v^2 - \xi^2}) d\xi dv, \quad v = w_n r_0 \quad (3.46)$$

3.2.3 Numerical treatment

The domain truncation allows to express the field in terms of series expansion. For the numerical evaluation of the infinite series, however, the number of terms taken into account must be limited to a finite number, which has to be chosen in order to assure sufficient precision. In this way, the system (6.10)-(6.12) and (6.13)-(6.15) is converted into a finite system of linear equations. The numerical solution of the problem requires the expression of the system in matrix notation, which reads

$$\mathbf{w} \mathbf{I}'_{\mathbf{w},1} \mathbf{A} = \mathbf{M}_c \mathbf{p} \begin{Bmatrix} \mathbf{K}'_{\mathbf{p},1} \\ \mathbf{I}'_{\mathbf{p},1} \end{Bmatrix} \mathbf{C}^{\rho \leqslant} + \frac{k^2 jm}{b_1} \mathbf{M}_r \begin{Bmatrix} \mathbf{K}_{\boldsymbol{\xi},1} \\ \mathbf{I}_{\boldsymbol{\xi},1} \end{Bmatrix} \mathbf{D}^{\rho \leqslant} - \mathbf{w} \mathbf{K}'_{\mathbf{w},1} \mathbf{A}^s \quad (3.47)$$

$$\frac{jm}{b_1} \mathbf{I}_{\mathbf{w},1} \mathbf{A} = \frac{jm}{b_1} \mathbf{M}_c \begin{Bmatrix} \mathbf{K}_{\mathbf{p},1} \\ \mathbf{I}_{\mathbf{p},1} \end{Bmatrix} \mathbf{C}^{\rho \leqslant} - k^2 \boldsymbol{\xi} \mathbf{M}_r \begin{Bmatrix} \mathbf{K}'_{\boldsymbol{\xi},1} \\ \mathbf{I}'_{\boldsymbol{\xi},1} \end{Bmatrix} \mathbf{D}^{\rho \leqslant} - \frac{jm}{b_1} \mathbf{K}_{\mathbf{w},1} \mathbf{A}^s \quad (3.48)$$

$$\mathbf{w}\mathbf{I}_{\mathbf{w},1}\mathbf{A} = \mathbf{M}_s \mathbf{p} \begin{Bmatrix} \mathbf{K}_{\mathbf{p},1} \\ \mathbf{I}_{\mathbf{p},1} \end{Bmatrix} \mathbf{C}^{\rho \lessgtr} - \mathbf{w}\mathbf{K}_{\mathbf{w},1}\mathbf{A}^s \quad (3.49)$$

$$\mathbf{w}\mathbf{K}'_{\mathbf{w},2}\mathbf{E} = \mathbf{M}_c \mathbf{p} \begin{Bmatrix} \mathbf{K}'_{\mathbf{p},2} \\ \mathbf{I}'_{\mathbf{p},2} \end{Bmatrix} \mathbf{C}^{\rho \lessgtr} + \frac{k^2 jm}{b_2} \mathbf{M}_r \begin{Bmatrix} \mathbf{K}_{\xi,2} \\ \mathbf{I}_{\xi,2} \end{Bmatrix} \mathbf{D}^{\rho \lessgtr} \quad (3.50)$$

$$\frac{jm}{b_2} \mathbf{K}_{\mathbf{w},2}\mathbf{E} = \frac{jm}{b_2} \mathbf{M}_c \begin{Bmatrix} \mathbf{K}_{\mathbf{p},2} \\ \mathbf{I}_{\mathbf{p},2} \end{Bmatrix} \mathbf{C}^{\rho \lessgtr} - k^2 \boldsymbol{\xi} \mathbf{M}_r \begin{Bmatrix} \mathbf{K}'_{\xi,2} \\ \mathbf{I}'_{\xi,2} \end{Bmatrix} \mathbf{D}^{\rho \lessgtr} \quad (3.51)$$

$$\mathbf{w}\mathbf{K}_{\mathbf{w},2}\mathbf{E} = \mathbf{M}_s \mathbf{p} \begin{Bmatrix} \mathbf{K}_{\mathbf{p},2} \\ \mathbf{I}_{\mathbf{p},2} \end{Bmatrix} \mathbf{C}^{\rho \lessgtr}. \quad (3.52)$$

Here, \mathbf{A} , \mathbf{A}^s , $\mathbf{C}^{\rho <}$, $\mathbf{C}^{\rho >}$, $\mathbf{D}^{\rho <}$, $\mathbf{D}^{\rho >}$ and \mathbf{E} are column vectors of the expansion coefficients, \mathbf{w} , \mathbf{p} and $\boldsymbol{\xi}$ are diagonal matrices of the eigenvalues, \mathbf{M}_c , \mathbf{M}_s and \mathbf{M}_r are the matrices (6.16)-(6.18) and

$$\mathbf{I}_{\mathbf{x},i} = \text{diag}[I_m(x_n b_i)] \quad (3.53)$$

$$\mathbf{K}_{\mathbf{x},i} = \text{diag}[K_m(x_n b_i)]. \quad (3.54)$$

The number of radial and axial modes taken into account depends on coil dimensions and frequency of operation. However, in all cases the ratio of ξ and p eigenvalues numbers needs to be approximately $N_\xi/N_p \approx (c_2 - c_1)/h$, in order to keep the system condition number low [ST12] and avoid a close-to-singular system.

The transcendental equation (6.9) is solved numerically using the iterative method proposed in [Lyn67, DL67]

3.2.4 Impedance change

The NDT signal in the inspection of a work-piece is defined as the impedance change of the probe in the presence of the piece. Hence, the impedance variation calculation is the ultimate goal of eddy-current NDT problems using electric field sensors. In Section 2.5 relation (2.55) is used to calculate the impedance change in the presence of a conductor based on the reciprocity theorem. We choose the integration surface S to be a cylinder of radius b_1 , the bases of which coincide with the truncation interfaces $z = 0$ and $z = h$. Expressing the fields in (2.55) in terms of scalar potentials the expression of ΔZ becomes [TB08, ST12]

$$\Delta Z = -\frac{j\omega}{\mu_0 I^2} \int_0^h \int_0^{2\pi} [\phi^I \frac{\partial \phi^s}{\partial \rho} - \phi^s \frac{\partial \phi^I}{\partial \rho}]_{\rho=b_1} b_1 d\varphi dz, \quad (3.55)$$

By substituting (6.1) and (6.2) in (3.55) and using the Wronskian

$$I'_m(z) K_m(z) - I_m(z) K'_m(z) = \frac{1}{z} \quad (3.56)$$

(3.55) reduces to

$$\Delta Z = -\frac{j\omega}{\mu_0 I^2} \pi h \sum_{m=-\infty}^{\infty} \sum_{i=1}^{\infty} A_{mn}^s A_{mn}. \quad (3.57)$$

It is noted that (6.19) holds for a truncated domain, where PEC and PMC conditions are set at the truncation interfaces $z = 0$ and $z = h$, respectively.

3.2.5 Perspectives

The primary field problem of a work-piece of finite axial thickness can be dealt with by superposing the solution of two sub-problems: the odd solution, where the symmetrical piece is subject to an antisymmetric excitation and the even solution, where the excitation is symmetrical [BT05, TK06, ST12]. This allows the solution of the induction problem for a tube (or a plate in case the tube thickness is set sufficiently large) with finite height. Imagine a tube of height $2c$ divided by a plane of symmetry into two equal parts of height c as the one in Fig. 6.2. Depending on the condition (PEC or PMC) imposed on this symmetry plane, we can create either the odd or the even solution. The odd parity solution represents the field due to the tube, which is excited by two identical coils carrying current flow in the opposite azimuthal directions and located symmetrically with respect to the plane of symmetry $z = 0$ (Fig. 3.4a). Similarly, the even parity solution represents the field, when the current flow in the two identical coils is of the same azimuthal direction (Fig. 3.4b). The average of the odd and the even solution yields the solution of a tube of finite length $2c$ excited by a coil located in the tube.

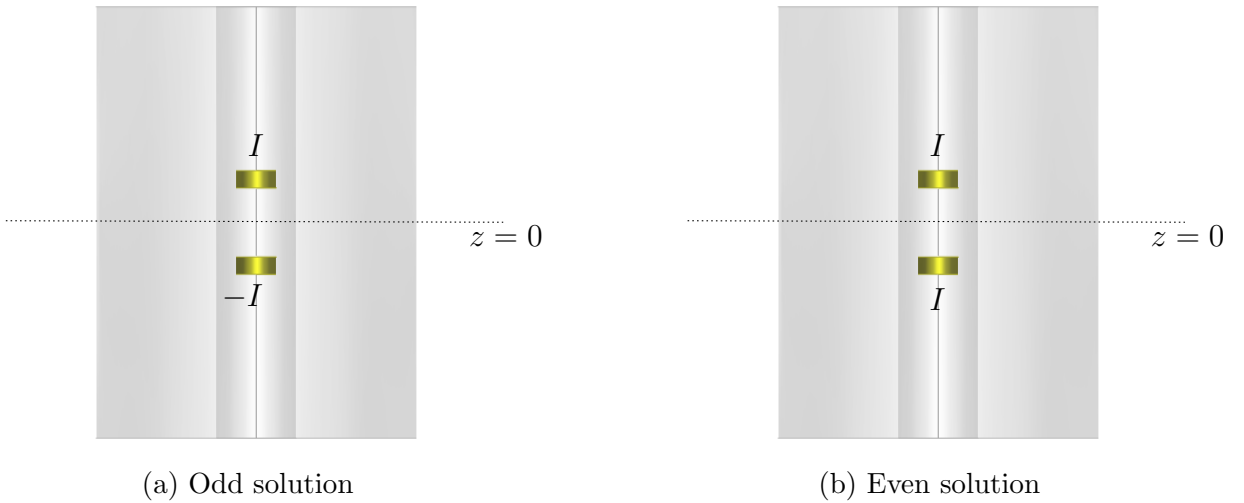


Figure 3.4: Inspection of a tube of finite length by separating the problem in two subproblems with odd and even parity. The tube height is $2c$ and the $z = 0$ plane is a symmetry plane of the tube. The coils are symmetrically located on the two sides of the symmetry plane.

The odd solution was given in the mathematical analysis of the previous subsection. In this subsection we will give an overview of the derivation of the even solution that

differs from the odd solution. Fig. 3.5 describes the problem of the even parity. The procedure followed is exactly the same as with the one of the odd parity but in this case a PMC condition is applied at the truncation boundary $z = 0$.

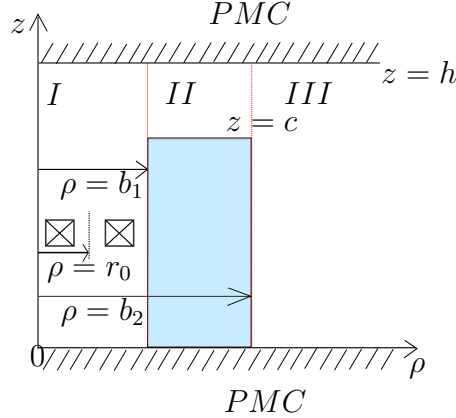


Figure 3.5: ρ - z cross section of a semi-infinite tube. Even parity.

As in the odd parity case we express the field by means of potentials 3.1-3.6. Following the same procedure as in the previous subsection, after application of the PMC conditions at the truncation boundaries and of the field continuity at $z = c$ several terms of these expressions vanish. Finally, the field potentials in each region read as

$$\phi^s = \sum_{m=-\infty}^{m=\infty} \sum_{n=1}^{\infty} A_{mn}^s \sin(w_n z) K_m(w_n \rho) e^{jm\varphi} \quad (3.58)$$

$$\phi^I = \sum_{m=-\infty}^{m=\infty} \sum_{n=1}^{\infty} A_{mn} \sin(w_n z) I_m(w_n \rho) e^{jm\varphi} \quad (3.59)$$

$$\phi^{II} = \sum_{m=-\infty}^{m=\infty} \sum_{n=1}^{\infty} B_{mn}^{\rho \lessgtr} \cos(p_n(h-z)) \begin{Bmatrix} K_m(p_n \rho) \\ I_m(p_n \rho) \end{Bmatrix} e^{jm\varphi} ; \quad c \leq z \leq h \quad (3.60)$$

$$W_a^{II} = \sum_{m=-\infty}^{m=\infty} \sum_{n=1}^{\infty} C_{mn}^{\rho \lessgtr} \cos(q_n z) \begin{Bmatrix} K_m(p_n \rho) \\ I_m(p_n \rho) \end{Bmatrix} e^{jm\varphi} ; \quad 0 \leq z \leq c \quad (3.61)$$

$$W_b^{II} = \sum_{m=-\infty}^{m=\infty} \sum_{n=1}^{\infty} D_{mn}^{\rho \lessgtr} \sin(\nu_n z) \begin{Bmatrix} K_m(\xi_n \rho) \\ I_m(\xi_n \rho) \end{Bmatrix} e^{jm\varphi} ; \quad 0 \leq z \leq c \quad (3.62)$$

$$\phi^{III} = \sum_{m=-\infty}^{m=\infty} \sum_{n=1}^{\infty} E_{mn} \sin(w_n z) K_m(w_n \rho) e^{jm\varphi} \quad (3.63)$$

and the eigenvalues w_n , ν_n and p_n are calculated from the relations

$$\sin(w_n h) = 0 \Leftrightarrow w_n = \frac{n\pi}{h} \quad (3.64)$$

$$\sin(\nu_n c) = 0 \Leftrightarrow \nu_n = \frac{n\pi}{c} \quad (3.65)$$

$$q_n \tan(q_n c) = -p_n \tan(p_n(h - c)). \quad (3.66)$$

The latter is solved again using the iterative method proposed in [Lyn67, DL67].

In addition to that, the continuity of the field at $z = c$ also provides the relation between the expansions coefficients $B_{mn}^{\rho \lessgtr}$ and $C_{mn}^{\rho \lessgtr}$.

$$B_{mn}^{\rho \lessgtr} = \frac{p_n \cos(q_n c)}{\cos(p_n(h - c))} C_{mn}^{\rho \lessgtr} \Leftrightarrow B_{mn}^{\rho \lessgtr} = \alpha_n C_{mn}^{\rho \lessgtr} \quad (3.67)$$

Additionally, by matching the field at the interfaces $\rho = b_1$ and $\rho = b_2$ we obtain the following system, the solution of which yields the expansion coefficients $A_{mn}^{\rho \lessgtr} - E_{mn}^{\rho \lessgtr}$.

$$\begin{aligned} w_n I'_m(w_n b_1) A_{mn} &= -M_s(l, n) p_n \left\{ \begin{array}{l} K'_m(p_n b_1) \\ I'_m(p_n b_1) \end{array} \right\} C_{mn}^{\rho \lessgtr} + \frac{k^2 j m}{b} M_r(l, n) \left\{ \begin{array}{l} K_m(\xi_n b_1) \\ I_m(\xi_n b_1) \end{array} \right\} D_{mn}^{\rho \lessgtr} \\ &\quad - w_n K'_m(w_n b_1) A_{mn}^s \end{aligned} \quad (3.68)$$

$$\begin{aligned} \frac{j m}{b_1} I_m(w_n b_1) A_{mn} &= -M_s(l, n) \frac{j m}{b_1} \left\{ \begin{array}{l} K_m(p_n b_1) \\ I_m(p_n b_1) \end{array} \right\} C_{mn}^{\rho \lessgtr} - k^2 \xi_n M_r(l, n) \left\{ \begin{array}{l} K'_m(\xi_n b_1) \\ I'_m(\xi_n b_1) \end{array} \right\} D_{mn}^{\rho \lessgtr} \\ &\quad - \frac{j m}{b_1} K_m(w_n b_1) A_{mn}^s \end{aligned} \quad (3.69)$$

$$w_n I_m(w_n b_1) A_{mn} = -M_c(l, n) p_n \left\{ \begin{array}{l} K_m(p_n b_1) \\ I_m(p_n b_1) \end{array} \right\} C_{mn}^{\rho \lessgtr} - w_n K_m(w_n b_1) A_{mn}^s \quad (3.70)$$

$$w_n I'_m(w_n b_1) E_{mn} = -M_s(l, n) p_n \left\{ \begin{array}{l} K'_m(p_n b_1) \\ I'_m(p_n b_1) \end{array} \right\} C_{mn}^{\rho \lessgtr} + \frac{k^2 j m}{b} M_r(l, n) \left\{ \begin{array}{l} K_m(\xi_n b_1) \\ I_m(\xi_n b_1) \end{array} \right\} D_{mn}^{\rho \lessgtr} \quad (3.71)$$

$$\frac{j m}{b_1} I_m(w_n b_1) E_{mn} = -M_s(l, n) \frac{j m}{b_1} \left\{ \begin{array}{l} K_m(p_n b_1) \\ I_m(p_n b_1) \end{array} \right\} C_{mn}^{\rho \lessgtr} - k^2 \xi_n M_r(l, n) \left\{ \begin{array}{l} K'_m(\xi_n b_1) \\ I'_m(\xi_n b_1) \end{array} \right\} D_{mn}^{\rho \lessgtr} \quad (3.72)$$

$$w_n I_m(w_n b_1) E_{mn} = -M_c(l, n) p_n \left\{ \begin{array}{l} K_m(p_n b_1) \\ I_m(p_n b_1) \end{array} \right\} C_{mn}^{\rho \lessgtr}, \quad (3.73)$$

where

$$M_s(l, n) = \frac{2}{h} [q_n \int_0^c \sin(q_n z) \sin(w_l z) dz + \alpha_n \int_c^h \sin(p_n(h - z)) \sin(w_l z) dz] \quad (3.74)$$

$$M_c(l, n) = \frac{2}{h} [p_n \int_0^c \cos(q_n z) \cos(w_l z) dz - \alpha_n \int_c^h \cos(p_n(h - z)) \cos(w_l z) dz] \quad (3.75)$$

$$M_r(l, n) = \frac{2}{h} \int_0^c \sin(\nu_n z) \sin(w_l z) dz \quad (3.76)$$

3.3 Green's function

The second and the most challenging step to the solution of the NDT problem with an integral equation method is the Green's function construction. As defined in Section 2.6, a Green's function is a component of the electric field radiated by an electric source. In this section we are interested in constructing the Green's function for an electric dipole situated in a tube of finite length $c_2 - c_1$ and thickness $b_2 - b_1$ (Fig. 6.3). The Green's function for a conducting plate with a borehole can be considered as a special case of an infinitely thick tube. The infinite thickness can be approximated by setting it sufficiently large with respect to the penetration depth ($> 3\delta$).

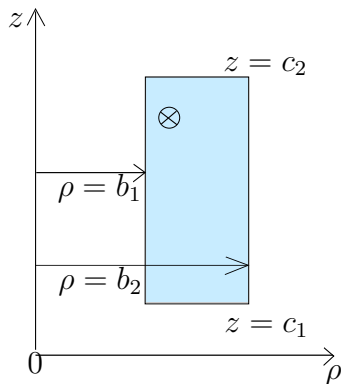


Figure 3.6: Radial cross section of a tube of finite length. An electric dipole with φ orientation

In order to construct the Green's function for the configuration of our interest, we have divided the problem into two sub-problems. First, a conducting plate, truncated at a remote radial distance with an electric dipole is assumed. At this step, the electric field radiated by the dipole, as well as the field reflected by the air-plate interfaces are determined. Second, the internal and external radial interfaces of the tube are introduced and considering the field calculated at the first step as an excitation field, the reflection due to these interfaces is calculated.

3.3.1 Electric dipole in conducting plate

Fig. 6.4 sketches the configuration of the first sub-problem. We assume a homogeneous, non-magnetic and conducting plate of conductivity σ and thickness $c_2 - c_1$. An electric dipole with orientation along φ is located at $(\rho', 0, z')$. Moreover, the domain is truncated at a distance from the source where the field is negligible.

The approach followed for the field calculation is similar to the one followed for the induction problem in Section 3.2. The domain is separated into four different regions

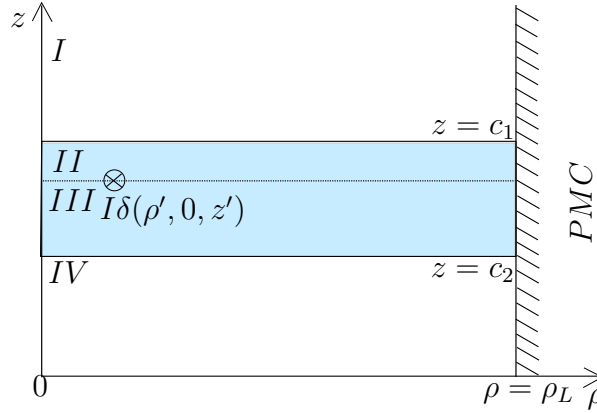


Figure 3.7: Radial cross-section of a conducting plate of thickness $c_2 - c_1$, with an electric dipole of φ -orientation located at $(\rho', 0, z')$.

(Fig. 6.4), where the field takes different expressions. The formulation used is the one of a scalar potential in the air regions which satisfies the Laplace equation and that of an SOVP in the conducting regions that satisfy the Helmholtz equation. This time, the potentials are expressed as modal expansions of the J -Bessel functions. Their expressions take the form

$$\begin{aligned} \phi = & \sum_{m=-\infty}^{m=\infty} \sum_{n=1}^{\infty} [A_{mn} e^{\kappa_n z} + B_{mn} e^{-\kappa_n z}] [C_{mn} J_m(\kappa_n \rho) + D_{mn} Y_m(\kappa_n \rho)] e^{jm\varphi} \\ & + \sum_{m=-\infty, m \neq 0}^{m=\infty} [A_m + B_m z] [C_m \rho^m + D_m \rho^{-m}] e^{jm\varphi} + [A_m + B_m z] [C \ln \rho + D] \end{aligned} \quad (3.77)$$

and

$$\begin{aligned} W_{a,b} = & \sum_{m=-\infty}^{m=\infty} \sum_{n=1}^{\infty} [A_{mn} e^{v_n z} + B_{mn} e^{-v_n z}] [C_n J_m(\kappa_n \rho) + D_n Y_m(\kappa_n \rho)] e^{jm\varphi} \\ & + \sum_{m=-\infty}^{m=\infty} [A_m e^{-kz} + B_m e^{kz}] [C_m \rho^m + D_m \rho^{-m}] e^{jm\varphi}, \end{aligned} \quad (3.78)$$

with $v_n^2 = \kappa_n^2 + k^2$.

From a physical point of view, the scalar potentials ϕ^I in region I and ϕ^{IV} in region IV represent the field transmitted through the interfaces $z = c_2$ and $z = c_1$, respectively, whereas the potentials W_a and W_b represent the TE and TM terms of the field in the conducting regions, respectively. As far as the TEM terms that may appear, they are added only in one of the potentials W_a or W_b , since for both potentials the TEM terms give the same expression of the field. In this work we choose to add them in the W_b potential. In the conducting regions, the field is the superposition of the field radiated by the dipole and the reflection due to the air-conductor interfaces. Thus, with regard to

(3.77) and (3.78) the potentials in regions $I - IV$ are written as

$$\begin{aligned}\phi^I = & \sum_{m=-\infty}^{m=\infty} \sum_{n=1}^{\infty} P_{mn} e^{-\kappa_n(z-z')} J_m(\kappa_n \rho) e^{jm\varphi} \\ & + \sum_{m=-\infty}^{m=\infty} (P_m^{(0)} z + Q_m^{(0)}) \rho^{-m} e^{jm\varphi} ; \quad z \geq c_2\end{aligned}\quad (3.79)$$

$$W_a^{II} = \sum_{m=-\infty}^{m=\infty} \sum_{n=1}^{\infty} (A_{mn} e^{-v_n(z-z')} + B_{mn} e^{v_n(z-z')}) J_m(\kappa_n \rho) e^{jm\varphi} ; \quad z' \leq z \leq c_2 \quad (3.80)$$

$$\begin{aligned}W_b^{II} = & \sum_{m=-\infty}^{m=\infty} \sum_{n=1}^{\infty} (C_{mn} e^{-r_n(z-z')} + D_{mn} e^{r_n(z-z')}) J_m(s_n \rho) e^{jm\varphi} \\ & + \sum_{m=-\infty}^{m=\infty} (C_m^{(0)} e^{-k(z-z')} + D_m^{(0)} e^{k(z-z')}) \rho^{-m} e^{jm\varphi} ; \quad z' \leq z \leq c_2\end{aligned}\quad (3.81)$$

$$W_a^{III} = \sum_{m=-\infty}^{m=\infty} \sum_{n=1}^{\infty} (E_{mn} e^{-v_n(z-z')} + F_{mn} e^{v_n(z-z')}) J_m(\kappa_n \rho) e^{jm\varphi} ; \quad c_1 \leq z \leq z' \quad (3.82)$$

$$\begin{aligned}W_b^{III} = & \sum_{m=-\infty}^{m=\infty} \sum_{n=1}^{\infty} (L_{mn} e^{-r_n(z-z')} + M_{mn} e^{r_n(z-z')}) J_m(s_n \rho) e^{jm\varphi} \\ & + \sum_{m=-\infty}^{m=\infty} (L_m^{(0)} e^{-k(z-z')} + M_m^{(0)} e^{k(z-z')}) \rho^{-m} e^{jm\varphi} ; \quad c_1 \leq z \leq z'\end{aligned}\quad (3.83)$$

$$\begin{aligned}\phi^{IV} = & \sum_{m=-\infty}^{m=\infty} \sum_{n=1}^{\infty} N_{mn} e^{\kappa_n(z-z')} J_m(\kappa_n \rho) e^{jm\varphi} \\ & + \sum_{m=-\infty}^{m=\infty} (N_m^{(0)} z + O_m^{(0)}) \rho^{-m} e^{jm\varphi} ; \quad z \geq c_2\end{aligned}\quad (3.84)$$

Conditions at truncation boundary

A zero tangential magnetic field is considered at the truncation interface. The PMC condition at $\rho = \rho_L$ leads to less complex expressions of the potentials since the TEM terms are neglected. More specifically, the PMC condition for the air **region I** results in

$$\begin{aligned}B_\phi^I|_{\rho=\rho_L} = 0 \Leftrightarrow & \sum_{n=1}^{\infty} \frac{jm}{\rho_L} P_{mn} \kappa_n e^{-\kappa_n(z-z')} J_m(\kappa_n \rho_L) + \frac{jm}{\rho_L} (P_m^{(0)} z + Q_m^{(0)}) \rho_L^{-m} = 0 \Leftrightarrow \\ & \boxed{P_m^{(0)} = Q_m^{(0)} = 0} \quad \text{and} \quad \boxed{J_m(\kappa_n \rho_L) = 0}\end{aligned}\quad (3.85)$$

and similarly for **region IV** it is given as

$$\boxed{N_m^{(0)} = O_m^{(0)} = 0}. \quad (3.86)$$

As far as the conducting regions are concerned, if we take (6.27) into account the PMC condition at $\rho = \rho_L$ leads for **region II** to

$$\begin{aligned} B_\phi^{II}|_{\rho=\rho_L} = 0 \Leftrightarrow & - \sum_{n=1}^{\infty} k^2 (C_{mn} e^{-r_n(z-z')} + D_{mn} e^{r_n(z-z')}) s_n J'_m(s_n \rho_L) \\ & + k^2 m (C_m^{(0)} e^{-k(z-z')} + D_m^{(0)} e^{k(z-z')}) \rho_L^{-m-1} = 0, \end{aligned}$$

which holds $\forall z$ and for $\rho_L \neq 0$ and thus, we obtain

$$\boxed{C_m^{(0)} = D_m^{(0)} = 0} \quad \text{and} \quad \boxed{J'_m(s_n \rho_L) = 0}. \quad (3.87)$$

Similarly, in **region III** the TEM terms expansion coefficients vanish:

$$\boxed{L_m^{(0)} = M_m^{(0)} = 0}. \quad (3.88)$$

Continuity at $z = z'$

In order to define the field in the entire domain one needs to calculate the ten unknown expansion coefficients of the potentials (6.20)-(6.25). Consequently, one needs ten independent relations between the expansion coefficients. The boundary conditions at the conductor-air interfaces $z = c_1$ and $z = c_2$ as well as at the fictitious interface that divides the conducting plate into two regions at the level of the source can provide us with these relations. Thus, the continuity of the magnetic field at the interface $z = z'$ gives

$$\begin{aligned} H_\rho^{III}|_{z=z'} - H_\rho^{II}|_{z=z'} = -\delta(\rho - \rho')\delta(\varphi) \Leftrightarrow & \\ & \sum_{i=1}^{\infty} [(-E_{mn} + F_{mn} + A_{mn} - B_{mn}) v_n \kappa_n J'_m(\kappa_n \rho) \\ & + \sum_{i=1}^{\infty} \frac{k^2 j m}{\rho} (L_{mn} + M_{mn} - C_{mn} - D_{mn}) J_m(s_n \rho)] = -\frac{\mu_0}{2\pi\rho} \delta(\rho - \rho') \end{aligned} \quad (3.89)$$

$$\begin{aligned} H_\varphi^{III}|_{z=z'} - H_\varphi^{II}|_{z=z'} = 0 \Leftrightarrow & \sum_{i=1}^{\infty} \frac{j m}{\rho} (-E_{mn} + F_{mn} + A_{mn} - B_{mn}) v_n J_m(\kappa_n \rho) \\ & - \sum_{i=1}^{\infty} k^2 (L_{mn} + M_{mn} - C_{mn} - D_{mn}) s_n J'_m(s_n \rho) = 0 \end{aligned} \quad (3.90)$$

$$\begin{aligned} B_z^{III}|_{z=z'} - B_z^{II}|_{z=z'} = 0 \Leftrightarrow & \sum_{i=1}^{\infty} [(E_{mn} + F_{mn} - A_{mn} - B_{mn}) \kappa_n^2 J_m(\kappa_n \rho)] = 0 \Leftrightarrow \\ & E_{mn} + F_{mn} = A_{mn} + B_{mn}. \end{aligned} \quad (3.91)$$

Plus, by using (3.91) the continuity of E_φ gives

$$\begin{aligned} E_\varphi^{III}|_{z=z'} - E_\varphi^{II}|_{z=z'} = 0 &\Leftrightarrow \sum_{i=1}^{\infty} [(E_{mn} + F_{mn} - A_{mn} - B_{mn})\kappa_n J'_m(\kappa_n \rho) \\ &+ \sum_{i=1}^{\infty} \frac{jm}{\rho} (-L_{mn} + M_{mn} + C_{mn} - D_{mn}) r_n J_m(s_n \rho)] = 0 \\ &- L_{mn} + M_{mn} = D_{mn} - C_{mn}. \end{aligned} \quad (3.92)$$

If we substitute (3.91) and (3.92) into (3.89) and (3.90) we obtain

$$\sum_{i=1}^{\infty} [2(A_{mn} - E_{mn})v_n \kappa_n J'_m(\kappa_n \rho) - 2\frac{k^2}{\rho} jm(C_{mn} - L_{mn}) J_m(s_n \rho)] = -\frac{\mu_0}{2\pi\rho} \delta(\rho - \rho') \quad (3.93)$$

and

$$\sum_{i=1}^{\infty} [2\frac{jm}{\rho} (A_{mn} - E_{mn}) v_n J_m(\kappa_n \rho) + 2k^2 (C_{mn} - L_{mn}) s_n J'_m(s_n \rho)] = 0 \quad (3.94)$$

Starting from (3.93) and (3.94) and after some algebra an expression for $A_{mn} - E_{mn}$ and $C_{mn} - L_{mn}$ can be derived. Therefore, calculating $\kappa_l J'_m(\kappa_l \rho) \times (3.93) - \frac{jm}{\rho} J_m(\kappa_l \rho) \times (3.94)$ we have

$$\begin{aligned} &\sum_{i=1}^{\infty} [2(A_{mn} - E_{mn})v_n \kappa_n \kappa_l J'_m(\kappa_n \rho) J'_m(\kappa_l \rho) - 2\frac{k^2}{\rho} jm(C_{mn} - L_{mn}) \kappa_l J_m(s_n \rho) J'_m(\kappa_l \rho)] \\ &+ \sum_{i=1}^{\infty} [2\frac{m^2}{\rho^2} (A_{mn} - E_{mn}) v_n J_m(\kappa_n \rho) J_m(\kappa_l \rho) - 2\frac{k^2 jm}{\rho} (C_{mn} - L_{mn}) s_n J'_m(s_n \rho) J_m(\kappa_l \rho)] \\ &= -\frac{\mu_0}{2\pi\rho} \kappa_l J'_m(\kappa_l \rho) \delta(\rho - \rho') \Leftrightarrow \\ &\sum_{i=1}^{\infty} [2(A_{mn} - E_{mn})v_n \kappa_n \kappa_l J'_m(\kappa_n \rho) J'_m(\kappa_l \rho) - 2\frac{k^2}{\rho} jm(C_{mn} - L_{mn}) \frac{d}{d\rho} (J_m(s_n \rho) J_m(\kappa_l \rho))] \\ &+ \sum_{i=1}^{\infty} 2\frac{m^2}{\rho^2} (A_{mn} - E_{mn}) v_n J_m(\kappa_n \rho) J_m(\kappa_l \rho) = -\frac{\mu_0}{2\pi\rho} \kappa_l J'_m(\kappa_l \rho) \delta(\rho - \rho') \end{aligned} \quad (3.95)$$

One can integrate (3.95) $\times \rho$ over ρ from 0 to ρ_L , which yields

$$\begin{aligned} &\sum_{i=1}^{\infty} 2(A_{mn} - E_{mn}) v_n \int_0^{\rho_L} [\kappa_n \kappa_l \rho J'_m(\kappa_n \rho) J'_m(\kappa_l \rho) + \frac{m^2}{\rho} J_m(\kappa_n \rho) J_m(\kappa_l \rho)] d\rho \\ &- \sum_{i=1}^{\infty} 2k^2 jm(C_{mn} - L_{mn}) \int_0^{\rho_L} \frac{d}{d\rho} [J_m(s_n \rho) J_m(\kappa_l \rho)] d\rho = -\frac{\mu_0}{2\pi} \kappa_l J'_m(\kappa_l \rho'). \end{aligned} \quad (3.96)$$

Furthermore, the left side second sum of (3.96) vanish:

$$m \int_0^{\rho_L} \frac{d}{d\rho} [J_m(s_n\rho) J_m(\kappa_l\rho)] d\rho = 0 \quad \forall m \quad (3.97)$$

since $J_m(\kappa_l\rho_L) = 0$ and $m J_m(0) = 0 \quad \forall m$.

We will calculate now $\int_0^{\rho_L} \kappa_n \kappa_l \rho J'_m(\kappa_n \rho) J'_m(\kappa_l \rho) d\rho$ separately:

$$\begin{aligned} \int_0^{\rho_L} \kappa_n \kappa_l \rho J'_m(\kappa_n \rho) J'_m(\kappa_l \rho) d\rho &= \int_0^{\rho_L} \kappa_n \rho J'_m(\kappa_n \rho) \frac{d}{d\rho} [J_m(\kappa_l \rho)] d\rho = \\ &= [\kappa_n \rho J'_m(\kappa_n \rho) J_m(\kappa_l \rho)]_0^{\rho_L} - \int_0^{\rho_L} \kappa_n \frac{d}{d\rho} [\rho J'_m(\kappa_n \rho)] J_m(\kappa_l \rho) d\rho, \end{aligned} \quad (3.98)$$

where the term $[\kappa_n \rho J'_m(\kappa_n \rho) J_m(\kappa_l \rho)]_0^{\rho_L}$ is zero since

- $J_m(\kappa_l \rho_L) = 0 \quad \forall m$,
- $J_m(0) = 0 \quad \forall m \neq 0$ (see Appendix ??) and
- $J'_0(0) = -J_1(0) = 0$ (see Appendix ??)

and therefore (3.98) becomes

$$\int_0^{\rho_L} \kappa_n \kappa_l \rho J'_m(\kappa_n \rho) J'_m(\kappa_l \rho) d\rho = - \int_0^{\rho_L} \frac{1}{\rho} [(\kappa_n \rho) J'_m(\kappa_n \rho) + (\kappa_n \rho)^2 J''_m(\kappa_n \rho)] J_m(\kappa_l \rho) d\rho. \quad (3.99)$$

It is also known that the Bessel equations are solutions of (Appendix ??)

$$x^2 \frac{d^2 J_m(x)}{dx^2} + x \frac{d J_m(x)}{dx} + (x^2 - m^2) J_m(x) = 0. \quad (3.100)$$

Also, from (3.99) and (3.100)

$$\int_0^{\rho_L} \kappa_n \kappa_l \rho J'_m(\kappa_n \rho) J'_m(\kappa_l \rho) d\rho = \int_0^{\rho_L} \frac{1}{\rho} [(\kappa_n \rho)^2 - m^2] J_m(\kappa_n \rho) J_m(\kappa_l \rho) d\rho \quad (3.101)$$

Additionally, one can find in mathematical handbooks that [AS65]

$$\int_0^{\rho_L} \rho J_m(\alpha_n \rho) J_m(\alpha_l \rho) d\rho = \begin{cases} 0 & n \neq l, m > -1 \\ \frac{\rho_L^2}{2} J_m'^2(\kappa_n \rho_L) & n = l, b = 0, m > -1 \\ \frac{\rho_L^2}{2\kappa_n^2} \left[\frac{a^2}{b^2} + \kappa_n^2 - \frac{m^2}{\rho_L^2} \right] J_m^2(\kappa_n \rho_L) & n = l, b \neq 0, m \geq -1 \end{cases}, \quad (3.102)$$

where $\kappa_1, \kappa_2, \dots$ are the positive zeros of $a J_m(\kappa_n \rho_L) + b \kappa_n \rho_L J'_m(\kappa_n \rho_L) = 0$. Moreover, the Bessel function J_m is related to its derivative via the relation

$$x J'_m(x) = m J_m(x) - x J_{m+1}(x). \quad (3.103)$$

Finally, combination of (3.96), (3.101), (3.102) and (3.103) gives

$$\begin{aligned} \sum_{i=1}^{\infty} 2(A_{mn} - E_{mn})v_n \kappa_n^2 \int_0^{\rho_L} \rho J_m(\kappa_n \rho) J_m(\kappa_l \rho) d\rho &= -\frac{\mu_0}{2\pi} \kappa_l J'_m(\kappa_l \rho') \Leftrightarrow \\ 2(A_{mn} - E_{mn})v_n \kappa_n^2 \frac{\rho_L^2}{2} J_{m+1}(\kappa_n \rho_L) &= -\frac{\mu_0}{2\pi} \kappa_l J'_m(\kappa_l \rho') \\ A_{mn} - E_{mn} &= -\frac{\mu_0}{2\pi v_n \rho_L^2 \kappa_n} \frac{J'_m(\kappa_n \rho')}{J_{m+1}^2(\kappa_n \rho_L)}. \end{aligned} \quad (3.104)$$

Equally, in order to find an expression for $A_{mn} - E_{mn}$ we calculate now $\frac{jm}{\rho} J_m(s_l \rho) \times (3.93) + s_l J'_m(s_l \rho) \times (3.94)$

$$\begin{aligned} \sum_{i=1}^{\infty} [2 \frac{jm}{\rho} (A_{mn} - E_{mn}) v_n \kappa_n J_m(s_l \rho) J'_m(\kappa_n \rho) + 2 \frac{k^2 m^2}{\rho^2} (C_{mn} - L_{mn}) J_m(s_n \rho) J_m(s_l \rho)] \\ + \sum_{i=1}^{\infty} [2 \frac{jm}{\rho} (A_{mn} - E_{mn}) v_n s_l J_m(\kappa_n \rho) J'_m(s_l \rho) + 2 k^2 (C_{mn} - L_{mn}) s_n s_l J'_m(s_n \rho) J'_m(s_l \rho)] \\ = -\frac{\mu_0}{2\pi} \frac{jm}{\rho^2} J_m(s_l \rho) \delta(\rho - \rho'). \end{aligned} \quad (3.105)$$

Grouping the terms in (3.105) and integrating over ρ from 0 to ρ_L we get

$$\begin{aligned} \sum_{i=1}^{\infty} 2jm(A_{mn} - E_{mn})v \int_0^{\rho_L} \frac{d}{d\rho} [J_m(s_l \rho) J_m(\kappa_n \rho)] d\rho + \\ \sum_{i=1}^{\infty} 2k^2(C_{mn} - L_{mn}) \int_0^{\rho_L} [(s_n s_l \rho J'_m(s_n \rho) J'_m(s_l \rho) + \frac{m^2}{\rho} J_m(s_n \rho) J_m(s_l \rho))] d\rho \\ = -\frac{\mu_0}{2\pi \rho'} jm J_m(s_l \rho'). \end{aligned} \quad (3.106)$$

Finally, if we substitute (3.97) and (3.101) in (3.106) we obtain

$$\begin{aligned} \sum_{i=1}^{\infty} 2k^2(C_{mn} - L_{mn}) \int_0^{\rho_L} \frac{1}{\rho} [(s_n \rho)^2 - m^2] + \frac{m^2}{\rho} J_m(s_n \rho) J_m(s_l \rho) d\rho &= -\frac{\mu_0}{2\pi \rho'} jm J_m(s_l \rho') \Leftrightarrow \\ \sum_{i=1}^{\infty} 2k^2(C_{mn} - L_{mn}) \int_0^{\rho_L} s_n^2 \rho J_m(s_n \rho) J_m(s_l \rho) d\rho &= -\frac{\mu_0}{2\pi \rho'} jm J_m(s_l \rho') \stackrel{(3.102)}{\Leftrightarrow} \\ (C_{mn} - L_{mn}) k^2 ((s_n \rho_L)^2 - m^2) J_m^2(s_n \rho_L) &= -\frac{\mu_0}{2\pi \rho'} jm J_m(s_l \rho') \Leftrightarrow \\ C_{mn} - L_{mn} &= -j \frac{\mu_0 m}{2\pi k^2 ((s_n \rho_L)^2 - m^2) \rho'} \frac{J_m(s_n \rho')}{J_m^2(s_n \rho_L)}. \end{aligned} \quad (3.107)$$

Continuity at $z = c_1$ and $z = c_2$

The continuity of the field at the air-conductor interfaces provides us with the rest of the relations that we need to calculate the field. Accordingly, the zero normal electric current density condition on $z = c_1$ yields

$$\begin{aligned} J_z|_{z=c_1} = -j\omega\sigma[\nabla \times W]_z &= -s_n^2(L_{mn}e^{-r_n(c_1-z')} + M_{mn}e^{r_n(c_1-z')})J_m(s_n\rho) = 0 \Leftrightarrow \\ M_{mn} &= -L_{mn}e^{-2r_n(c_1-z')}. \end{aligned} \quad (3.108)$$

The same condition in region IV for $z = c_2$ gives

$$D_{mn} = -C_{mn}e^{-2r_n(c_2-z')}. \quad (3.109)$$

If we now sum up (3.92), (3.108) and (3.109) we have

$$L_{mn} = C_{mn} \frac{e^{-2r_n(c_2-z')} + 1}{e^{-2r_n(c_1-z')} + 1} \quad (3.110)$$

and using the relations (3.107) - (3.110) we arrive at the final expressions for the TM potentials expansion coefficients

$$C_{mn} = -j \frac{\mu_0 m}{2\pi k^2(s_n^2\rho_L^2 - m^2)\rho'} \frac{J_m(s_n\rho')}{J_m(s_n\rho_L)} \frac{e^{-2r_n(c_1-z')} + 1}{(e^{-2r_nc_1} - e^{-2r_nc_2})e^{2r_n z'}} \quad (3.111)$$

$$L_{mn} = -j \frac{\mu_0 m}{2\pi k^2(s_n^2\rho_L^2 - m^2)\rho'} \frac{J_m(s_n\rho')}{J_m(s_n\rho_L)} \frac{e^{-2r_n(c_2-z')} + 1}{(e^{-2r_nc_1} - e^{-2r_nc_2})e^{2r_n z'}} \quad (3.112)$$

$$D_{mn} = j \frac{\mu_0 m}{2\pi k^2(s_n^2\rho_L^2 - m^2)\rho'} \frac{J_m(s_n\rho')}{J_m(s_n\rho_L)} \frac{e^{-2r_n(c_1-z')} + 1}{e^{-2r_n(c_1-c_2)} - 1} \quad (3.113)$$

$$M_{mn} = j \frac{\mu_0 m}{2\pi k^2(s_n^2\rho_L^2 - m^2)\rho'} \frac{J_m(s_n\rho')}{J_m(s_n\rho_L)} \frac{e^{-2r_n(c_2-z')} + 1}{1 - e^{-2r_n(c_1-c_2)}}. \quad (3.114)$$

Furthermore, the continuity of the magnetic field at $z = c_1$ gives

$$\begin{aligned} H_\rho^{III}|_{z=c_1} &= H_\rho^{IV}|_{z=c_1} \stackrel{(3.108)}{\Leftrightarrow} \\ \sum_{i=1}^{\infty} (-E_{mn}e^{-v_n(c_1-z')} + F_i e^{v_n(c_1-z')})v_n \kappa_n J'_m(\kappa_n\rho) &= \sum_{i=1}^{\infty} N_{mn} \kappa_n e^{\kappa_n(c_1-z')} J'_m(\kappa_n\rho) \Leftrightarrow \\ v_n(-E_{mn}e^{-v_n(c_1-z')} + F_i e^{v_n(c_1-z')}) &= N_{mn} e^{\kappa_n(c_1-z')} \end{aligned} \quad (3.115)$$

$$\begin{aligned} B_z^{III}|_{z=c_1} &= B_z^{IV}|_{z=c_1} \Leftrightarrow \\ \sum_{i=1}^{\infty} [(E_{mn}e^{-v_n(c_1-z')} + F_i e^{v_n(c_1-z')})\kappa_n^2 J_m(\kappa_n\rho)] &= \sum_{i=1}^{\infty} N_{mn} \kappa_n e^{\kappa_n(c_1-z')} \Leftrightarrow \\ \kappa_n(E_{mn}e^{-v_n(c_1-z')} + F_i e^{v_n(c_1-z')}) &= N_{mn} e^{\kappa_n(c_1-z')} \end{aligned} \quad (3.116)$$

By subtracting (3.115) from (3.116)

$$F_i = -E_{mn} \frac{\kappa_n + v_n}{\kappa_n - v_n} e^{-2v_n(c_1 - z')} \quad (3.117)$$

and from the combination of (3.115) and (3.117) we obtain the relation between $N_{mn} - E_{mn}$

$$N_{mn} = -E_{mn} \frac{2\kappa_n v_n}{\kappa_n - v_n} e^{-(\kappa_n + v_n)(c_1 - z')}. \quad (3.118)$$

In the same fashion, the boundary conditions at $z = c_2$ yield

$$\begin{aligned} H_\rho^{III} \Big|_{z=c_2} &= H_\rho^{IV} \Big|_{z=c_2} \stackrel{(3.109)}{\Leftrightarrow} \\ \sum_{i=1}^{\infty} (-A_{mn} e^{-v_n(c_2 - z')} + B_{mn} e^{v_n(c_2 - z')}) v_n \kappa_n J'_m(\kappa_n \rho) &= \sum_{i=1}^{\infty} P_{mn} \kappa_n e^{-\kappa_n(c_2 - z')} J'_m(\kappa_n \rho) \Leftrightarrow \\ v_n (-A_{mn} e^{-v_n(c_2 - z')} + B_{mn} e^{v_n(c_2 - z')}) &= P_{mn} e^{-\kappa_n(c_2 - z')} \end{aligned} \quad (3.119)$$

$$\begin{aligned} B_z^{III} \Big|_{z=c_2} &= B_z^{IV} \Big|_{z=c_2} \Leftrightarrow \\ \sum_{i=1}^{\infty} [(A_{mn} e^{-v_n(c_2 - z')} + B_{mn} e^{v_n(c_2 - z')}) \kappa_n^2 J_m(\kappa_n \rho)] &= - \sum_{i=1}^{\infty} P_{mn} \kappa_n e^{-\kappa_n(c_2 - z')} \Leftrightarrow \\ \kappa_n (A_{mn} e^{-v_n(c_2 - z')} + B_{mn} e^{v_n(c_2 - z')}) &= -P_{mn} e^{-\kappa_n(c_2 - z')}. \end{aligned} \quad (3.120)$$

If we sum (3.120) and (3.119) we get

$$B_{mn} = -A_{mn} \frac{\kappa_n - v_n}{\kappa_n + v_n} e^{-2v_n(c_2 - z')} \quad (3.121)$$

And by substituting (3.121) in (3.119) we obtain

$$P_{mn} = -A_{mn} \frac{2\kappa_n v_n}{\kappa_n - v_n} e^{(\kappa_n - v_n)(c_2 - z')}. \quad (3.122)$$

From (3.91), (3.117) and (3.121) the $E_{mn} - A_{mn}$ relation reads

$$E_{mn} = A_{mn} \frac{1 - \frac{\kappa_n - v_n}{\kappa_n + v_n} e^{-2v_n(c_2 - z')}}{1 - \frac{\kappa_n + v_n}{\kappa_n - v_n} e^{-2v_n(c_1 - z')}}. \quad (3.123)$$

In the end, the expansion coefficients of the TE terms are defined by combining (3.104), (3.117), (3.118), (3.121) and (3.123):

$$A_{mn} = -\frac{\mu_0}{2\pi v_n \rho_L^2 \kappa_n} \frac{J'_m(\kappa_n \rho')}{J_{m+1}^2(\kappa_n \rho_L)} \frac{1 - \frac{\kappa_n + v_n}{\kappa_n - v_n} e^{-2v_n(c_1 - z')}}{\left(\frac{\kappa_n - v_n}{\kappa_n + v_n} e^{-2v_n c_2} - \frac{\kappa_n + v_n}{\kappa_n - v_n} e^{-2v_n c_1} \right) e^{2v_n z'}} \quad (3.124)$$

$$B_{mn} = \frac{\mu_0}{2\pi v_n \rho_L^2 \kappa_n} \frac{J'_m(\kappa_n \rho')}{J_{m+1}^2(\kappa_n \rho_L)} \frac{\frac{\kappa_n - v_n}{\kappa_n + v_n} - e^{-2v_n(c_1 - z')}}{\frac{\kappa_n - v_n}{\kappa_n + v_n} - \frac{\kappa_n + v_n}{\kappa_n - v_n} e^{-2v_n(c_1 - c_2)}} \quad (3.125)$$

$$E_{mn} = -\frac{\mu_0}{2\pi v_n \rho_L^2 \kappa_n} \frac{J'_m(\kappa_n \rho')}{J_{m+1}^2(\kappa_n \rho_L)} \frac{1 - \frac{\kappa_n - v_n}{\kappa_n + v_n} e^{-2v_n(c_2 - z')}}{\left(\frac{\kappa_n - v_n}{\kappa_n + v_n} e^{-2v_n c_2} - \frac{\kappa_n + v_n}{\kappa_n - v_n} e^{-2v_n c_1} \right) e^{2v_n z'}} \quad (3.126)$$

$$F_{mn} = \frac{\mu_0}{2\pi v_n \rho_L^2 \kappa_n} \frac{J'_m(\kappa_n \rho')}{J_{m+1}^2(\kappa_n \rho_L)} \frac{\frac{\kappa_n + v_n}{\kappa_n - v_n} - e^{-2v_n(c_2 - z')}}{\frac{\kappa_n - v_n}{\kappa_n + v_n} e^{-2v_n(c_2 - c_1)} - \frac{\kappa_n + v_n}{\kappa_n - v_n}} \quad (3.127)$$

$$N_{mn} = \frac{\mu_0}{2\pi v_n \rho_L^2 \kappa_n} \frac{J'_m(\kappa_n \rho')}{J_{m+1}^2(\kappa_n \rho_L)} \frac{\left(\frac{2\kappa_n v_n}{\kappa_n - v_n} - \frac{2\kappa_n v_n}{\kappa_n + v_n} e^{-2v_n(c_2 - z')} \right) e^{-(\kappa_n + v_n)c_1} e^{(\kappa_n + v_n)z'}}{\frac{\kappa_n - v_n}{\kappa_n + v_n} e^{-2v_n c_2} - \frac{\kappa_n + v_n}{\kappa_n - v_n} e^{-2v_n c_1}} \quad (3.128)$$

$$P_{mn} = \frac{\mu_0}{2\pi v_n \rho_L^2 \kappa_n} \frac{J'_m(\kappa_n \rho')}{J_{m+1}^2(\kappa_n \rho_L)} \frac{\left(\frac{2\kappa_n v_n}{\kappa_n + v_n} - \frac{2\kappa_n v_n}{\kappa_n - v_n} e^{-2v_n(c_1 - z')} \right) e^{(\kappa_n - v_n)c_2} e^{-(\kappa_n + v_n)z'}}{\frac{\kappa_n - v_n}{\kappa_n + v_n} e^{-2v_n c_2} - \frac{\kappa_n + v_n}{\kappa_n - v_n} e^{-2v_n c_1}} \quad (3.129)$$

3.3.2 Reflection of the radial interfaces

Solving the sub-problem of the infinite conducting plate with an electric dipole located in it, we have calculated the field radiated by the dipole as well as the reflection due to the air-conductor interfaces of the plate. In the second sub-problem we introduce two radial interfaces and we aim at calculating the reflection due to these interfaces. The field calculated in the first problem will be referred to conventionally as "source field" in this text since it acts as an excitation term for the perturbation problem that we consider in this subsection.

$$\begin{aligned} \phi^{I,sc} &= \sum_{m=-\infty}^{m=\infty} \sum_{i=1}^{\infty} (L_{mn}^{\rho^<} \sin(w_n z) + A_{mn}^{\rho^<} \cos(w_n z)) I_m(w_n \rho) e^{jm\varphi} \\ &+ \sum_{m=-\infty}^{m=\infty} (A^{(0)} z + B^{(0)}) \rho^m e^{jm\varphi} \quad ; \quad 0 \leq z \leq h \end{aligned} \quad (3.130)$$

$$\begin{aligned} \phi^{II,sc} &= \sum_{m=-\infty}^{m=\infty} \sum_{n=1}^{\infty} (B_{mn}^{\rho^{\leqslant}} \sin(p_n(h - z)) + M_{mn}^{\rho^{\leqslant}} \cos(p_n(h - z))) \begin{Bmatrix} K_m(p_n \rho) \\ I_m(p_n \rho) \end{Bmatrix} e^{jm\varphi} \\ &+ \sum_{m=-\infty}^{m=\infty} (C^{(0)} z + D^{(0)}) \begin{Bmatrix} \rho^{-m} \\ \rho^m \end{Bmatrix} e^{jm\varphi} \quad ; \quad c_2 \leq z \leq h \end{aligned} \quad (3.131)$$

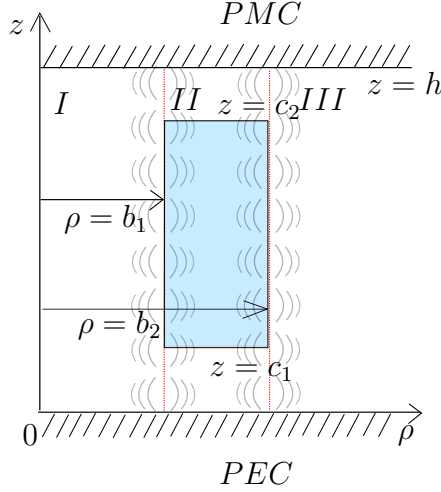


Figure 3.8: Radial cross-section of a finite tube of thickness $b_2 - b_1$ and height $c_2 - c_1$. An initial field equal to this calculated in Section 3.3.1 is considered in region II.

$$W_a^{II,sc} = \sum_{m=-\infty}^{m=\infty} \sum_{n=1}^{\infty} (N_m^{\rho \lessgtr} \sin(q_n z) + C_m^{\rho \lessgtr} \cos(q_n z)) \begin{Bmatrix} K_m(p_n \rho) \\ I_m(p_n \rho) \end{Bmatrix} e^{jm\varphi} + \sum_{m=-\infty}^{m=\infty} (E^{(0)} z + F^{(0)}) \begin{Bmatrix} K_m(k \rho) \\ I_m(k \rho) \end{Bmatrix} e^{jm\varphi} ; \quad c_1 \leq z \leq c_2 \quad (3.132)$$

$$W_b^{II,sc} = \sum_{m=-\infty}^{m=\infty} \sum_{n=1}^{\infty} (D_m^{\rho \lessgtr} \sin(\nu_n z) + O_m^{\rho \lessgtr} \cos(\nu_n z)) \begin{Bmatrix} K_m(\xi_n \rho) \\ I_m(\xi_n \rho) \end{Bmatrix} e^{jm\varphi} + \sum_{m=-\infty}^{m=\infty} (L^{(0)} z + M^{(0)}) \begin{Bmatrix} K_m(k \rho) \\ I_m(k \rho) \end{Bmatrix} e^{jm\varphi} + \sum_{m=-\infty}^{m=\infty} (P^{(0)} \sinh(q_n z) + Q^{(0)} \cosh(q_n z)) \begin{Bmatrix} \rho^{-m} \\ \rho^m \end{Bmatrix} e^{jm\varphi} ; \quad c_1 \leq z \leq c_2 \quad (3.133)$$

$$\phi^{II,sc} = \sum_{m=-\infty}^{m=\infty} \sum_{n=1}^{\infty} (F_m^{\rho \lessgtr} \sin(p_n z) + E_m^{\rho \lessgtr} \cos(p_n z)) \begin{Bmatrix} K_m(p_n \rho) \\ I_m(p_n \rho) \end{Bmatrix} e^{jm\varphi} + \sum_{m=-\infty}^{m=\infty} (N^{(0)} z + R^{(0)}) \begin{Bmatrix} \rho^{-m} \\ \rho^m \end{Bmatrix} e^{jm\varphi} ; \quad 0 \leq z \leq c_1, \quad (3.134)$$

$$\phi^{III,sc} = \sum_{m=-\infty}^{m=\infty} \sum_{i=1}^{\infty} (Q_m^{\rho \gtrless} \sin(w_n z) + P_m^{\rho \gtrless} \cos(w_n z)) K_m(w_n \rho) e^{jm\varphi} + \sum_{m=-\infty}^{m=\infty} (O^{(0)} z + S^{(0)}) \rho^{-m} e^{jm\varphi} ; \quad 0 \leq z \leq h \quad (3.135)$$

where $p_n^2 = q_n^2 + k^2$, $\xi_n^2 = \nu_n^2 + k^2$.

For the sake of simplicity, we will ignore in this subsection the φ dependence of the field. This dependence can be in any case eliminated by multiplying by $e^{-jm\varphi}$ and integrating from $\varphi = 0$ to $\varphi = 2\pi$ any of the boundary conditions at the interfaces $z = 0$ and $z = h$

that we will apply below.

PMC and PEC conditions at truncation interfaces

Like with the previous problems, we start by applying the boundary conditions at the truncation boundaries. In this subproblem we choose to apply PEC conditions at $z = 0$ and PMC conditions at $z = h$. These conditions give in **region I**

$$B_z^I|_{z=0} = 0 \Leftrightarrow \sum_{n=1}^{\infty} L_m^{\rho^<} w_n I_m(w_n \rho) + A^{(0)} \rho^m = 0 \Leftrightarrow [L_m^{\rho^<} = A^{(0)} = 0] \quad (3.136)$$

and

$$B_\rho^I|_{z=h} = 0 \Leftrightarrow \sum_{n=1}^{\infty} A_m^{\rho^<} w_n \cos(w_n h) I'_m(w_n \rho) + B^{(0)} m \rho^{m-1} = 0 \quad (3.137)$$

which yields $[B^{(0)} = 0]$ and $\cos(w_n h) = 0 \Leftrightarrow [w_n = \frac{(2n-1)\pi}{2h}]$. Equally, in **region III** the same conditions result in $[Q_m^{\rho^>} = O^{(0)} = S^{(0)} = 0]$.

Finally, in **region II** we have

$$B_z^{II}|_{z=0} = 0 \Leftrightarrow \sum_{n=1}^{\infty} F_m^{\rho^<} p_n \begin{Bmatrix} K_m(p_n \rho) \\ I_m(p_n \rho) \end{Bmatrix} + N^{(0)} \begin{Bmatrix} \rho^{-m} \\ \rho^m \end{Bmatrix} = 0 \Leftrightarrow [F_m^{\rho^<} = N^{(0)} = 0]. \quad (3.138)$$

$$B_\rho^{II}|_{z=h} = 0 \Leftrightarrow \sum_{n=1}^{\infty} [M_m^{\rho^<} p_n \begin{Bmatrix} K'_m(p_n \rho) \\ I'_m(p_n \rho) \end{Bmatrix} + (C^{(0)} h + D^{(0)}) m \begin{Bmatrix} -\rho^{-m-1} \\ \rho^{m-1} \end{Bmatrix}] = 0 \Leftrightarrow [M_m^{\rho^<} = C^{(0)} h + D^{(0)} = 0]. \quad (3.139)$$

Continuity at $z = c_1$ and $z = c_2$

Furthermore, application of zero normal current density condition at $z = c_1$ and $z = c_2$ leads to the calculation of the ξ_n eigenvalues as well as the zero-order terms and the TEM terms of the W_b potential.

$$\begin{aligned} J_z|_{z=c_2} &= -j\omega\sigma[\nabla \times W]_z = -j\omega\sigma(k^2 W_b - \frac{\partial^2 W_b}{\partial z^2}) = 0 \Leftrightarrow \\ &- \sum_{n=1}^{\infty} \xi_n^2 (D_m^{\rho^<} \sin(\nu_n c_2) + O_m^{\rho^<} \cos(\nu_n c_2)) \begin{Bmatrix} K_m(\xi_n \rho) \\ I_m(\xi_n \rho) \end{Bmatrix} \\ &- k^2 [(L^{(0)} c_2 + M^{(0)}) \begin{Bmatrix} K_m(k \rho) \\ I_m(k \rho) \end{Bmatrix} - (P^{(0)} \sinh(k c_2) + Q^{(0)} \cosh(k c_2)) \begin{Bmatrix} \rho^{-m} \\ \rho^m \end{Bmatrix}] = 0, \end{aligned}$$

which results in

$$D_{mn}^{\rho \lessgtr} \sin(\nu_n c_2) + O_{mn}^{\rho \lessgtr} \cos(\nu_n c_2) = 0 \quad (3.140a)$$

$$L^{(0)} c_2 + M^{(0)} = P^{(0)} \sinh(kc_2) + Q^{(0)} \cosh(kc_2) = 0. \quad (3.140b)$$

Similarly for $z = c_1$

$$D_{mn}^{\rho \lessgtr} \sin(\nu_n c_1) + O_{mn}^{\rho \lessgtr} \cos(\nu_n c_1) = 0 \quad (3.141a)$$

$$L^{(0)} c_1 + M^{(0)} = P^{(0)} \sinh(kc_1) + Q^{(0)} \cosh(kc_1) = 0. \quad (3.141b)$$

From (3.140) and (3.141)

$$\boxed{L^{(0)} = M^{(0)} = P^{(0)} = Q^{(0)}} \quad (3.142)$$

and

$$\tan(\nu_n c_2) = \tan(\nu_n c_1) \Leftrightarrow \nu_n c_2 = n\pi + \nu_n c_1 \Leftrightarrow \boxed{\nu_n = \frac{n\pi}{c_2 - c_1}}. \quad (3.143)$$

The continuity of the magnetic flux density at both axial interfaces of the tube yields

$$\begin{aligned} H_\rho^{II} \Big|_{z=c_1^+} &= H_\rho^{II} \Big|_{z=c_1^-} \Leftrightarrow \\ \sum_{n=1}^{\infty} p_n q_n (N_{mn}^{\rho \lessgtr} \cos(q_n c_1) - C_{mn}^{\rho \lessgtr} \sin(q_n c_1)) \left\{ \begin{array}{l} K'_m(p_n \rho) \\ I'_m(p_n \rho) \end{array} \right\} + k E^{(0)} K'_m(k \rho) &= \\ \sum_{n=1}^{\infty} E_{mn}^{\rho \lessgtr} p_n \cos(p_n c_1) \left\{ \begin{array}{l} K'_m(p_n \rho) \\ I'_m(p_n \rho) \end{array} \right\} + R^{(0)} (-m-1) \left\{ \begin{array}{l} \rho^{-m-1} \\ \rho^m \end{array} \right\}, \end{aligned}$$

which gives

$$q_n (N_{mn}^{\rho \lessgtr} \cos(q_n c_1) - C_{mn}^{\rho \lessgtr} \sin(q_n c_1)) = E_{mn}^{\rho \lessgtr} \cos(p_n c_1) \quad (3.144a)$$

$$E^{(0)} = R^{(0)} = 0. \quad (3.144b)$$

$$\begin{aligned} B_z^{II} \Big|_{z=c_1^+} &= B_z^{II} \Big|_{z=c_1^-} \Leftrightarrow \\ - \sum_{n=1}^{\infty} p_n^2 (N_{mn}^{\rho \lessgtr} \sin(q_n c_1) + C_{mn}^{\rho \lessgtr} \cos(q_n c_1)) \left\{ \begin{array}{l} K_m(p_n \rho) \\ I_m(p_n \rho) \end{array} \right\} - k^2 F_i(0) \left\{ \begin{array}{l} K_m(k \rho) \\ I_m(k \rho) \end{array} \right\} &= \\ - \sum_{n=1}^{\infty} E_{mn}^{\rho \lessgtr} p_n \sin(p_n c_1) \left\{ \begin{array}{l} K_m(p_n \rho) \\ I_m(p_n \rho) \end{array} \right\}, \end{aligned}$$

from which a second relation between $C_{mn}^{\rho \lessgtr}$, $N_{mn}^{\rho \lessgtr}$ and $E_{mn}^{\rho \lessgtr}$ is obtained, whereas the second zero-order term of W_a turns out to be zero

$$p_n (N_{mn}^{\rho \lessgtr} \sin(q_n c_1) + C_{mn}^{\rho \lessgtr} \cos(q_n c_1)) = E_{mn}^{\rho \lessgtr} \sin(p_n c_1) \quad (3.145a)$$

$$F^{(0)} = 0. \quad (3.145b)$$

Similarly, for $z = c_2$, the continuity of the magnetic field density gives

$$B_z^{II}|_{z=c_2^+} = B_z^{II}|_{z=c_2^-} \Leftrightarrow$$

$$\begin{aligned} -\sum_{n=1}^{\infty} p_n^2 (N_{mn}^{\rho \lessgtr} \sin(q_n c_1) + C_{mn}^{\rho \lessgtr} \cos(q_n c_1)) \begin{Bmatrix} K_m(p_n \rho) \\ I_m(p_n \rho) \end{Bmatrix} = \\ -\sum_{n=1}^{\infty} B_{mn}^{\rho \lessgtr} p_n \cos(p_n(h - c_2)) \begin{Bmatrix} K_m(p_n \rho) \\ I_m(p_n \rho) \end{Bmatrix} + D^{(0)} \begin{Bmatrix} \rho^{-m} \\ \rho^m \end{Bmatrix}, \end{aligned}$$

which implies

$$p_n (N_{mn}^{\rho \lessgtr} \sin(q_n c_2) + C_{mn}^{\rho \lessgtr} \cos(q_n c_2)) = B_{mn}^{\rho \lessgtr} \cos(p_n(h - c_2)) \quad (3.146a)$$

$$D^{(0)} = 0. \quad (3.146b)$$

If we now substitute (3.146b) in (3.139) we have

$$\boxed{C^{(0)} = 0}. \quad (3.147)$$

$$\begin{aligned} H_{\rho}^{II}|_{z=c_2^-} = H_{\rho}^{II}|_{z=c_2^+} \Leftrightarrow \\ \sum_{n=1}^{\infty} p_n q_n (N_{mn}^{\rho \lessgtr} \cos(q_n c_2) - C_{mn}^{\rho \lessgtr} \sin(q_n c_2)) \begin{Bmatrix} K'_m(p_n \rho) \\ I'_m(p_n \rho) \end{Bmatrix} = \\ \sum_{n=1}^{\infty} B_{mn}^{\rho \lessgtr} p_n \sin(p_n(h - c_2)) \begin{Bmatrix} K'_m(p_n \rho) \\ I'_m(p_n \rho) \end{Bmatrix}, \end{aligned}$$

which gives

$$q_n (N_{mn}^{\rho \lessgtr} \cos(q_n c_2) - C_{mn}^{\rho \lessgtr} \sin(q_n c_2)) = B_{mn}^{\rho \lessgtr} \sin(p_n(h - c_2)). \quad (3.148)$$

From (3.145a) and (3.144a) we obtain

$$\begin{aligned} \frac{p_n N_{mn}^{\rho \lessgtr} \sin(q_n c_1) + C_{mn}^{\rho \lessgtr} \cos(q_n c_1)}{q_n N_{mn}^{\rho \lessgtr} \cos(q_n c_1) - C_{mn}^{\rho \lessgtr} \sin(q_n c_1)} = \tan(p_n c_1) \Leftrightarrow \\ \tan(p_n c_1) = \frac{p_n N_{mn}^{\rho \lessgtr} \tan(q_n c_1) + C_{mn}^{\rho \lessgtr}}{q_n N_{mn}^{\rho \lessgtr} - C_{mn}^{\rho \lessgtr} \tan(q_n c_1)} \Leftrightarrow \\ N_{mn}^{\rho \lessgtr} q_n \tan(p_n c_1) - C_{mn}^{\rho \lessgtr} q_n \tan(p_n c_1) \tan(q_n c_1) = N_{mn}^{\rho \lessgtr} p_n \tan(q_n c_1) + C_{mn}^{\rho \lessgtr} p_i \\ N_{mn}^{\rho \lessgtr} = \frac{p_n + q_n \tan(p_n c_1) \tan(q_n c_1)}{q_n \tan(p_n c_1) - p_n \tan(q_n c_1)} C_{mn}^{\rho \lessgtr} = \alpha_i C_{mn}^{\rho \lessgtr}, \end{aligned} \quad (3.149)$$

where we define

$$\alpha_n = \frac{p_n + q_n \tan(p_n c_1) \tan(q_n c_1)}{q_n \tan(p_n c_1) - p_n \tan(q_n c_1)}. \quad (3.150)$$

Eqs. (3.145a) and (3.150) yield

$$p_n(\alpha_n \sin(q_n c_1) + \cos(q_n c_1)) C_{mn}^{\rho \lessdot} = E_{mn}^{\rho \lessdot} \sin(p_n c_1) \Leftrightarrow E_{mn}^{\rho \lessdot} = \beta_n C_{mn}^{\rho \lessdot},$$

where β_n is set

$$\beta_n = p_n \frac{\alpha_n \sin(q_n c_1) + \cos(q_n c_1)}{\sin(p_n c_1)}. \quad (3.151)$$

In the same way (3.146a) and (3.150) give

$$p_n(\alpha_n \sin(q_n c_2) + \cos(q_n c_2)) C_{mn}^{\rho \lessdot} = B_{mn}^{\rho \lessdot} \cos(p_n(h - c_2)) \Leftrightarrow B_{mn}^{\rho \lessdot} = \gamma_n C_{mn}^{\rho \lessdot},$$

where

$$\gamma_n = p_n \frac{\alpha_n \sin(q_n c_2) + \cos(q_n c_2)}{\cos(p_n(h - c_2))} \quad (3.152)$$

and from (3.141a) it is obtained

$$O_{mn}^{\rho \lessdot} = -\tan(\nu_n c_1) D_{mn}^{\rho \lessdot} = \delta_n D_{mn}^{\rho \lessdot}$$

where it is again defined

$$\delta_n = -\tan(\nu_n c_1). \quad (3.153)$$

Furthermore, from (3.146a) and (3.148) we obtain:

$$\begin{aligned} \frac{q_n N_{mn}^{\rho \lessdot} \cos(q_n c_2) - C_{mn}^{\rho \lessdot} \sin(q_n c_2)}{p_n N_{mn}^{\rho \lessdot} \sin(q_n c_2) + C_{mn}^{\rho \lessdot} \cos(q_n c_2)} &= \tan(p_n(h - c_2)) \Leftrightarrow \\ \tan(p_n(h - c_2)) &= \frac{q_n N_{mn}^{\rho \lessdot} - C_{mn}^{\rho \lessdot} \tan(q_n c_2)}{p_n N_{mn}^{\rho \lessdot} \tan(q_n c_2) + C_{mn}^{\rho \lessdot}} \Leftrightarrow \\ N_{mn}^{\rho \lessdot} p_n \tan(p_n(h - c_2)) \tan(q_n c_2) + C_{mn}^{\rho \lessdot} p_n \tan(p_n(h - c_2)) &= N_{mn}^{\rho \lessdot} q_n - C_{mn}^{\rho \lessdot} q_n \tan(q_n c_2) \\ N_{mn}^{\rho \lessdot} &= \frac{p_n \tan(p_n(h - c_2)) + q_n \tan(q_n c_2)}{q_n - p_n \tan(p_n(h - c_2)) \tan(q_n c_2)} C_{mn}^{\rho \lessdot}. \end{aligned} \quad (3.154)$$

Combining (3.149) and (3.154)

$$\frac{q_n \tan(p_n c_1) - p_n \tan(q_n c_1)}{q_n - p_n \tan(p_n(h - c_2)) \tan(q_n c_2)} = \frac{p_n + q_n \tan(p_n c_1) \tan(q_n c_1)}{p_n \tan(p_n(h - c_2)) + q_n \tan(q_n c_2)}. \quad (3.155)$$

The transcendental equation (6.46) is again solved using the method proposed in [DL67] and [Lyn67]. It is worth to mention that this equation is the general transcendental equation for a planar conductor of arbitrary thickness, when PEC and PMC conditions are applied at $z = 0$ and $z = h$, respectively. It is also noted that the relation for the semi-infinite plate (6.9) is a special case of the general transcendental equation (6.46), when $c_1 = 0$ is set.

Continuity at the radial interfaces

Matching the field at the radial interfaces $\rho = b_1$ and $\rho = b_2$ we obtain

$$\begin{aligned}
H_\rho^I|_{\rho=b_1} &= H_\rho^{II}|_{\rho=b_1} \Leftrightarrow \\
\sum_{n=1}^{\infty} A_{mn}^{\rho<} w_n \cos(w_n z) I'_m(w_n b) &= u(z - c_2) \sum_{n=1}^{\infty} B_{mn}^{\rho\leqslant} p_n \sin(p_n(h - z)) \left\{ \begin{array}{l} K'_m(p_n b_1) \\ I'_m(p_n b_1) \end{array} \right\} \\
+ [u(z - c_1) - u(z - c_2)] \sum_{n=1}^{\infty} (N_{mn}^{\rho\leqslant} \cos(q_n z) - C_{mn}^{\rho\leqslant} \sin(q_n z)) p_n q_n &\left\{ \begin{array}{l} K'_m(p_n b_1) \\ I'_m(p_n b_1) \end{array} \right\} \\
+ [u(z - c_1) - u(z - c_2)] \sum_{n=1}^{\infty} \frac{k^2 j m}{b_1} (D_{mn}^{\rho\leqslant} \sin(\nu_n z) + O_{mn}^{\rho\leqslant} \cos(\nu_n z)) \left\{ \begin{array}{l} K'_m(\xi_n b_1) \\ I'_m(\xi_n b_1) \end{array} \right\} \\
+ [u(z) - u(z - c_1)] \sum_{n=1}^{\infty} E_{mn}^{\rho\leqslant} \cos(p_n z) &\left\{ \begin{array}{l} K'_m(p_n b_1) \\ I'_m(p_n b_1) \end{array} \right\} \\
+ \sigma_m(b_1, z) &
\end{aligned} \tag{3.156}$$

$$\begin{aligned}
H_\varphi^I|_{\rho=b_1} &= H_\varphi^{II}|_{\rho=b_1} \Leftrightarrow \\
\sum_{n=1}^{\infty} A_{mn}^{\rho<} \frac{j m}{b} \cos(w_n z) I_m(w_n b) &= u(z - c_2) \sum_{n=1}^{\infty} B_{mn}^{\rho\leqslant} \frac{j m}{b} \sin(p_n(h - z)) \left\{ \begin{array}{l} K_m(p_n b_1) \\ I_m(p_n b_1) \end{array} \right\} \\
[u(z - c_1) - u(z - c_2)] \sum_{n=1}^{\infty} \frac{j m}{b} (N_{mn}^{\rho\leqslant} \cos(q_n z) - C_{mn}^{\rho\leqslant} \sin(q_n z)) q_n &\left\{ \begin{array}{l} K_m(p_n b_1) \\ I_m(p_n b_1) \end{array} \right\} \\
- [u(z - c_1) - u(z - c_2)] \sum_{n=1}^{\infty} k^2 (D_{mn}^{\rho\leqslant} \sin(\nu_n z) + O_{mn}^{\rho\leqslant} \cos(\nu_n z)) \xi &\left\{ \begin{array}{l} K'_m(\xi_n b_1) \\ I'_m(\xi_n b_1) \end{array} \right\} \\
+ [u(z) - u(z - c_1)] \sum_{n=1}^{\infty} \frac{j m}{b} E_{mn}^{\rho\leqslant} \cos(p_n z) &\left\{ \begin{array}{l} K_m(p_n b_1) \\ I_m(p_n b_1) \end{array} \right\} \\
+ J_z(b_1, z) &
\end{aligned} \tag{3.157}$$

$$\begin{aligned}
B_z^I|_{\rho=b_1} &= B_z^{II}|_{\rho=b_1} \Leftrightarrow \\
- \sum_{n=1}^{\infty} A_{mn}^{\rho<} w_n \sin(w_n z) I_m(w_n b) &= - u(z - c_2) \sum_{n=1}^{\infty} B_{mn}^{\rho\leqslant} \cos(p_n(h - z)) p_n \left\{ \begin{array}{l} K'_m(p_n b_1) \\ I'_m(p_n b_1) \end{array} \right\} \\
- [u(z - c_1) - u(z - c_2)] \sum_{n=1}^{\infty} (N_{mn}^{\rho\leqslant} \sin(q_n z) + C_{mn}^{\rho\leqslant} \cos(q_n z)) p_n^2 &\left\{ \begin{array}{l} K'_m(p_n b_1) \\ I'_m(p_n b_1) \end{array} \right\} \\
+ [u(z) - u(z - c_1)] \sum_{n=1}^{\infty} E_{mn}^{\rho\leqslant} \sin(p_n z) p_n &\left\{ \begin{array}{l} K'_m(p_n b_1) \\ I'_m(p_n b_1) \end{array} \right\} \\
+ J_\varphi(b_1, z), &
\end{aligned} \tag{3.158}$$

The notation $\sigma_m(b_1, z)$, $J_z(b_1, z)$ and $J_\varphi(b_1, z)$ is used for the B_ρ , B_ϕ and B_z components of the source field, respectively, at $\rho = b_1$, the expressions of which are given in Appendix ???. Generally, the equivalent magnetic charge corresponding to a discontinuity of the magnetic flux density is expressed as $\sigma_m = \Delta\mathbf{B} \cdot \mathbf{n}$, where $\Delta\mathbf{B}$ is the discontinuity magnetic flux density and \mathbf{n} the unit normal vector. Furthermore, the electric current sources produced by the discontinuity of the magnetic field are expressed as $\mathbf{J} = \mathbf{n} \times \Delta\mathbf{H}$, with $\Delta\mathbf{H}$ being the discontinuity of the magnetic field. Hence, the terms $\sigma_m(z)$, $J_z(z)$ and $J_\varphi(z)$ in (3.156), (3.157) and (3.158) can be viewed as equivalent magnetic charge and electric current sources produced by the discontinuity of φ and W_a at the interfaces $z = c_1$ and $z = c_2$.

Finally, if we weight (3.156) and (3.157) with $\cos(w_l z)$ and (3.158) with $\sin(w_l z)$, taking into account (3.150) - (3.153) and knowing that

$$\int_0^h \sin(u_l z) \sin(u_i z) dz = \int_0^h \cos(u_l z) \cos(u_i z) dz = \delta_{l,n} \frac{h}{2} \quad (3.159)$$

the system (3.156)-(3.158) transforms into

$$\begin{aligned} w_n I'_m(w_n b) A_{mn}^{\rho^<} &= -M_c(l, i) p_n \begin{Bmatrix} K'_m(p_n b_1) \\ I'_m(p_n b_1) \end{Bmatrix} C_{mn}^{\rho \leqslant} + \frac{k^2 j m}{b} M_r(l, i) \begin{Bmatrix} K_m(\xi_n b_1) \\ I_m(\xi_n b_1) \end{Bmatrix} D_{mn}^{\rho \leqslant} \\ &\quad + S_\rho(z) \end{aligned} \quad (3.160)$$

$$\begin{aligned} \frac{jm}{b} I_m(w_n b) A_{mn}^{\rho^<} &= -\frac{jm}{b} M_c(l, i) \begin{Bmatrix} K_m(p_n b_1) \\ I_m(p_n b_1) \end{Bmatrix} C_{mn}^{\rho \leqslant} - k^2 M_r(l, i) \xi_n \begin{Bmatrix} K'_m(\xi_n b_1) \\ I'_m(\xi_n b_1) \end{Bmatrix} D_{mn}^{\rho \leqslant} \\ &\quad + S_\varphi(b_1, z) \end{aligned} \quad (3.161)$$

$$-w_n I_m(w_n b) A_{mn}^{\rho^<} = -M_s(l, i) p_n \begin{Bmatrix} K_m(p_n b_1) \\ I_m(p_n b_1) \end{Bmatrix} C_{mn}^{\rho \leqslant} + S_z(b_1, z), \quad (3.162)$$

with

$$\begin{aligned} M_c(l, i) &= \frac{2}{h} \left[-\beta_n \int_0^{c_1} \cos(p_n z) \cos(w_l z) dz - q_n \alpha_n \int_{c_1}^{c_2} \cos(q_n z) \cos(w_l z) dz \right. \\ &\quad \left. + q_n \int_{c_1}^{c_2} \sin(q_n z) \cos(w_l z) dz - \gamma_n \int_{c_2}^h \sin(p_n(h-z)) \cos(w_l z) dz \right] \end{aligned} \quad (3.163)$$

$$\begin{aligned} M_s(l, i) &= \frac{2}{h} \left[\beta_n \int_0^{c_1} \sin(p_n z) \sin(w_l z) dz + p_n \alpha_n \int_{c_1}^{c_2} \sin(q_n z) \sin(w_l z) dz \right. \\ &\quad \left. + p_n \int_{c_1}^{c_2} \cos(q_n z) \sin(w_l z) dz + \gamma_n \int_{c_2}^h \cos(p_n(h-z)) \sin(w_l z) dz \right] \end{aligned} \quad (3.164)$$

and

$$M_r(l, i) = \frac{2}{h} \left[\int_{c_1}^{c_2} \sin(\nu_n z) \cos(w_l z) dz + \delta_n \int_{c_1}^{c_2} \cos(\nu_n z) \cos(w_l z) dz \right] \quad (3.165)$$

and the source terms

$$\begin{aligned} S_\rho(\rho, z) = & \frac{2}{h} [R_c^{(iv)}(-\kappa_n, w_l) P_{mn} - R_c^{(iii)}(-v_n, w_l) v_n A_{mn} + R_c^{(iii)}(v_n, w_l) v_n B_{mn} \\ & - R_c^{(ii)}(-v_n, w_l) v_n E_{mn} + R_c^{(ii)}(v_n, w_l) v_n F_{mn} + R_c^{(i)}(\kappa_n, w_l) N_{mn}] \kappa_n J'_m(\kappa_n \rho) \\ & + \frac{2k^2 jm}{\rho h} [R_c^{(iii)}(-r_n, w_l) C_{mn} + R_c^{(iii)}(r_n, w_l) D_{mn} \\ & + R_c^{(ii)}(-r_n, w_l) L_{mn} + R_c^{(ii)}(r_n, w_l) M_{mn}] J_m(s_n \rho) \end{aligned} \quad (3.166)$$

$$\begin{aligned} S_\varphi(\rho, z) = & \frac{2jm}{\rho h} [R_c^{(iv)}(-\kappa_n, w_l) P_{mn} - R_c^{(iii)}(-v_n, w_l) v_n A_{mn} + R_c^{(iii)}(v_n, w_l) v_n B_{mn} \\ & - R_c^{(ii)}(-v_n, w_l) v_n E_{mn} + R_c^{(ii)}(v_n, w_l) v_n F_{mn} + R_c^{(i)}(\kappa_n, w_l) N_{mn}] J_m(\kappa_n \rho) \\ & - \frac{2k^2}{h} [R_c^{(iii)}(-r_n, w_l) C_{mn} + R_c^{(iii)}(r_n, w_l) D_{mn} + R_c^{(ii)}(-r_n, w_l) L_{mn} \\ & + R_c^{(ii)}(r_n, w_l) M_{mn}] J'_m(s_n \rho) \end{aligned} \quad (3.167)$$

$$\begin{aligned} S_z(\rho, z) = & \frac{2}{h} [-R_s^{(iv)}(-\kappa_n, w_l) P_{mn} + R_s^{(iii)}(-v_n, w_l) \kappa_n A_{mn} + R_s^{(iii)}(v_n, w_l) \kappa_n B_{mn} \\ & + R_s^{(ii)}(-v_n, w_l) \kappa_n E_{mn} + R_s^{(ii)}(v_n, w_l) \kappa_n F_{mn} + R_s^{(iv)}(\kappa_n, w_l) N_{mn}] \kappa_n J_m(\kappa_n \rho), \end{aligned} \quad (3.168)$$

where

$$R_s^{(i, ii, iii, iv)}(\mu, \nu) = \int_{0, c_1, z', c_2}^{c_1, z', c_2, h} e^{\mu(z-z')} \sin(\nu z) dz \quad (3.169)$$

and

$$R_c^{(i, ii, iii, iv)}(\mu, \nu) = \int_{0, c_1, z', c_2}^{c_1, z', c_2, h} e^{\mu(z-z')} \cos(\nu z) dz. \quad (3.170)$$

Repeating the same analysis for the external radial interface of the tube ($\rho = b_2$) we obtain analogous relations

$$\begin{aligned} w_n I'_m(w_n b) M_{mn}^{\rho >} = & -M_c(l, i) p_n \left\{ \begin{array}{l} K'_m(p_n b_2) \\ I'_m(p_n b_2) \end{array} \right\} C_{mn}^{\rho \leqslant} + \frac{k^2 jm}{b} M_r(l, i) \left\{ \begin{array}{l} K_m(\xi_n b_2) \\ I_m(\xi_n b_2) \end{array} \right\} D_{mn}^{\rho \leqslant} \\ & + S_\rho(b_2, z) \end{aligned} \quad (3.171)$$

$$\begin{aligned} \frac{jm}{b} I_m(w_n b) M_{mn}^{\rho>} = & -\frac{jm}{b} M_c(l, i) \begin{Bmatrix} K_m(p_n b_2) \\ I_m(p_n b_2) \end{Bmatrix} C_{mn}^{\rho \leqslant} - k^2 M_r(l, i) \xi_n \begin{Bmatrix} K'_m(\xi_n b_2) \\ I'_m(\xi_n b_2) \end{Bmatrix} D_{mn}^{\rho \leqslant} \\ & + S_\varphi(b_2, z) \end{aligned} \quad (3.172)$$

and

$$-w_n I_m(w_n b) M_{mn}^{\rho>} = -M_s(l, i) p_n \begin{Bmatrix} K_m(p_n b_2) \\ I_m(p_n b_2) \end{Bmatrix} C_{mn}^{\rho \leqslant} + S_z(b_2, z), \quad (3.173)$$

The relations (6.50)-(6.52) complete the system of equations which determine the expansion coefficients $A_{mn}^{\rho<}$, $M_{mn}^{\rho>}$, $C_{mn}^{\rho<}$, $C_{mn}^{\rho>}$, $D_{mn}^{\rho<}$ and $D_{mn}^{\rho>}$.

Therefore, the coefficients are sought by solving the system of the boundary conditions in matrix notation

$$\mathbf{w} \mathbf{I}'_{\mathbf{w},1} \mathbf{A}^{\rho<} = -\mathbf{M}_c \mathbf{p} \begin{Bmatrix} \mathbf{K}'_{\mathbf{p},1} \\ \mathbf{I}'_{\mathbf{p},1} \end{Bmatrix} \mathbf{C}^{\rho \leqslant} + \frac{k^2 jm}{b_1} \mathbf{M}_r \begin{Bmatrix} \mathbf{K}_{\boldsymbol{\xi},1} \\ \mathbf{I}_{\boldsymbol{\xi},1} \end{Bmatrix} \mathbf{D}^{\rho \leqslant} + \mathbf{S}_\rho \quad (3.174)$$

$$\frac{jm}{b_1} \mathbf{I}'_{\mathbf{w},1} \mathbf{A}^{\rho<} = -\frac{jm}{b_1} \mathbf{M}_c \begin{Bmatrix} \mathbf{K}_{\mathbf{p},1} \\ \mathbf{I}_{\mathbf{p},1} \end{Bmatrix} \mathbf{C}^{\rho \leqslant} - k^2 \boldsymbol{\xi} \mathbf{M}_r \begin{Bmatrix} \mathbf{K}'_{\boldsymbol{\xi},1} \\ \mathbf{I}'_{\boldsymbol{\xi},1} \end{Bmatrix} \mathbf{D}^{\rho \leqslant} + \mathbf{S}_\varphi \quad (3.175)$$

$$-\mathbf{w} \mathbf{I}'_{\mathbf{w},1} \mathbf{A}^{\rho<} = -\mathbf{M}_s \mathbf{p} \begin{Bmatrix} \mathbf{K}_{\mathbf{p},1} \\ \mathbf{I}_{\mathbf{p},1} \end{Bmatrix} \mathbf{C}^{\rho \leqslant} + \mathbf{S}_z \quad (3.176)$$

$$\mathbf{w} \mathbf{K}'_{\mathbf{w},2} \mathbf{M}^{\rho>} = -\mathbf{M}_c \mathbf{p} \begin{Bmatrix} \mathbf{K}'_{\mathbf{p},2} \\ \mathbf{I}'_{\mathbf{p},2} \end{Bmatrix} \mathbf{C}^{\rho \leqslant} + \frac{k^2 jm}{b_2} \mathbf{M}_r \begin{Bmatrix} \mathbf{K}_{\boldsymbol{\xi},2} \\ \mathbf{I}_{\boldsymbol{\xi},2} \end{Bmatrix} \mathbf{D}^{\rho \leqslant} + \mathbf{S}_\rho \quad (3.177)$$

$$\frac{jm}{b_2} \mathbf{K}'_{\mathbf{w},2} \mathbf{M}^{\rho>} = \frac{jm}{b_2} \mathbf{M}_c \begin{Bmatrix} \mathbf{K}_{\mathbf{p},2} \\ \mathbf{I}_{\mathbf{p},2} \end{Bmatrix} \mathbf{C}^{\rho \leqslant} - k^2 \boldsymbol{\xi} \mathbf{M}_r \begin{Bmatrix} \mathbf{K}'_{\boldsymbol{\xi},2} \\ \mathbf{I}'_{\boldsymbol{\xi},2} \end{Bmatrix} \mathbf{D}^{\rho \leqslant} + \mathbf{S}_\varphi \quad (3.178)$$

$$-\mathbf{w} \mathbf{K}'_{\mathbf{w},2} \mathbf{M}^{\rho>} = -\mathbf{M}_s \mathbf{p} \begin{Bmatrix} \mathbf{K}_{\mathbf{p},2} \\ \mathbf{I}_{\mathbf{p},2} \end{Bmatrix} \mathbf{C}^{\rho \leqslant} + \mathbf{S}_z. \quad (3.179)$$

Here, $\mathbf{A}^{\rho<}$, $\mathbf{C}^{\rho<}$, $\mathbf{C}^{\rho>}$, $\mathbf{D}^{\rho<}$, $\mathbf{D}^{\rho>}$ and $\mathbf{M}^{\rho>}$ are column vectors of expansion coefficients, \mathbf{w} , \mathbf{p} and $\boldsymbol{\xi}$ are diagonal matrices of the eigenvalues, and \mathbf{M}_c , \mathbf{M}_s and \mathbf{M}_r are the matrices (6.53)-(6.55) and

$$\mathbf{I}_{\mathbf{x},i} = \text{diag}[I_m(x_n b_i)] \quad (3.180)$$

$$\mathbf{K}_{\mathbf{x},i} = \text{diag}[K_m(x_n b_i)]. \quad (3.181)$$

3.3.3 Numerical treatment

For the Green's function derivation the choice of the number of azimuthal modes (N_m), radial/axial modes (N_p, N_κ) as well as the truncation boundaries h and ρ_L is of great importance with regards to accuracy and numerical stability. It has been observed that the lower the operation frequency is, the larger is the distance, where the domain should

be truncated (larger h and ρ_L). As far as the number of radial/axial modes is concerned, there is a lower threshold defined by the desired accuracy and a higher threshold, over which the system condition number becomes too high. Both the lower and the higher thresholds are also linked with the truncation boundaries. The larger the truncation distance is, the larger are the values of these thresholds. In addition, as in the case of the induction problem, the ratios of s , κ and ξ, p eigenvalues need to be approximately $N_s/N_\kappa = N_\xi/N_p \approx (c_2 - c_1)/h$, in order to keep the system condition number low [ST12] and avoid a close-to-singular system.

An algorithm optimising the parameters choice has not been developed in this work and a thorough study on this issue, taking the entire configuration parameters into account, should be carried out as a perspective of the model optimisation.

3.4 Eddy-current signal calculation

The last task in order to solve the NDT modeling problem is the calculation of the eddy-current signal. As defined in Section 3.1, the eddy-current signal is the impedance change owing to the presence of the inspected work-piece with regards to the free-space coil impedance. The coil impedance can be written as

$$Z = Z_0 + \Delta Z_{geom} + \Delta Z_{crack}. \quad (3.182)$$

In (6.61) Z_0 stands for the free-space coil impedance and it depends on the characteristics of the coil and the frequency. The term ΔZ_{geom} is the impedance change due to the presence of the flawless piece and finally, ΔZ_{crack} represents the impedance variation owing to the inhomogeneity introduced by the crack.

The expression of Z_0 reads

$$Z_0 = j\omega L, \quad (3.183)$$

where L is the free-space inductance of the coil. The above equation shows that Z_0 is purely inductive and its analytical expression can be found in [TK06]. The variation ΔZ_{geom} has been calculated in Section 3.2 for a coil inspecting the hole from inside of our geometries or in [ST15] when the coil is moved above the work-piece. In this section, we are interested in calculating the term ΔZ_{crack} .

In order to calculate this term one needs to solve at first the integral equation associated to our problem, which reads

$$\mathbf{n} \cdot \mathbf{E}_0(\mathbf{r}) = -j\omega\mu_0 \int_{S_{def}} \mathbf{n} \cdot \overline{\mathbf{G}}(\mathbf{r}, \mathbf{r}') \cdot \mathbf{n} p(\mathbf{r}') dS' \quad (3.184)$$

where \mathbf{E}_0 is the field in the absence of the flaw, namely the primary field, calculated in Section 3.2, $\overline{\mathbf{G}}(\mathbf{r}, \mathbf{r}')$ is the Green's dyadic operator, and \mathbf{n} stands for the normal to the

crack surface unit vector. It is recalled here that we consider a narrow crack, which is represented by a surface dipole density $p(\mathbf{r})$, whereas S_{def} is the surface of the crack. The effect of the borehole is taken implicitly into account by the Green's dyad, the construction of which is presented in the previous section.

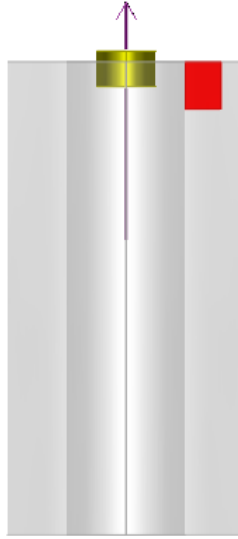
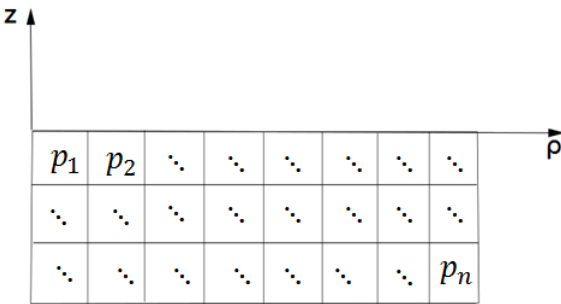


Figure 3.9: Inspection of a conductor with a borehole and a crack breaking the wall of the borehole. The flaw surface is on the $\rho - z$ plane with a narrow azimuthal opening.

As for the crack orientation, the normal vector \mathbf{n} is parallel to the φ direction (Fig. 3.9). Thus, the only component of the Green's tensor needed is the Green's function $G^{\varphi\varphi}$, which is calculated in Section 3.3. Taking into account (2.36), (6.4), (6.5), (6.40), (6.41), the expressions of the expansion coefficients (6.28)-(6.36) and having calculated the expansion coefficients $C_{mn}^{\rho \leq}$ and $D_{mn}^{\rho \leq}$ from the solution of the system (3.174)-(3.179), the analytical expression of the Green's function reads as

$$\begin{aligned}
 G^{\varphi\varphi}(\mathbf{r}, \mathbf{r}') = & j\omega \sum_{m=-\infty}^{m=\infty} \sum_{n=1}^{\infty} \kappa_n \left(A_{mn} e^{-v_n(z-z')} + B_{mn} e^{v_n(z-z')} \right) J'_m(\kappa_n \rho) e^{jm\varphi} \\
 & + j\omega \sum_{m=-\infty}^{m=\infty} \sum_{n=1}^{\infty} \frac{jm}{\rho} \left(D_{mn} e^{r_n(z-z')} - C_{mn} e^{-r_n(z-z')} \right) J_m(s_n \rho) e^{jm\varphi} \\
 & + j\omega \sum_{m=-\infty}^{m=\infty} \sum_{n=1}^{\infty} C_{mn}^{\rho \leq} p_n \cos(q_n z) \left\{ \begin{array}{l} K'_m(p_n \rho) \\ I'_m(p_n \rho) \end{array} \right\} e^{jm\varphi} \\
 & + j\omega \sum_{m=-\infty}^{m=\infty} \sum_{n=1}^{\infty} D_{mn}^{\rho \leq} \xi_n \cos(\nu_n z) \left\{ \begin{array}{l} K'_m(\xi_n \rho) \\ I'_m(\xi_n \rho) \end{array} \right\} e^{jm\varphi}; \quad z \leq z' \tag{3.185}
 \end{aligned}$$

$$\begin{aligned}
G^{\varphi\varphi}(\mathbf{r}, \mathbf{r}') = & j\omega \sum_{m=-\infty}^{m=\infty} \sum_{n=1}^{\infty} \kappa_n \left(E_{mn} e^{-v_n(z-z')} + F_{mn} e^{v_n(z-z')} \right) J'_m(\kappa_n \rho) e^{jm\varphi} \\
& + j\omega \sum_{m=-\infty}^{m=\infty} \sum_{n=1}^{\infty} \frac{jm}{\rho} \left(M_{mn} e^{r_n(z-z')} - L_{mn} e^{-r_n(z-z')} \right) J_m(s_n \rho) e^{jm\varphi} \\
& + j\omega \sum_{m=-\infty}^{m=\infty} \sum_{n=1}^{\infty} C_{mn}^{\rho \leqslant} p_n \cos(q_n z) \begin{Bmatrix} K'_m(p_n \rho) \\ I'_m(p_n \rho) \end{Bmatrix} e^{jm\varphi} \\
& + j\omega \sum_{m=-\infty}^{m=\infty} \sum_{n=1}^{\infty} D_{mn}^{\rho \leqslant} \xi_n \cos(\nu_n z) \begin{Bmatrix} K'_m(\xi_n \rho) \\ I'_m(\xi_n \rho) \end{Bmatrix} e^{jm\varphi}; \quad z < z' \tag{3.186}
\end{aligned}$$

Figure 3.10: Crack discretisation in n cells.

Eq. (6.62) is solved numerically by means of the method of moments (MoM) [Che95]. The unknown distribution is discretized in n (Fig. 3.10) cells using a set of rectangular pulse basis-functions, while a set of Dirac delta functions assigned at the barycenters of the basis-functions supports are used as test functions (point-matching method). Hence, the electric dipole distribution of every cell derives from the solution of

$$\mathbf{n} \cdot \begin{bmatrix} \mathbf{E}_0(\mathbf{r}_1) \\ \mathbf{E}_0(\mathbf{r}_2) \\ \vdots \\ \mathbf{E}_0(\mathbf{r}_n) \end{bmatrix} = \begin{bmatrix} a_{1,1} & a_{1,2} & \cdots & a_{1,n} \\ a_{2,1} & a_{2,2} & \cdots & a_{2,n} \\ \vdots & \vdots & \ddots & \vdots \\ a_{n,1} & a_{n,2} & \cdots & a_{n,n} \end{bmatrix} \begin{bmatrix} p_1 \\ p_2 \\ \vdots \\ p_n \end{bmatrix}, \tag{3.187}$$

where $a_{i,j} = \int_{S_j} \mathbf{n} \cdot \overline{\mathbf{G}}(\mathbf{r}_i, \mathbf{r}') \cdot \mathbf{n} d\mathbf{r}'$, p_j is the uniform electric dipole distribution in the j -th cell and S_j is the cell surface. It is noted that, despite the fact that we represent the crack as a surface distribution of electric dipoles, a narrow opening (d) of it is considered for the simulations. Thus, an azimuthal angle $\delta\varphi$ is taken into account for each cell and the Green's function (3.186) and (3.185) is subjected to an azimuthal integration. However, by considering a constant azimuthal angle for every cell a conical crack is considered since the crack opening becomes larger for larger ρ (Fig. 3.11). In order to take this effect into account and simulate a crack of constant opening we need to correct the azimuthal dimension of the j -cell $\delta\varphi_j$ according to its ρ'_j position. Considering that the opening is

very small

$$\tan(\delta\varphi_j) \simeq \delta\varphi_j = \frac{d_j}{2\rho'_j} \quad (3.188)$$

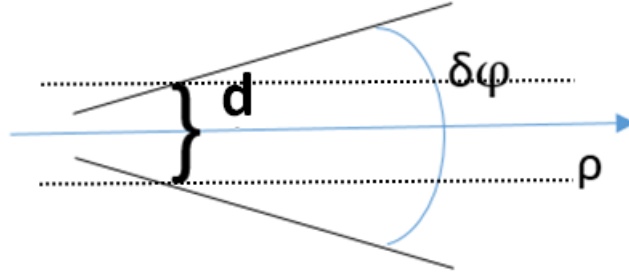


Figure 3.11: Conical crack representation.

Hence, if we consider constant crack opening $d_j = d$ then the azimuthal angular opening of each cell should be calculated by $\delta\varphi_j = \frac{d}{2\rho'_j}$.

However, attention has to be paid while computing the diagonal elements $a_{i,i}$ of (3.187). These elements include, except for the field reflected by the interfaces of the work-piece, the field radiated by the electric dipole. This part of the elements is singular when calculated at the location point ($\mathbf{r} = \mathbf{r}'$) or at its vicinity and it has to be "isolated" and treated separately while deriving the Green's function. The treatment to which this part is subjected is like the one in [BTP12].

Solution of (3.187) gives the surface dipole density in every element and thus, the dipole distribution that represents the entire defect. Once the dipole distribution obtained, the reciprocity theorem is applied to derive the ECT signal of the crack. The eddy-current probe impedance change due to a narrow crack is given by the formula [Bow94]

$$I^2 \Delta Z_{crack} = - \int_{S_{def}} \mathbf{E}_0(\mathbf{r}) \cdot \mathbf{p}(\mathbf{r}) dS \quad (3.189)$$

where I is the amplitude of the coil current.

Chapter 4

Numerical validations

In this chapter we will present results that validate the models presented in Chapter 3. Two different geometries are treated: a conducting plate with a borehole and a conducting tube. Each of these geometries corresponds to a different application. The former is orientated to applications in aeronautics, more precisely to aircraft fasteners inspection, whereas the latter simulates the inspection of steam generator tubes in nuclear plants. The models are validated by comparing their results with simulations from other models, i.e. the VIM-SIM method using the CIVA software and the FEM model using the software COMSOL, as well as with experimental data. All simulations have been performed on a workstation with an Intel Core i7 @ 2.93 GHz processor and 8 GB RAM. Finally, the computational times given refer to the entire scan of the coil, unless it is explicitly mentioned that it refers to one coil position (which is the case for the FEM computational times).

4.1 Conducting plate with a borehole

A conducting plate with a borehole is considered, referring to Fig. 6.1 and the models developed in Chapter 3, as a conducting tube, the radial thickness of which is sufficiently large versus the penetration depth, so that there is no reflection of the field from its outer interface. We will treat in this section two distinct cases. First, we present results of a thick plate, the thickness of which is large enough to approximate a half-space. Second, we present the results of a thinner plate where the field reflection from the lower interface is not negligible.

For both cases a coil scanning from above the work-piece is considered. In this case, the primary field and the coil impedance change due to the flawless piece have been calculated in previous works [ST15] and will be considered as validated.

4.1.1 Halfspace with a borehole and a crack

The goal of this subsection is, on the one hand, to demonstrate the validity of the developed model and, on the other hand, to give a quantitative interpretation of the eddy-current signals. Therefore, we consider a half-space with a borehole and a narrow crack breaking the wall of the borehole (Fig. 6.6), whereas a coil excited at 1 kHz scans the work-piece from above. Table 6.1 summarises the simulation parameters.

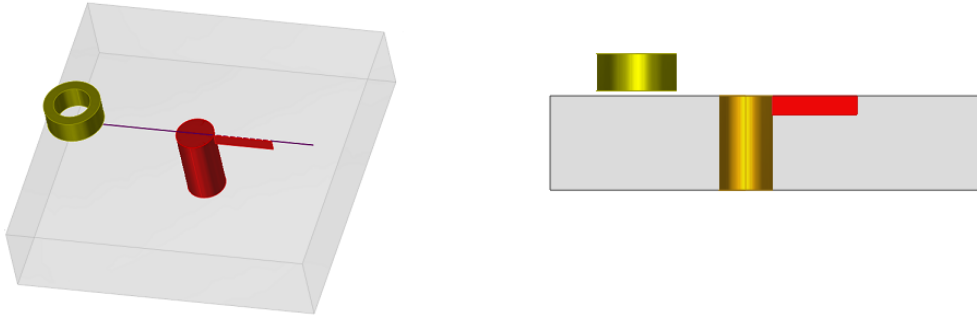


Figure 4.1: Half-space with borehole and a crack.

Table 4.1: Simulation parameters for a conducting half-space with a borehole and a thin crack

	Coil	Halfspace		Crack	
Inner diameter	6 mm	Conductivity	10 MS/m	Length	9.8 mm
Outer diameter	9.3 mm	Hole diameter	6.25 mm	Depth	2 mm
Length	4 mm			Opening	0.1 mm
Turns	336				
Lift-off	0.5 mm				

Fig. 4.2 shows the real (left) and the imaginary part (right) of the coil impedance variation for the different positions of the coil. The impedance change is given with respect to the value above an infinite plate with the properties given in Table 6.1. As it can be seen in Fig. 6.6 in the absence of a crack the work-piece is rotationally symmetric. This symmetry is reflected in the eddy-current signal. As demonstrated by the signals of Fig. 4.2 the signal is symmetric with respect to the borehole axis of radial symmetry.

Moreover, Fig. 4.3 illustrates the signal due to the crack in the presence of the borehole. In other words, the signal represents the impedance change owing to a crack in the conducting plate taking into account the interaction of the borehole and the defect. The presence of the crack in Fig. 6.6 introduces a geometrical asymmetry in the work-piece which is expected to be reflected into the eddy-current signal as well. The total eddy-current signal is the superposition of the signals of Fig. 4.2 and Fig. 4.3 and it is illustrated in Fig. 6.7. The impedance variation with respect to the value above an infinite plate for different coil positions is illustrated. One can see that the presence of the flaw introduces, indeed, an asymmetry to the eddy-current signal.

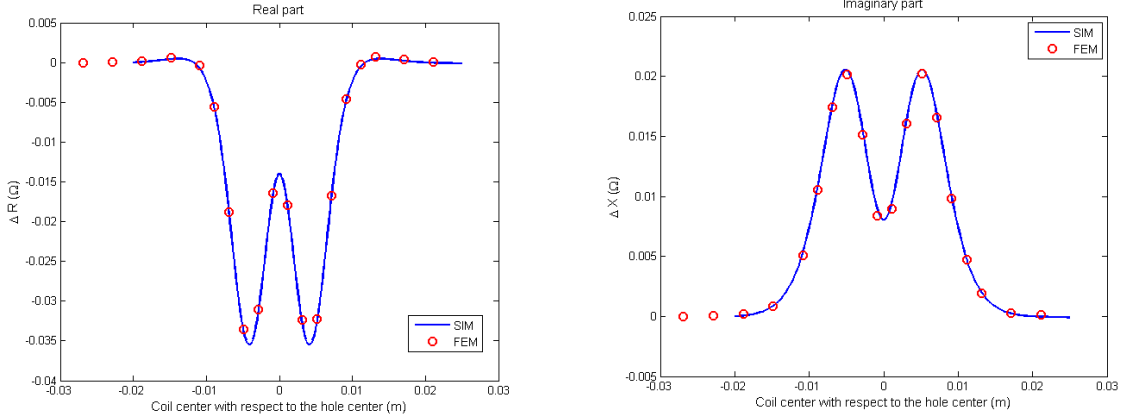


Figure 4.2: Impedance variation vs. coil position along a scan over the flawless work-piece.

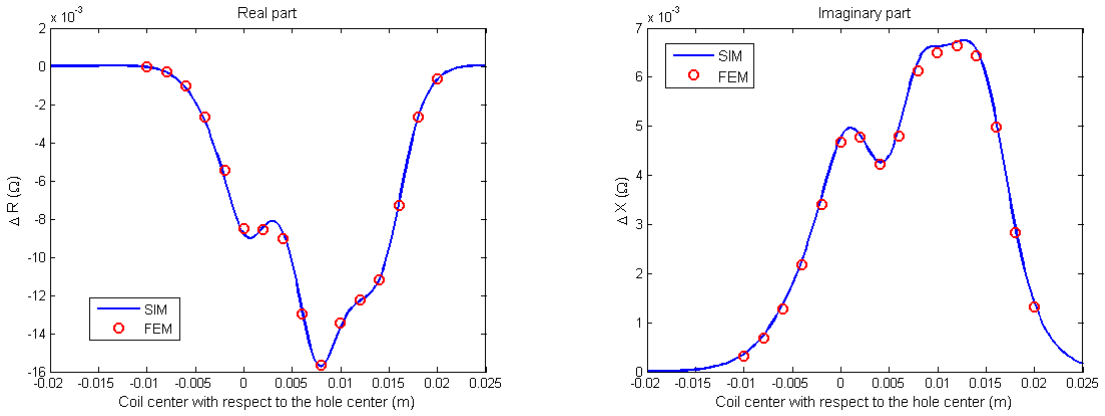


Figure 4.3: Impedance variation owing to the crack in the presence of the borehole.

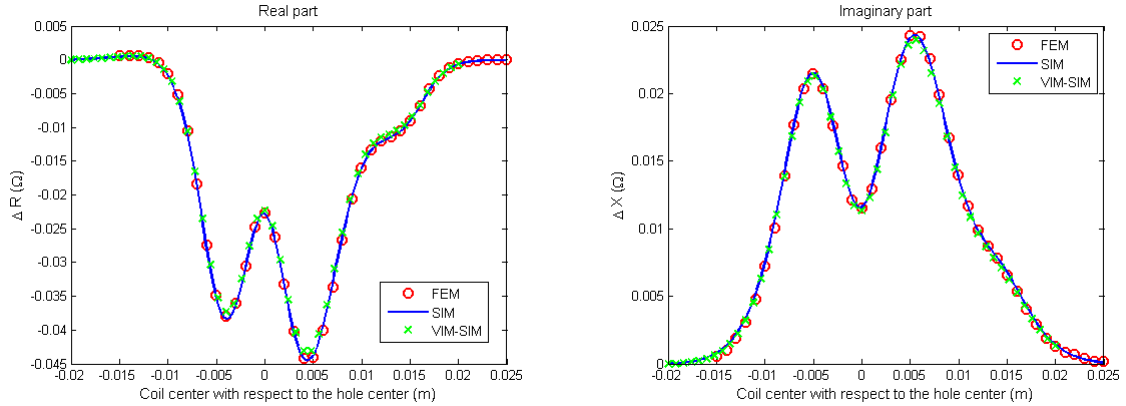


Figure 4.4: Impedance variation vs. coil position along a scan line passing above the borehole and the crack.

The presence of the flaw can be easily identified also in the complex plane representation of the signal. Fig. 4.5 shows the real versus imaginary part for the case of the flawless work-piece (left) and the case with a defect (right). In the first case the complex plane curve has two identical branches, with each branch illustrating the values for the coil scan on one of the sides of the borehole axis, whereas the two branches do not coincide.

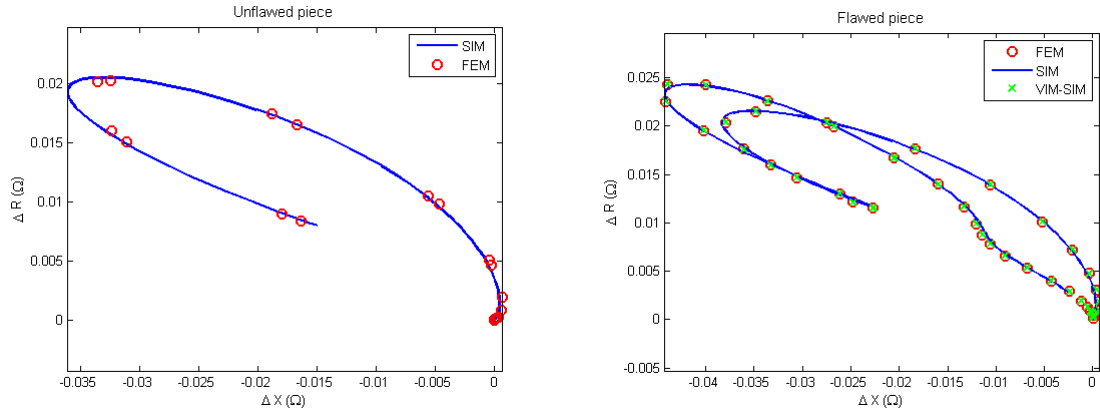


Figure 4.5: Simulation data for the real part vs. the imaginary part of the impedance variation due to the crack in the presence of the borehole. The coil is operated at 1 kHz.

Conclusions and numerical treatment

The total eddy-current signal of the SIM model (solid line) is compared with simulations of the FEM model (circles) and of the VIM-SIM model (crosses). From Fig. 6.7 one can deduce that there is very good agreement of the three models. Table 4.2 summarises all the solver parameters, as far as the truncation, modes number and the crack discretisation is concerned. The computational time is also given in this table in order to compare the speed of the model compared to that of the other models. We see that the presented model provides an important gain in computational time, compared to the VIM-SIM and the FEM models.

Table 4.2: Simulation parameters and computational time for a conducting half-space with a borehole and a narrow crack

Configuration data		Modes number		Crack discretisation	
Axial truncation (h)	30 mm	Azimuthal (Nm)	60	ρ -elements	11
Radial truncation (ρ_L)	20 mm	Axial/radial (N_κ, N_s)	100	z -elements	2
Lower conductor level	4 mm	Axial/radial (N_p, N_ξ)	300		
Upper conductor level	17 mm				
Computational time: 229 sec (SIM) - 2890 sec (VIM-SIM) - 168 sec/pos. (FEM)					

4.1.2 Plate with a borehole and a crack

In this subsection, we present the results of the model for a conducting plate with a borehole and a crack (Fig. 6.8). In other words, the complexity added with respect to the case treated in Subsection 4.1.1 is the reflection of the field from the lower interface of the plate. This case is a step towards the real application of the aircraft fastener holes inspection. In this context, we treat two test cases.

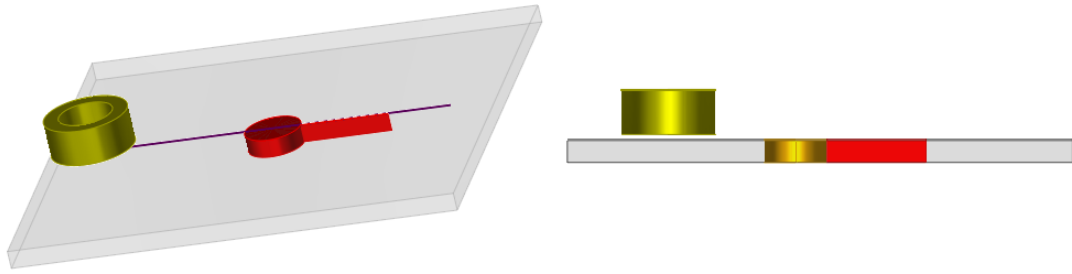


Figure 4.6: 2 mm-thick plate with borehole and a crack.

Test case 1

As a first test case, we examine the configuration of Subsection 4.1.1, where a plate of 2mm instead of a halfspace is considered. The crack is a through crack. The coil is operated this time at 4 kHz. Table 4.3 summarises the parameters of the test case configuration.

Table 4.3: Test case 1: Simulation parameters for a conducting plate with a borehole and a narrow crack

	Coil	Piece	Crack
Inner diameter	6 mm	Conductivity	10 MS/m
Outer diameter	9.3 mm	Thickness	2 mm
Length	4 mm	Hole diameter	6.25 mm
Turns	336		Opening
Lift-off	0.5 mm		0.1 mm

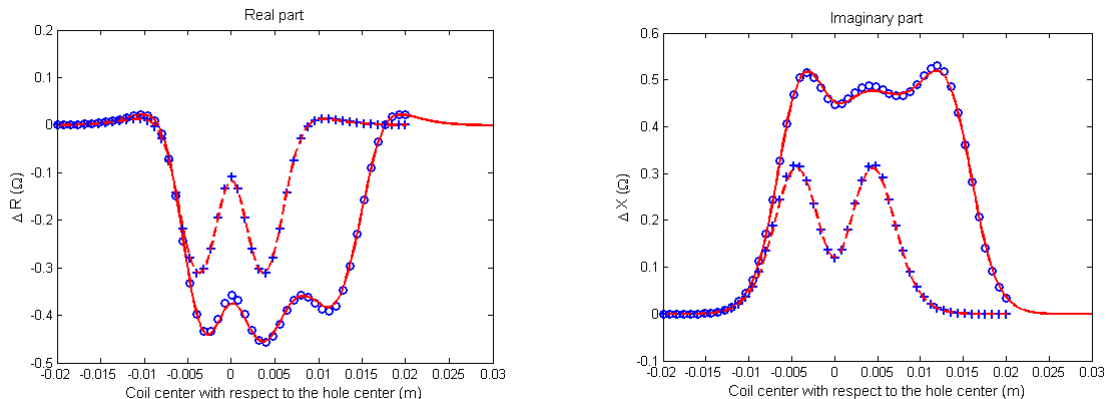


Figure 4.7: Impedance variation vs. coil position. The total signal simulated with VIM-SIM (circles) and SIM (solid line) as well as the hole signal as calculated with VIM-SIM (crosses) and SIM (dashed line) are illustrated.

In Fig. 4.7 we see the impedance variation of the coil in both cases of the flawless piece and in presence of the defect. The results of the SIM model are compared with those of the VIM-SIM model. The reflection from the lower interface (and, as a consequence, of

the multiple reflections in the plate) as well as the change of the eddy-currents flaw due to the through crack render the impact of the crack on the total ECT signal very important. In this case the asymmetry of the ECT signal around the hole center for the flawed piece is clear. The presence of the flaw is also easily distinguishable in the complex plane if we compare the two figures in Fig. 4.8.

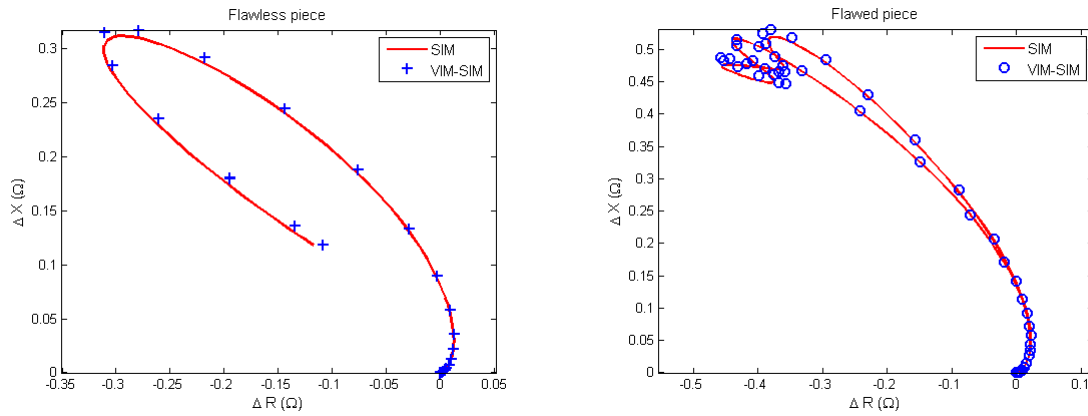


Figure 4.8: Complex plane of the impedance variation due to the flawless piece and the piece with a crack at the vicinity of the borehole.

Furthermore, the complex plane representation of the signal due to the crack in the presence of the borehole (Fig. 4.9) illustrates the validity of the Green's function.

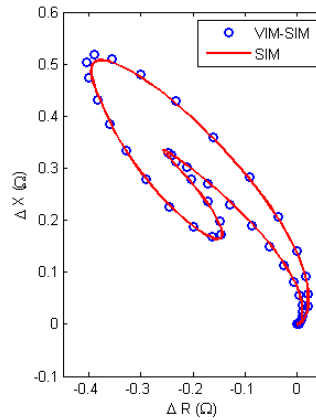


Figure 4.9: Complex plane representation of the impedance variation due to the crack in the presence of the borehole.

Conclusions and numerical treatment. Table 4.4 gives the simulation parameters used in the simulation of this test case, as well as the computational time for each model used in this test case.

As far as the computational time is concerned, we notice, on the one hand, an increase in the case of the SIM model with respect to the halfspace computational time in Table 4.2. This increase is mainly due to the increase of the azimuthal modes needed for

Table 4.4: Simulation parameters chosen and computational time for a conducting plate with a borehole and a narrow crack for the test case 1

Configuration data		Modes number		Crack discretisation	
Axial truncation (h)	35 mm	Azimuthal (N_m)	110	ρ -elements	8
Radial truncation (ρ_L)	52 mm	Axial/radial (N_κ, N_s)	150	z -elements	4
Lower conductor level	6 mm	Axial/radial (N_p, N_ξ)	100		
Upper conductor level	8 mm				
Computational time: 420 sec (SIM) - 660 sec (VIM-SIM)					

convergence and the higher operation frequency which requires denser discretisation of the crack. On the other hand, in the case of the VIM-SIM model, despite the higher frequency which requires finer mesh of the borehole and crack discretisation [MRT⁺14b], there is an important decrease of the computational time. This decrease is due to the decrease of the plate thickness and thus, of the borehole volume. Since the VIM-SIM treats the borehole as a flaw and requires its discretisation in order to solve the volume integral equation [MRT⁺14b], the computational time is proportional with the borehole volume. More precisely, in order to simulate the inspection in the case of the half-space in Subsection 4.1.1 we have considered a conductor 13 mm thick, whereas in the case of the plate the conductor is 2 mm thick. Hence, the height of the borehole is also 13 mm and 2 mm in the two cases, respectively. This difference in the borehole volume explains the difference in computational time.

Considering this example, we see that the gain in computational time that our model provides depends on several parameters. As mentioned, the SIM model in contrast to the VIM-SIM does not require the discretisation of the borehole. Thus, the bigger the borehole is, the more significant the gain becomes. Additionally, the parameters affecting the discretisation of the borehole play an important role. Therefore, the smaller the coil or the higher the excitation frequency is, the denser the borehole flaw discretisation is, which has a greater impact on the computational time of VIM-SIM than of SIM.

Test case 2

The second test case in this geometry is the 2013 benchmark problem of the WFNDEC [MRT14a]. The geometrical parameters of this problem are given in Table 6.2.

The simulations with the SIM model are compared with the experimental measurements conducted for the 2013 benchmark. Fig. 6.9 depicts the real and the imaginary part of the coil impedance variation for both the cases of the flawless work-piece and in the presence of the crack, whereas Fig. 4.11 illustrates the coil impedance variation due to the crack in presence of the borehole in the complex plane. The asymmetry of the signal is again noticed when the crack is present. However, the asymmetry now is weaker than in the case of Fig. 4.7. This is explained by the larger diameter borehole that overshadows the effect of the crack on the ECT signal.

Table 4.5: Test case 2: Parameters of the 2013 benchmark problem of the WFNDEC

Coil	Piece		Crack		
Inner diameter	12 mm	Conductivity	17.34 MS/m	Length	9.8 mm
Outer diameter	24 mm	Thickness	2 mm	Depth	2 mm
Length	4 mm	Hole diameter	20 mm	Opening	0.234 mm
Turns	1650				
Lift-off	1.08 mm				

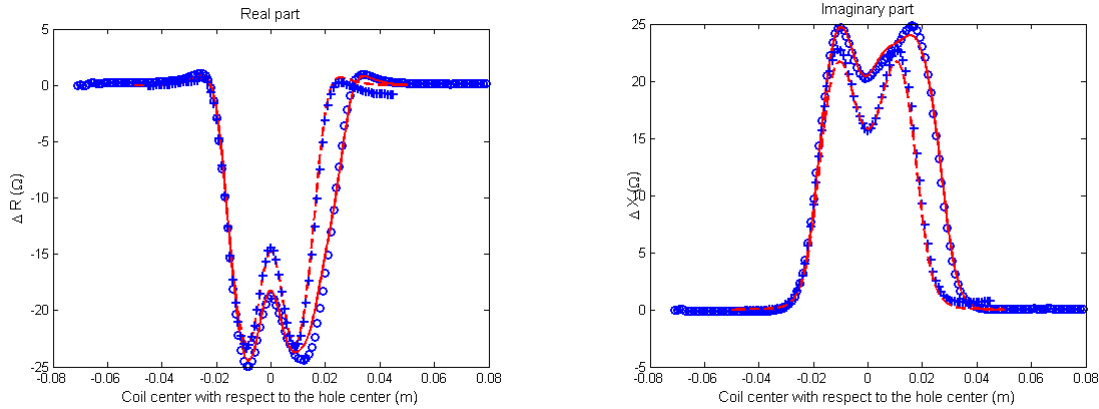


Figure 4.10: Theoretical and measured data for the impedance variation vs. coil position for the configuration of Table 6.2. The solid line represents the SIM results for the total signal, whereas the dashed line stands for the hole signal. The SIM results are compared against the measured signals in both cases (given by circle and cross markers, respectively).

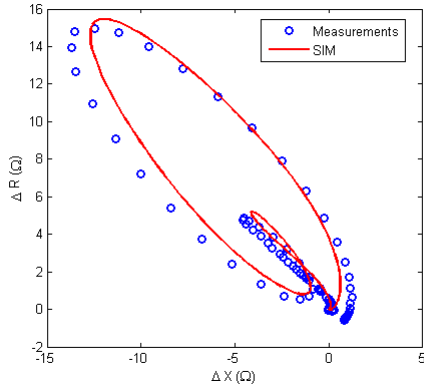


Figure 4.11: Theoretical and measured data for the real part vs. the imaginary part of the impedance variation due to the crack in the presence of the borehole.

Conclusions and numerical treatment. Table 4.6 gathers the parameters used for the simulation.

The computational time for simulations of this problem with the VIM-SIM problem is 3360 seconds for a good accuracy [MRT14a].

Note that the number of radial modes needed for good accuracy, a parameter which affects the computational time, is significantly higher than for the first test case. This can

Table 4.6: Simulation parameters and computational time for a conducting plate with a borehole and a narrow crack (test case 2)

Configuration data		Modes number		Crack discretisation	
Axial truncation (h)	30 mm	Azimuthal (N_m)	120	ρ -elements	4
Radial truncation (ρ_L)	26 mm	Axial/radial (N_κ, N_s)	100	z -elements	7
Lower conductor level	17 mm	Axial/radial (N_p, N_ξ)	550		
Upper conductor level	15 mm				
Computational time:	480 sec (SIM)				

be explained by examining the effect of the argument of the J-Bessel functions ($J_m(\kappa_n \rho)$). The more significant the argument is, the smaller is the value of $J_m(\kappa_n \rho)$ (see Fig. ?? in Appendix ??), and thus more terms are needed for convergence. Let us examine separately the two terms of the quantity $\kappa_n \rho$. The larger the distance is, where the crack is located in the radial direction (bigger ρ), the larger this quantity becomes. Moreover, as we have seen in Chapter 3 the eigenvalues κ_n are calculated by $J_m(\kappa_n \rho_L) = 0$. As a consequence, the larger is the truncation distance in the radial direction (bigger ρ_L), the smaller the values of κ_n are. Additionally, the minimum truncation distance ρ_L that we can choose is determined, on the one hand, by the skin depth $\delta = \sqrt{\frac{2}{\sigma \omega \mu}}$, as for lower operation frequencies one needs to truncate at a larger distance and, on the other hand, by the radial extension of the borehole-crack system, which implies truncation at a larger distance for higher borehole diameters or crack lengths.

Considering this analysis, it turns out that the borehole diameter affects the computational time in an indirect way, despite the fact that the SIM model avoids its discretisation. However, the cost in computational time for larger diameter boreholes remains lower for SIM than for VIM-SIM model.

4.2 Conducting tube

In this section we present results validating our model in which the reflection from the external radial interface is not negligible. In fact, this case is faced with in the inspection of steam generator tubes in nuclear power plants.

In the first subsection, results of the induction problem, when a coil is moved inside the tube, are presented. The coil impedance variation simulated with SIM is validated by comparing it with results from a commercial FEM platform (COMSOL). In the second subsection, results of the tube inspection in presence of a crack at the edge of the tube are presented. The model is again validated by comparing with FEM simulations.

4.2.1 Flawless tube

In this subsection the induction problem model for a semi-infinite flawless conducting tube is considered (Fig. 4.12). A coil scans inside the flawless tube, the impedance of which is subject to a change when it is moving close to the geometrical discontinuity of the tube edge. This impedance change due to the geometrical perturbation is called "edge effect" or "end effect".

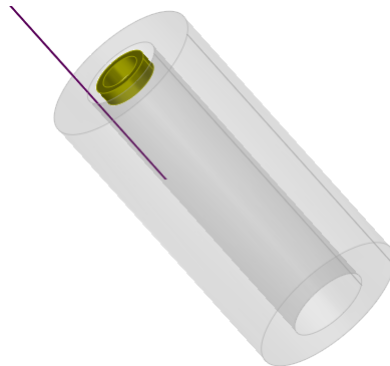


Figure 4.12: 5mm-thick flawless tube.

Table 4.7 shows the parameters of the considered test case. Simulations using the SIM model have been carried out for three operation frequencies, at 1 kHz, 5 kHz and 10 kHz, and the results have been compared with the COMSOL results.

Table 4.7: Test case 1: Simulation parameters for a semi-infinite tube

	Coil	Piece	
Inner diameter	3 mm	Conductivity	10 MS/m
Outer diameter	5 mm	Thickness	5 mm
Length	4 mm	Hole diameter	6.25 mm
Turns	336		
Offset	0.0 mm		

Fig. 4.13 and Fig. 4.14 illustrate the end effect for 1 kHz, 5 kHz and 10 kHz, respectively. The two models are in very good agreement. Table 4.8 gives the simulation parameters of the SIM simulations for 1 kHz in blue, 5 kHz in red and 10 kHz in black. From the simulation parameters one notes that for lower frequencies the domain must be truncated at a greater axial distance from the edge, which requires more eigenvalues and the computational time correspondingly becomes higher. It is also noted that there is need for only one azimuthal mode in the test case presented because the coil center is aligned with the axis of radial symmetry of the tube (zero coil offset). In case where the rotational symmetry of the system coil-tube is violated there is need of higher order azimuthal modes. The more important the coil offset is, the more azimuthal modes are needed for convergence of the ECT signal. Finally, there is a remarkable performance

improvement in terms of computational time with the SIM model compared to the FEM model.

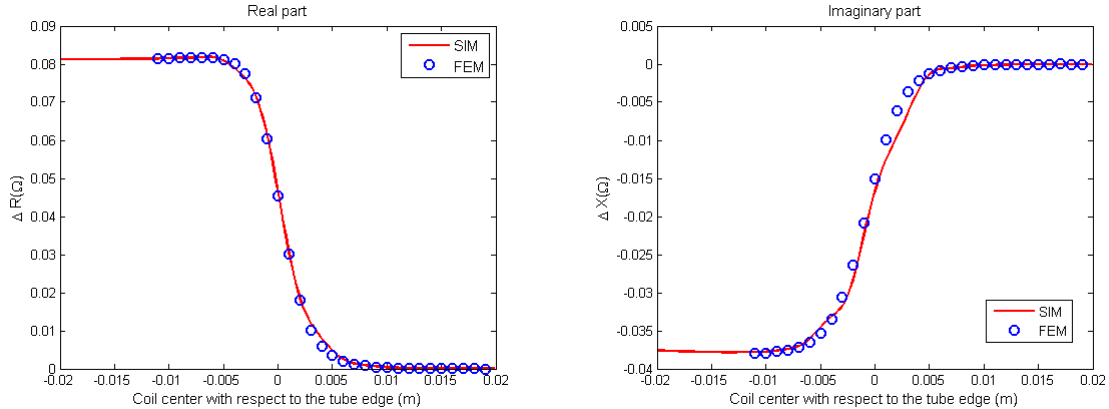


Figure 4.13: Impedance variation vs. coil position along a scan line inside the flawless tube. The coil is operated at 1 kHz.

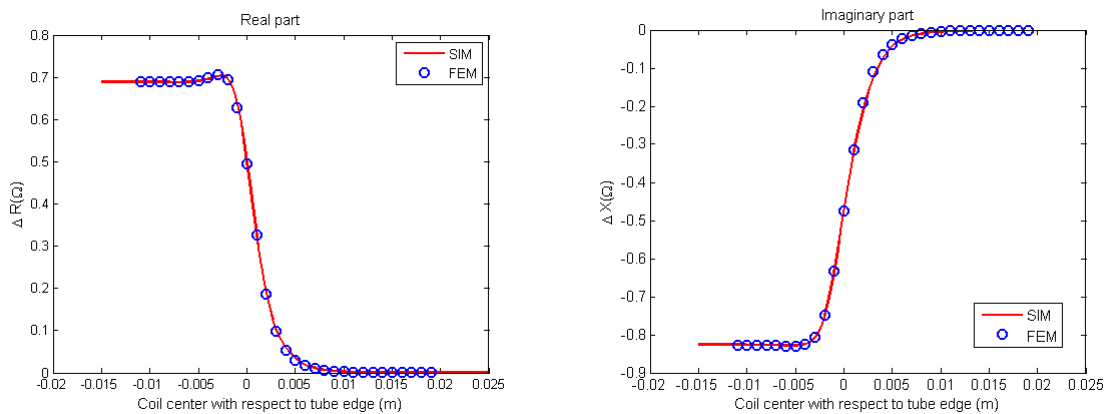


Figure 4.14: Impedance variation vs. coil position along a scan line inside the flawless tube. The coil is operated at 5 kHz.

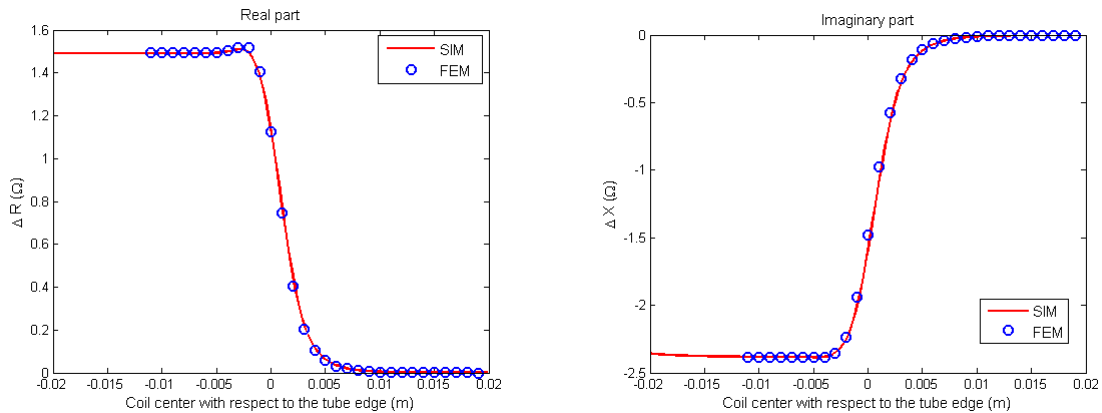


Figure 4.15: Impedance variation vs. coil position along a scan line inside the flawless tube. The coil is operated at 10 kHz.

Table 4.8: Simulation parameters and computational time for a flawless, semi-infinite, conducting tube inspection.

Frequency: 1kHz/5kHz/10kHz

Configuration data		Modes number	
Axial truncation (h)	900/650/60 mm	Azimuthal (N_m)	1/1/1
Conductor level (c)	40/40/30 mm	Axial (N_p, N_ξ)	500/350/40
Computational time:		47/15/0.3 sec (SIM) - 60 sec/coil position (FEM)	

4.2.2 Crack at the edge of the tube

The inspection of the semi-infinite conducting tube of Subsection 4.2.1 with a crack added at the edge is presented in this subsection (Fig. 6.10). We examine again three operation frequencies: 1 kHz, 5 kHz and 10 kHz.

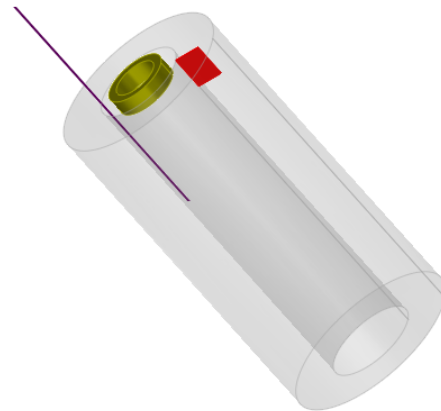


Figure 4.16: 5 mm-thick tube with a 3 mm x 4 mm narrow crack located at the edge of the tube.

Table 4.9: Simulation parameters for a semi-infinite tube with a crack at the edge.

Coil	Piece		Crack		
Inner diameter	3 mm	Conductivity	10 MS/m	Length	3 mm
Outer diameter	5 mm	Thickness	5 mm	Depth	4 mm
Length	4 mm	Hole diameter	6.2 mm	Opening	0.1 mm
Turns	336				
Offset	0.0 mm				

Table 6.3 summarises the geometrical parameters of the problem. In Fig. 4.17 the real and the imaginary parts of the ECT signal for different coil positions as simulated with the SIM and the FEM model are illustrated. The two models are again in very good agreement, but if we compare Fig. 4.13 and Fig. 4.14 with Fig. 4.17 and Fig. 4.18, respectively, the impact of the crack on the total ECT signal is not easy to identify and it

can be totally overshadowed by the end effect for small frequencies (i.e., for an operation frequency of 1 kHz in our test case) and for small cracks.

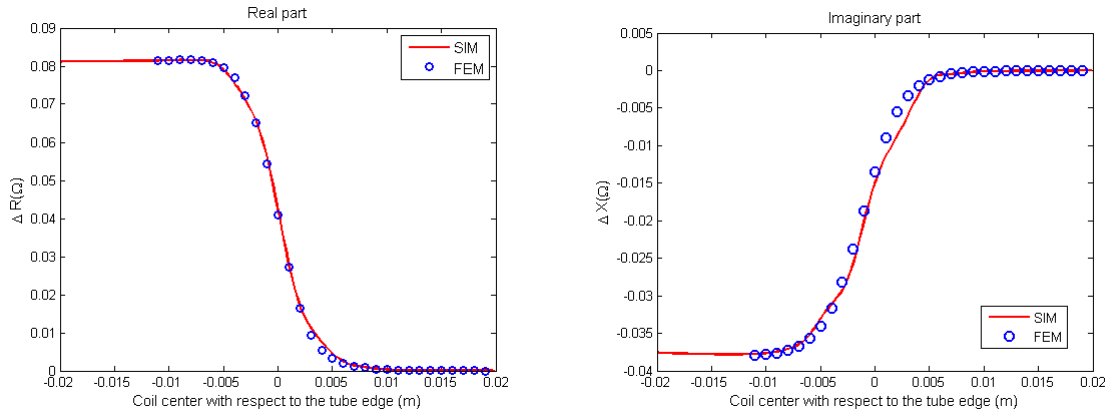


Figure 4.17: Impedance variation vs. coil position along a scan line inside the tube. The operation frequency is 1 kHz.

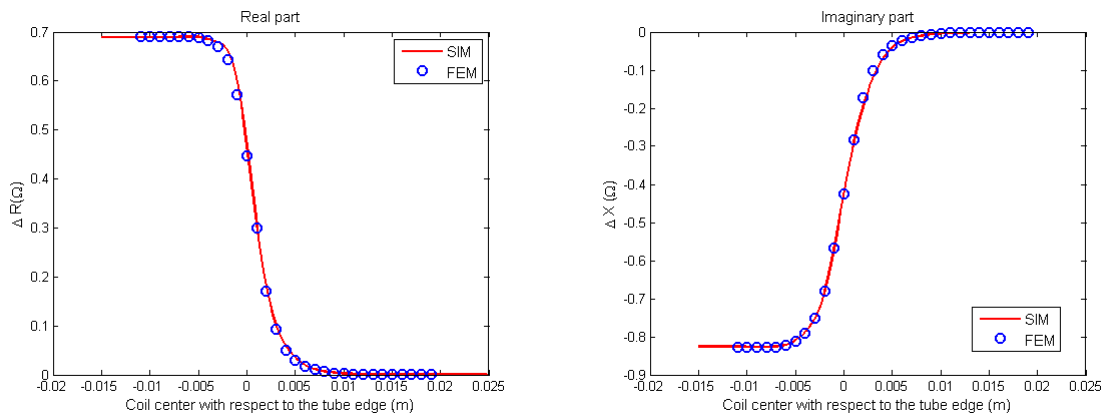


Figure 4.18: Impedance variation vs. coil position along a scan line inside the tube. The operation frequency is 5 kHz.

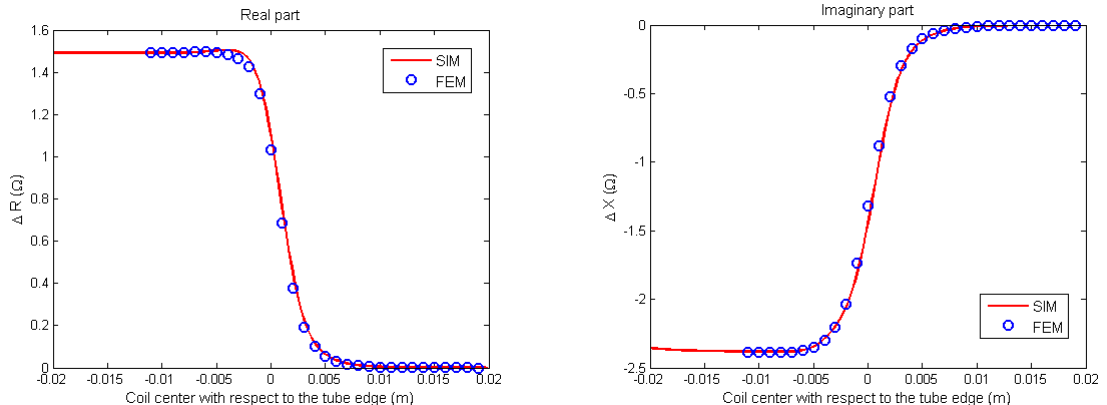


Figure 4.19: Impedance variation vs. coil position along a scan line inside the tube. The operation frequency is 10 kHz.

Table 4.10 summarises the simulation parameters for the three frequencies. The conclusions drawn in this case are similar to those about the flawless tube simulation in Subsection 4.2.1. The operation frequency is linked to the domain truncation distance, which increases for lower frequencies. Moreover, the number of axial modes to be taken into account is dependent on the truncation distance and the larger the truncation distance is, the higher the number of axial modes needed is.

Table 4.10: Simulation parameters and computational time for the inspection of a semi-infinite, conducting tube with a narrow crack at the edge

Frequency: 1kHz/5kHz/10kHz

Configuration data		Modes number	Crack discretisation	
Axial trunc. (h)	190/190/100 mm	N_m	40/40/40	ρ -elements 2/2/2
Radial trunc. (r_L)	50/50/40 mm	N_κ, N_s	100/100/100	z -elements 4/3/3
Edge level (c)	40/40/30 mm	N_p, N_ξ	100/100/60	

Computational time: 74 sec/56 sec/26 sec (SIM) - 90 sec/coil position (FEM)

Chapter 5

Conclusion

5.1 Work recapitulation

A model for the eddy-current inspection modelling of cylindrical work-pieces affected by a narrow crack has been presented. This model is based on an integral equation method, the so-called SIM method. A cylindrical conducting work-piece has been selected in order to simulate the inspection of several applied geometries, such as a conducting plate with a borehole, which is met in aeronautics for the inspection of rivet holes, or a semi-infinite conducting tube, which finds application in the nuclear and petrochemical industry, as well as in metallurgy. The configuration of a conducting plate can be approximated by assuming infinite radial thickness and finite axial thickness of the starting cylindrical geometry conductor, whereas the conducting tube is approximated by considering finite radial and semi-infinite axial thickness of the conductor.

In Chapter 3 the eddy-current inspection problem is tackled in three distinct steps. At first the induction problem of the flawless geometry is solved by using the TREE method and the impedance change of the coil is calculated by using the reciprocity theorem. Next, a dedicated Green's kernel that takes into account the hole is constructed following again the TREE method. The third step consists in using the field induced in the conductor and the Green's kernel in order to solve the dedicated integral equation by means of the MoM, and the ECT signal is finally calculated by using the reciprocity theorem.

In Chapter 4, the model is validated by comparing the results of the SIM model with the VIM-SIM, the FEM model as well as with experimental measurements. The model shows good performance both in terms of accuracy and computational time also.

The SIM model is a powerful tool for the inspection of the geometries treated in this work. Furthermore, the developed model can treat the problem of borehole inspection when the scanning probe enters into the hole region, a case that cannot be tackled by the VIM approach, where the hole is considered as a supplementary defect. This possibility is of much interest in the aeronautic industry, where inspections with bolthole scanning probes (e.g. rotating coils) are conducted [UM04]. Nonetheless, there can be improvement and extension of the presented model and we give here some suggestions for future works.

5.2 Perspectives

The SIM model can be enhanced in order to improve the performance in more complex applications and deal with even more realistic cases of the applications treated.

Indeed, the model presented herein can only deal with cracks, the orientation of which is along the radial direction. The calculation of the entire Green's dyad will lead to the inspection of the same geometries, when they are affected by cracks of any orientation.

Also, the model can be extended in order to make it compatible with other types of sensors, such as D-coils, coil arrays, etc., with ferrite coils, as well as to model the inspection by two different coils (emission-reception coils) with different inclination of their centres axis or to study the effect of the coil tilt (Fig. 5.1).

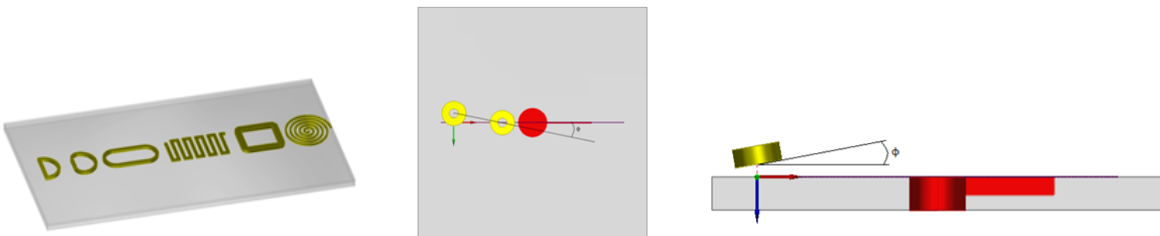


Figure 5.1: Model enhancement referring to the coils characteristics. Coil types (left), emission-reception coils (middle) and tilted coil (right).

Besides, the model can be extended in order to take into account a more realistic configuration of the rivet, that is to say, in order to inspect a multi-layer conducting plate as well as to model the rivet head by using the VIM-SIM model (Fig. 5.2). In fact,

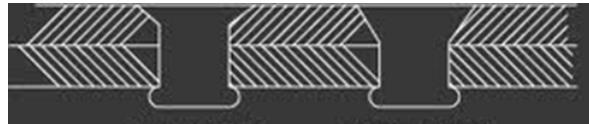


Figure 5.2: Cross section of rivets. The rivet heads present an increasing diameter from the lower part to the top of the head.

the fastener holes in the aeronautical industry are composed by a number of superposed aluminium plates with a borehole. The model extension could take into account a superposition of j layers including non-magnetic materials of different conductivities σ_j as well as ferromagnetic materials of different permittivities μ_j .

Moreover, an important enhancement of the model that will lead to a significant reduction of the inspection time is to model the inspection of a conducting plate with a conducting inclusion at the place of the hole (Fig. 5.3). Such a configuration corresponds with the inspection of fastener holes in the presence of the conducting fastener.

Further, the model can be extended in order to calculate the ECT signal affected by a series of rivets (Fig. 5.4). This is the case that better approximates the inspection of



Figure 5.3: Fastened rivet holes.

airplane fasteners, since many fasteners are located in close distance from one another.

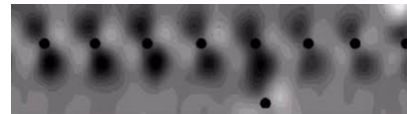


Figure 5.4: C-scan of a Rivet array.

Apart from the modelling of multi-layered plates with a borehole, stratification of tubes finds applications in nuclear technology. Thus, the development of a model for the inspection of axially and radially stratified tubes is intended (Fig. 5.5).

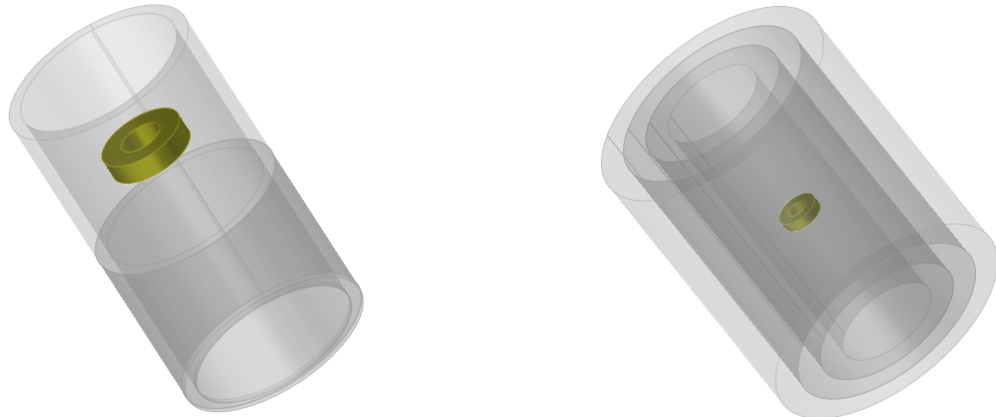


Figure 5.5: Inspection of axially (left) and radially (right) stratified tubes.

Regarding the perspectives proposed above, the ultimate goal is to develop a general model for the inspection with different coil types of a multi-layered structure with stratification in both ρ and z directions of both ferromagnetic and non-magnetic materials.

Chapter 6

Résumé

6.1 Introduction

Le contrôle non-destructif (CND) est l'ensemble des méthodes pour l'inspection, le contrôle ou l'évaluation de matériaux ou des systèmes concernant l'état d'intégrité ou leurs caractéristiques sans les dégrader de manière qu'ils puissent être réutilisés après le contrôle.

Le contrôle par courants de Foucault (CF) est une méthode CND qui utilise le phénomène d'induction. Le principe de la méthode est décrit par le phénomène suivant. Un courant alternatif excitant une bobine crée un champ magnétique, dit champ primaire, à la proximité de la bobine. Des courants électriques, dits courants de Foucault, sont induits dans une pièce conductrice autour du flux magnétique. Les courants de Foucault créent à leur tour un champ magnétique secondaire qui s'oppose au champ primaire. La valeur de l'impédance du capteur en présence de la pièce inspectée et loin de toute discontinuité dans cette pièce est souvent la valeur de référence de l'impédance. Une fois que les courants de Foucault rencontrent une discontinuité dans la pièce inspectée la densité de courant est affectée et ce changement est remarqué dans le champ magnétique secondaire et il est finalement détecté par la variation de l'impédance du capteur. Ainsi, une discontinuité dans la pièce peut être détectée et caractérisée.

La méthode CF est utilisée pour la détection et dimensionnement des défauts dans des pièces, la définition des caractéristiques électriques et géométriques des matériaux, etc. La fréquence d'opération de cette méthode varie entre 100 Hz et 10 MHz et elle est définie par la pénétration désirée du champ dans la pièce. Cette méthode trouve des applications dans plusieurs domaines comme dans l'aéronautique, l'industrie nucléaire, la métallurgie, l'industrie pétrochimique, etc. L'intérêt de ce travail se focalise dans la modélisation de l'inspection des pièces rivetées, comme les rivets trouvés dans l'aéronautique, avec un défaut au voisinage du rivet ainsi que des tubes conducteurs avec un défaut au bord, pour l'appliquer dans le secteur nucléaire.

La méthode proposée suit une formulation d'équation intégrale (IM). La formulation d'équation intégrale est une approche qui peut donner des simulations rapides pour un grand nombre de positions du capteur. Ainsi, la méthode d'intégrale volumique (VIM)

[Dun88] [SPL⁺08] modélise les défauts comme une distribution de dipôles électriques dans le volume du défaut. Le champ électrique est donc calculé par une équation intégrale liant le champ du à un dipole électrique au champ total du au défaut. De la même manière, le cas d'un défaut fin, défini comme un défaut d'une ouverture très fine par rapport à la taille du capteur et de l'épaisseur de peau, est traité comme une distribution surfacique de dipôles électriques et une intégration sur la surface du défaut plutôt que sur son volume est nécessaire. Dans ce cas, l'approche suivie est la méthode d'intégrale surfacique (SIM) [BTXJ12][KA04][KA09][PL06][The10][MRT⁺13]. Par ailleurs, [MRT⁺14b] propose une approche d'équation intégrale hybride qui utilise VIM pour traiter le rivet dans une pièce rivetée et SIM pour modéliser la fissure au voisinage de l'alésage. Cette approche est appelée VIM-SIM et elle a amené à une amélioration du temps de calcul.

Dans ce travail une approche d'équation intégrale est présentée, où la fissure est modélisée avec SIM, en utilisant une dyade de Green prenant en compte la présence de l'alésage, comme présenté à [BTP12]. La méthode TREE (Truncated Region Eigenfunction Expansion) est utilisée pour la dérivation de l'opérateur de Green [TK06]. Cette méthode utilise la dégradation rapide du champ pour tronquer le domaine du problème à une distance où le champ est négligeable et permet l'expression du champ par une expansion modale.

6.2 Inspection des pièces cylindriques

6.2.1 Description du problème

La géométrie se compose d'une pièce conductrice, non-magnétique et cylindrique avec une inclusion d'air (Fig. 6.1). La pièce est homogène de conductivité σ et de perméabilité μ_0 . Un défaut fin est situé dans la partie conductrice de la pièce. Un défaut fin se comporte comme une barrière de courant [Bow94, BNH94]. Cela permet la représentation de l'effet du défaut par une distribution surfacique de dipôles électriques lorsque des courants de Foucault sont induits dans la pièce. La géométrie est inspectée par une bobine excitée par un courant harmonique $Ie^{j\omega t}$ qui se déplace au dessus de la pièce ou dans l'alésage.

La solution du problème CF se focalise sur le calcul de la variation de l'impédance (ΔZ) du capteur pour un ensemble de positions par rapport à la pièce. Ce signal est appelé signal CF.

Le signal CF est calculé en trois étapes. La première étape est la solution du problème électromagnétique en absence de défauts. Dans cette étape le champ primaire est calculé, ainsi que la variation de l'impédance du capteur due à la pièce sans défaut à l'aide du théorème de réciprocité. En ce qui concerne la deuxième étape, il s'agit de la construction de la fonction de Green correspondant à la géométrie inspectée. Enfin, la troisième étape correspond à la solution de l'équation intégrale associée au problème CF et au calcul

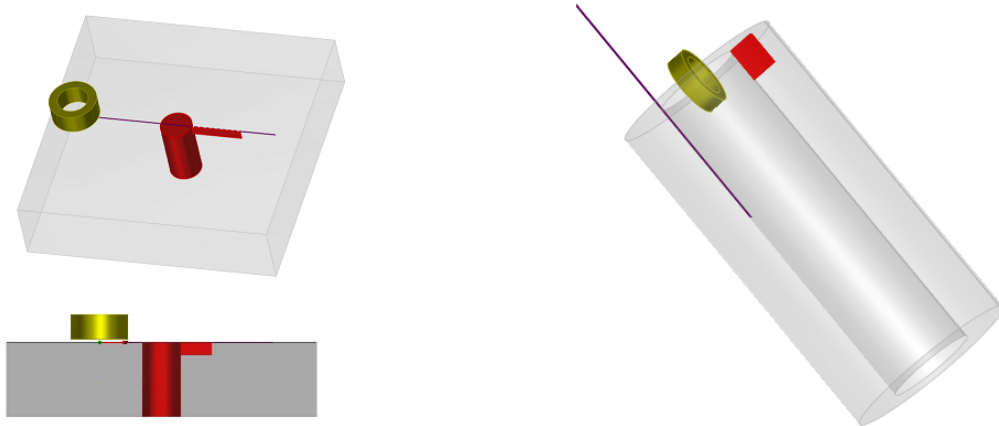


Figure 6.1: Inspection d'une pièce cylindrique d'épaisseur axiale et radiale différentes avec une inclusion d'air et un défaut. Le capteur est localisé en dessus de la pièce inspectée ou dans l'inclusion d'air.

du changement de l'impédance dû au défaut avec le théorème de réciprocité. Dans les prochain paragraphes, les trois étapes sont examinées.

6.2.2 Calcul du champ primaire

Dans ce paragraphe le calcul du champ primaire pour le cas d'un capteur situé dans un tube conducteur et semi-infini de rayon interne b_1 et externe b_2 et calculé. La stratégie suivie est celle proposée dans [ST15].

Le densité du flux magnétique \mathbf{B} dans les régions d'air est exprimé par un potentiel scalaire $\mathbf{B} = \nabla\phi$ qui satisfait l'équation de Laplace $\nabla^2\phi = 0$. En outre, la formulation suivie pour les régions conductrices représente la densité du flux magnétique avec une approche de potentiel vectoriel de second ordre. Selon cette approche $\mathbf{B} = \nabla \times \nabla \times \mathbf{W}$, avec $\mathbf{W} = W_a \mathbf{e}_z + \mathbf{e}_z \times \nabla W_b$. W_a et W_b représentent les termes TE et TM, respectivement, et ils satisfont l'équation de Helmholtz $(\nabla^2 - k^2)W_{a,b} = 0$, où $k^2 = j\omega\mu_0\sigma$.

Fig. 6.2 illustre une coupe $\rho - z$ du tube. Une bobine de rayon interne et externe r_a and r_b , respectivement, de longueur H_c et comportant N spires se déplace dans l'alésage. La distance entre l'axe z de la bobine et celui de l'alésage est r_0 . Le domaine d'intérêt est tronqué selon la méthode TREE à $z = 0$ et $z = h$, où des conditions de champ électrique tangentiel zéro (conducteur électrique parfait - PEC) et de densité du flux magnétique tangentiel zéro (conducteur magnétique parfait - PMC) sont considérées, respectivement. Le domaine est aussi séparé en trois sous-régions, où le champ prend des expressions différentes. Dans chaque région les potentiels sont exprimés par des expansions modales à l'aide des fonctions de Bessel modifiées. Dans la région I il y a deux termes du champ :celui provenant du capteur (ϕ^s) et celui du à la perturbation du champ par la pièce. En plus, dans la région II et la superposition du champ s'éliminant vers $\rho \rightarrow \infty$ (noté avec l'indice $\rho^>$) et celui s'éliminant vers $\rho \rightarrow 0$ (noté avec l'indice $\rho^<$). Le premier correspond au champ émis par le capteur ainsi qu'à la perturbation due à l'interface $\rho = b_1$ et il

est exprimé avec des fonctions de Bessel K_m . Aussi, le deuxième correspond au champ perturbé par l'interface $\rho = b_2$ et il est exprimé avec des fonctions de Bessel I_m . Dans la suite du manuscrit cette superposition est notée avec $\left\{ \right\}$ et les notations $\rho^>$ and $\rho^<$ sont fusionnées en ρ^{\leq} . Enfin, dans la région III il n'y a qu'un terme regroupant le champ provenant du capteur et la perturbation par le conducteur. Les expressions des potentiels dans chaque région sont

$$\phi^s = \sum_{m=-\infty}^{m=\infty} \sum_{n=1}^{\infty} A_{mn}^s \cos(w_n z) K_m(w_n \rho) e^{jm\varphi} \quad (6.1)$$

$$\phi^I = \sum_{m=-\infty}^{m=\infty} \sum_{n=1}^{\infty} A_{mn} \cos(w_n z) I_m(w_n \rho) e^{jm\varphi} \quad (6.2)$$

$$\phi^{II} = \sum_{m=-\infty}^{m=\infty} \sum_{n=1}^{\infty} B_{mn}^{\rho \leq} \sin(p_n(h-z)) \begin{Bmatrix} K_m(p_n \rho) \\ I_m(p_n \rho) \end{Bmatrix} e^{jm\varphi} ; \quad c \leq z \leq h \quad (6.3)$$

$$W_a^{II} = \sum_{m=-\infty}^{m=\infty} \sum_{n=1}^{\infty} C_{mn}^{\rho \leq} \sin(q_n z) \begin{Bmatrix} K_m(p_n \rho) \\ I_m(p_n \rho) \end{Bmatrix} e^{jm\varphi} ; \quad 0 \leq z \leq c \quad (6.4)$$

$$W_b^{II} = \sum_{m=-\infty}^{m=\infty} \sum_{n=1}^{\infty} D_{mn}^{\rho \leq} \cos(\nu_n z) \begin{Bmatrix} K_m(\xi_n \rho) \\ I_m(\xi_n \rho) \end{Bmatrix} e^{jm\varphi} ; \quad 0 \leq z \leq c \quad (6.5)$$

$$\phi^{III} = \sum_{m=-\infty}^{m=\infty} \sum_{n=1}^{\infty} E_{mn} \cos(w_n z) K_m(w_n \rho) e^{jm\varphi}, \quad (6.6)$$

où $p_n^2 = q_n^2 + k^2$ and $\xi_n^2 = \nu_n^2 + k^2$.

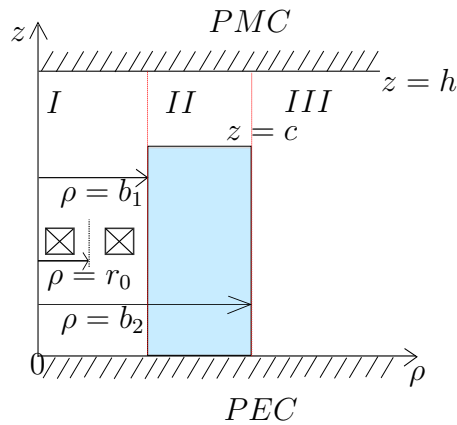


Figure 6.2: Coupe ρ - z d'un tube semi-infini.

La procédure qui amène au calcul des potentiels (6.2)-(6.6) comprend les étapes suivantes.

Les coefficients A_{mn}^s dépendent seulement des caractéristiques géométriques du capteur, de son excitation et sa position, et ils se trouvent dans la littérature [TB08].

L'application des conditions PEC et PMC sur les interfaces de troncature et la condition de zéro densité de courant normal sur l'interface horizontale du tube $z = c$ nous permettent de calculer les valeurs propres

$$\cos(w_n h) = 0 \Leftrightarrow w_n = \frac{(2n - 1)\pi}{2h} \quad (6.7)$$

et

$$\cos(\nu_n c) = 0 \Leftrightarrow \nu_n = \frac{(2n - 1)\pi}{2c}. \quad (6.8)$$

En outre, la continuité du champ sur le bord du tube $z = c$ donne une équation transcendante, dont la solution selon la méthode proposée en [Lyn67, DL67] donne les valeurs propres $p - q$

$$q_n \cot(q_n c) = p_n \tan(p_n(h - c)). \quad (6.9)$$

Enfin, l'application des conditions de continuité du champ sur les interfaces verticales $\rho = b_1$ et $\rho = b_2$ produit

$$\begin{aligned} w_n I'_m(w_n b_1) A_{mn} &= M_c(l, n) p_n \begin{Bmatrix} K'_m(p_n b_1) \\ I'_m(p_n b_1) \end{Bmatrix} C_{mn}^{\rho \leqslant} + \frac{k^2 j m}{b} M_r(l, n) \begin{Bmatrix} K_m(\xi_n b_1) \\ I_m(\xi_n b_1) \end{Bmatrix} D_{mn}^{\rho \leqslant} \\ &\quad - w_n K'_m(w_n b_1) A_{mn}^s \end{aligned} \quad (6.10)$$

$$\begin{aligned} \frac{j m}{b_1} I_m(w_n b_1) A_{mn} &= M_c(l, n) \frac{j m}{b_1} \begin{Bmatrix} K_m(p_n b_1) \\ I_m(p_n b_1) \end{Bmatrix} C_{mn}^{\rho \leqslant} - k^2 \xi_n M_r(l, n) \begin{Bmatrix} K'_m(\xi_n b_1) \\ I'_m(\xi_n b_1) \end{Bmatrix} D_{mn}^{\rho \leqslant} \\ &\quad - \frac{j m}{b_1} K_m(w_n b_1) A_{mn}^s \end{aligned} \quad (6.11)$$

et

$$w_n I_m(w_n b_1) A_{mn} = M_s(l, n) p_n \begin{Bmatrix} K_m(p_n b_1) \\ I_m(p_n b_1) \end{Bmatrix} C_{mn}^{\rho \leqslant} - w_n K_m(w_n b_1) A_{mn}^s, \quad (6.12)$$

$$w_n I'_m(w_n b_1) E_{mn} = M_c(l, n) p_n \begin{Bmatrix} K'_m(p_n b_1) \\ I'_m(p_n b_1) \end{Bmatrix} C_{mn}^{\rho \leqslant} + \frac{k^2 j m}{b} M_r(l, n) \begin{Bmatrix} K_m(\xi_n b_1) \\ I_m(\xi_n b_1) \end{Bmatrix} D_{mn}^{\rho \leqslant} \quad (6.13)$$

$$\frac{j m}{b_1} I_m(w_n b_1) E_{mn} = M_c(l, n) \frac{j m}{b_1} \begin{Bmatrix} K_m(p_n b_1) \\ I_m(p_n b_1) \end{Bmatrix} C_{mn}^{\rho \leqslant} - k^2 \xi_n M_r(l, n) \begin{Bmatrix} K'_m(\xi_n b_1) \\ I'_m(\xi_n b_1) \end{Bmatrix} D_{mn}^{\rho \leqslant} \quad (6.14)$$

$$w_n I_m(w_n b_1) E_{mn} = M_s(l, n) p_n \begin{Bmatrix} K_m(p_n b_1) \\ I_m(p_n b_1) \end{Bmatrix} C_{mn}^{\rho \leqslant}. \quad (6.15)$$

où

$$M_c(l, n) = \frac{2}{h} [q_n \int_0^c \cos(q_n z) \cos(w_l z) dz + \alpha_n \int_c^h \sin(p_n(h - z)) \cos(w_l z) dz] \quad (6.16)$$

$$M_s(l, n) = \frac{2}{h} [p_n \int_0^c \sin(q_n z) \sin(w_l z) dz - \alpha_n \int_c^h \cos(p_n(h - z)) \sin(w_l z) dz] \quad (6.17)$$

$$M_r(l, n) = \frac{2}{h} \int_0^c \cos(\nu_n z) \cos(w_l z) dz. \quad (6.18)$$

La solution de ce système conduit au calcul des coefficients $A, C^{\rho^<}, C^{\rho^>}, D^{\rho^<}, D^{\rho^>} et E$ et cela permet la définition analytique des potentiels dans les différentes régions et avec ceci le champ peut-être calculé à partir de ces potentiels.

Enfin, le changement de l'impédance due à la géométrie sans défaut peut être calculé à l'aide de la formule [TB08, ST12]

$$\Delta Z_{geom} = -\frac{j\omega}{\mu_0 I^2} \pi h \sum_{m=-\infty}^{\infty} \sum_{i=1}^{\infty} A_{mn}^s A_{mn}. \quad (6.19)$$

6.2.3 Fonction de Green

Dans ce paragraphe on considère la construction de la fonction de Green pour un tube conducteur et fini (Fig. 6.3). Un dipôle électrique est considéré dans le tube conducteur.

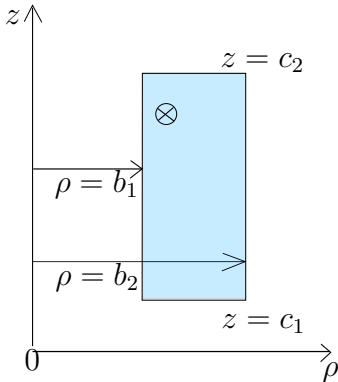


Figure 6.3: Coupe radiale d'un tube fini. Un dipôle électrique d'orientation selon φ est situé dans le conducteur dans le tube.

Le problème de la construction de la fonction de Green est divisé en deux sous-problèmes. Dans un premier temps, le champ émis par un dipôle électrique situé dans une plaque conductrice et tronqué à une distance radiale lointaine est calculé. Par la suite, les interfaces verticales du tube sont introduites et la perturbation du champ calculé dans le premier sous-problème due à ces interfaces est calculée.

Dipôle électrique dans une plaque conductrice

La Fig. 6.4 montre la configuration du premier sous-problème : une plaque conductrice, homogène et non-magnétique de conductivité σ et épaisseur $c_2 - c_1$, un dipôle électrique d'orientation selon φ est situé à $(\rho', 0, z')$, en plus, le domaine est tronqué à $\rho = \rho_L$.

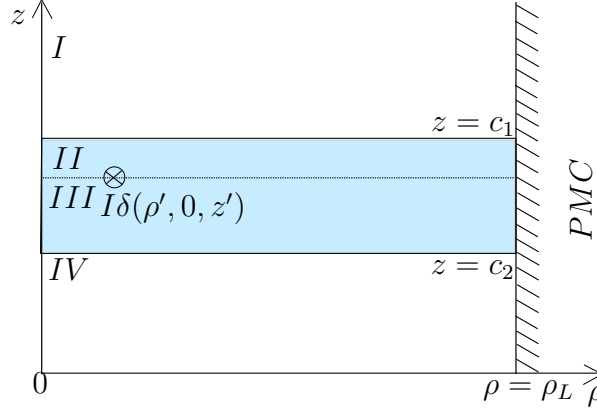


Figure 6.4: Coupe radiale d'une plaque conductrice d'épaisseur $c_2 - c_1$ avec un dipôle électrique d'orientation selon φ situé à $(\rho', 0, z')$.

Les potentiels sont exprimés de nouveau dans les différentes régions du domaine à l'aide de fonctions de Bessel :

$$\phi^I = \sum_{m=-\infty}^{m=\infty} \sum_{n=1}^{\infty} P_{mn} e^{-\kappa_n(z-z')} J_m(\kappa_n \rho) e^{jm\varphi} ; \quad z \geq c_2 \quad (6.20)$$

$$W_a^{II} = \sum_{m=-\infty}^{m=\infty} \sum_{n=1}^{\infty} (A_{mn} e^{-v_n(z-z')} + B_{mn} e^{v_n(z-z')}) J_m(\kappa_n \rho) e^{jm\varphi} ; \quad z' \leq z \leq c_2 \quad (6.21)$$

$$W_b^{II} = \sum_{m=-\infty}^{m=\infty} \sum_{n=1}^{\infty} (C_{mn} e^{-r_n(z-z')} + D_{mn} e^{r_n(z-z')}) J_m(s_n \rho) e^{jm\varphi} ; \quad z' \leq z \leq c_2 \quad (6.22)$$

$$W_a^{III} = \sum_{m=-\infty}^{m=\infty} \sum_{n=1}^{\infty} (E_{mn} e^{-v_n(z-z')} + F_{mn} e^{v_n(z-z')}) J_m(\kappa_n \rho) e^{jm\varphi} ; \quad c_1 \leq z \leq z' \quad (6.23)$$

$$W_b^{III} = \sum_{m=-\infty}^{m=\infty} \sum_{n=1}^{\infty} (L_{mn} e^{-r_n(z-z')} + M_{mn} e^{r_n(z-z')}) J_m(s_n \rho) e^{jm\varphi} ; \quad c_1 \leq z \leq z' \quad (6.24)$$

$$\phi^{IV} = \sum_{m=-\infty}^{m=\infty} \sum_{n=1}^{\infty} N_{mn} e^{\kappa_n(z-z')} J_m(\kappa_n \rho) e^{jm\varphi} ; \quad z \geq c_2 \quad (6.25)$$

où $v_n^2 = \kappa_n^2 + k^2$ et $r_n^2 = s_n^2 + k^2$.

En appliquant la condition PMC sur l'interface de troncature nous arrivons aux équations

$$J_m(\kappa_n \rho_L) = 0 \quad (6.26)$$

et

$$J'_m(s_n \rho_L) = 0 \quad (6.27)$$

et leur solution donne les valeurs propres κ et s . En plus, la continuité du champ sur les interfaces $z = c_1$, $z = z'$ et $z = c_2$ conduit aux expressions des coefficients modaux des potentiels TE :

$$A_{mn} = -\frac{\mu_0}{2\pi v_n \rho_L^2 \kappa_n} \frac{J'_m(\kappa_n \rho')}{J_{m+1}^2(\kappa_n \rho_L)} \frac{1 - \frac{\kappa_n + v_n}{\kappa_n - v_n} e^{-2v_n(c_1 - z')}}{\left(\frac{\kappa_n - v_n}{\kappa_n + v_n} e^{-2v_n c_2} - \frac{\kappa_n + v_n}{\kappa_n - v_n} e^{-2v_n c_1} \right) e^{2v_n z'}} \quad (6.28)$$

$$B_{mn} = \frac{\mu_0}{2\pi v_n \rho_L^2 \kappa_n} \frac{J'_m(\kappa_n \rho')}{J_{m+1}^2(\kappa_n \rho_L)} \frac{\frac{\kappa_n - v_n}{\kappa_n + v_n} - e^{-2v_n(c_1 - z')}}{\frac{\kappa_n - v_n}{\kappa_n + v_n} - \frac{\kappa_n + v_n}{\kappa_n - v_n} e^{-2v_n(c_1 - c_2)}} \quad (6.29)$$

$$E_{mn} = -\frac{\mu_0}{2\pi v_n \rho_L^2 \kappa_n} \frac{J'_m(\kappa_n \rho')}{J_{m+1}^2(\kappa_n \rho_L)} \frac{1 - \frac{\kappa_n - v_n}{\kappa_n + v_n} e^{-2v_n(c_2 - z')}}{\left(\frac{\kappa_n - v_n}{\kappa_n + v_n} e^{-2v_n c_2} - \frac{\kappa_n + v_n}{\kappa_n - v_n} e^{-2v_n c_1} \right) e^{2v_n z'}} \quad (6.30)$$

$$F_{mn} = \frac{\mu_0}{2\pi v_n \rho_L^2 \kappa_n} \frac{J'_m(\kappa_n \rho')}{J_{m+1}^2(\kappa_n \rho_L)} \frac{\frac{\kappa_n + v_n}{\kappa_n - v_n} - e^{-2v_n(c_2 - z')}}{\frac{\kappa_n - v_n}{\kappa_n + v_n} e^{-2v_n(c_2 - c_1)} - \frac{\kappa_n + v_n}{\kappa_n - v_n}} \quad (6.31)$$

$$N_{mn} = \frac{\mu_0}{2\pi v_n \rho_L^2 \kappa_n} \frac{J'_m(\kappa_n \rho')}{J_{m+1}^2(\kappa_n \rho_L)} \frac{\left(\frac{2\kappa_n v_n}{\kappa_n - v_n} - \frac{2\kappa_n v_n}{\kappa_n + v_n} e^{-2v_n(c_2 - z')} \right) e^{-(\kappa_n + v_n)c_1} e^{(\kappa_n + v_n)z'}}{\left(\frac{\kappa_n - v_n}{\kappa_n + v_n} e^{-2v_n c_2} - \frac{\kappa_n + v_n}{\kappa_n - v_n} e^{-2v_n c_1} \right)} \quad (6.32)$$

$$P_{mn} = \frac{\mu_0}{2\pi v_n \rho_L^2 \kappa_n} \frac{J'_m(\kappa_n \rho')}{J_{m+1}^2(\kappa_n \rho_L)} \frac{\left(\frac{2\kappa_n v_n}{\kappa_n + v_n} - \frac{2\kappa_n v_n}{\kappa_n - v_n} e^{-2v_n(c_1 - z')} \right) e^{(\kappa_n - v_n)c_2} e^{-(\kappa_n + v_n)z'}}{\left(\frac{\kappa_n - v_n}{\kappa_n + v_n} e^{-2v_n c_2} - \frac{\kappa_n + v_n}{\kappa_n - v_n} e^{-2v_n c_1} \right)} \quad (6.33)$$

et des potentiels TM :

$$C_{mn} = -j \frac{\mu_0 m}{2\pi k^2 (s_n^2 \rho_L^2 - m^2) \rho'} \frac{J_m(s_n \rho')}{J_m(s_n \rho_L)} \frac{e^{-2r_n(c_1 - z')} + 1}{(e^{-2r_n c_1} - e^{-2r_n c_2}) e^{2r_n z'}} \quad (6.34)$$

$$L_{mn} = -j \frac{\mu_0 m}{2\pi k^2 (s_n^2 \rho_L^2 - m^2) \rho'} \frac{J_m(s_n \rho')}{J_m(s_n \rho_L)} \frac{e^{-2r_n(c_2 - z')} + 1}{(e^{-2r_n c_1} - e^{-2r_n c_2}) e^{2r_n z'}} \quad (6.35)$$

$$D_{mn} = j \frac{\mu_0 m}{2\pi k^2 (s_n^2 \rho_L^2 - m^2) \rho'} \frac{J_m(s_n \rho')}{J_m(s_n \rho_L)} \frac{e^{-2r_n(c_1 - z')} + 1}{e^{-2r_n(c_1 - c_2)} - 1} \quad (6.36)$$

$$M_{mn} = j \frac{\mu_0 m}{2\pi k^2 (s_n^2 \rho_L^2 - m^2) \rho'} \frac{J_m(s_n \rho')}{J_m(s_n \rho_L)} \frac{e^{-2r_n(c_2 - z')} + 1}{1 - e^{-2r_n(c_1 - c_2)}}. \quad (6.37)$$

Perturbation due aux interfaces radiales

La Fig. 6.5 illustre la configuration du deuxième sous-problème. Nous considérons un tube fini d'épaisseur $b_2 - b_1$ et longueur $c_2 - c_1$. Le champ calculé dans le premier sous-problème est considéré comme un champ initial dans la région II. Le domaine est tronqué aux interfaces $z = 0$ et $z = h$.

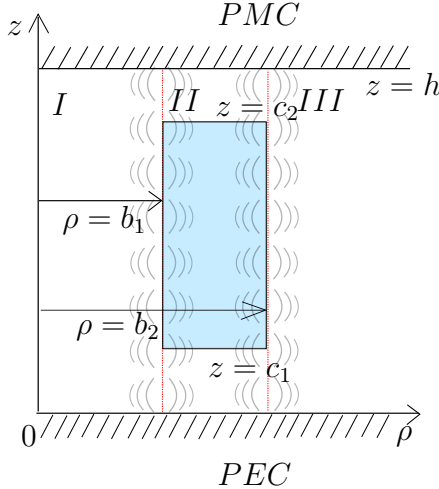


Figure 6.5: Coupe radiale d'un tube fini d'épaisseur $b_2 - b_1$ et longueur $c_2 - c_1$. Le champ calculé dans le premier sous-problème est considéré comme un champ initial dans la région II.

$$\phi^{I,sc} = \sum_{m=-\infty}^{m=\infty} \sum_{i=1}^{\infty} (L_m^{\rho<} \sin(w_n z) + A_m^{\rho<} \cos(w_n z)) I_m(w_n \rho) e^{jm\varphi} ; \quad 0 \leq z \leq h \quad (6.38)$$

$$\phi^{II,sc} = \sum_{m=-\infty}^{m=\infty} \sum_{n=1}^{\infty} (B_m^{\rho\lessgtr} \sin(p_n(h-z)) + M_m^{\rho\lessgtr} \cos(p_n(h-z))) \begin{Bmatrix} K_m(p_n \rho) \\ I_m(p_n \rho) \end{Bmatrix} e^{jm\varphi} ; \quad c_2 \leq z \leq h \quad (6.39)$$

$$W_a^{II,sc} = \sum_{m=-\infty}^{m=\infty} \sum_{n=1}^{\infty} (N_m^{\rho\lessgtr} \sin(q_n z) + C_m^{\rho\lessgtr} \cos(q_n z)) \begin{Bmatrix} K_m(p_n \rho) \\ I_m(p_n \rho) \end{Bmatrix} e^{jm\varphi} ; \quad c_1 \leq z \leq c_2 \quad (6.40)$$

$$W_b^{II,sc} = \sum_{m=-\infty}^{m=\infty} \sum_{n=1}^{\infty} (D_m^{\rho\lessgtr} \sin(\nu_n z) + O_m^{\rho\lessgtr} \cos(\nu_n z)) \begin{Bmatrix} K_m(\xi_n \rho) \\ I_m(\xi_n \rho) \end{Bmatrix} e^{jm\varphi} ; \quad c_1 \leq z \leq c_2 \quad (6.41)$$

$$\phi^{II,sc} = \sum_{m=-\infty}^{m=\infty} \sum_{n=1}^{\infty} (F_m^{\rho\lessgtr} \sin(p_n z) + E_m^{\rho\lessgtr} \cos(p_n z)) \begin{Bmatrix} K_m(p_n \rho) \\ I_m(p_n \rho) \end{Bmatrix} e^{jm\varphi} ; \quad 0 \leq z \leq c_1 \quad (6.42)$$

$$\phi^{III,sc} = \sum_{m=-\infty}^{m=\infty} \sum_{i=1}^{\infty} (Q_m^{\rho>} \sin(w_n z) + P_m^{\rho>} \cos(w_n z)) K_m(w_n \rho) e^{jm\varphi} ; \quad 0 \leq z \leq h \quad (6.43)$$

où $p_n^2 = q_n^2 + k^2$, $\xi_n^2 = \nu_n^2 + k^2$.

Comme dans les étapes précédentes, l'application des conditions PEC et PMC dans les interfaces de troncature comme indiqué dans Fig. 6.5, ainsi que la continuité du champ aux interfaces $z = c_1$ et $z = c_2$ amènent aux expressions des valeurs propres

$$w_n = \frac{(2n - 1)\pi}{2h}, \quad (6.44)$$

$$\nu_n = \frac{n\pi}{c_2 - c_1} \quad (6.45)$$

et à l'équation transcendentale

$$\frac{q_n \tan(p_n c_1) - p_n \tan(q_n c_1)}{q_n - p_n \tan(p_n(h - c_2)) \tan(q_n c_2)} = \frac{p_n + q_n \tan(p_n c_1) \tan(q_n c_1)}{p_n \tan(p_n(h - c_2)) + q_n \tan(q_n c_2)} \quad (6.46)$$

dont la solution donne les valeurs propres $p - q$.

Enfin, la continuité du champ sur les interfaces radiales du tube conduit au système d'équations suivant, dont la solution donne les coefficients modaux des potentiels.

$$\begin{aligned} w_n I'_m(w_n b) A_{mn}^{\rho <} &= -M_c(l, i)p_n \begin{Bmatrix} K'_m(p_n b_1) \\ I'_m(p_n b_1) \end{Bmatrix} C_{mn}^{\rho \leqslant} + \frac{k^2 j m}{b} M_r(l, i) \begin{Bmatrix} K_m(\xi_n b_1) \\ I_m(\xi_n b_1) \end{Bmatrix} D_{mn}^{\rho \leqslant} \\ &\quad + S_\rho(z) \end{aligned} \quad (6.47)$$

$$\begin{aligned} \frac{j m}{b} I_m(w_n b) A_{mn}^{\rho <} &= -\frac{j m}{b} M_c(l, i) \begin{Bmatrix} K_m(p_n b_1) \\ I_m(p_n b_1) \end{Bmatrix} C_{mn}^{\rho \leqslant} - k^2 M_r(l, i) \xi_n \begin{Bmatrix} K'_m(\xi_n b_1) \\ I'_m(\xi_n b_1) \end{Bmatrix} D_{mn}^{\rho \leqslant} \\ &\quad + S_\varphi(b_1, z) \end{aligned} \quad (6.48)$$

$$-w_n I_m(w_n b) A_{mn}^{\rho <} = -M_s(l, i)p_n \begin{Bmatrix} K_m(p_n b_1) \\ I_m(p_n b_1) \end{Bmatrix} C_{mn}^{\rho \leqslant} + S_z(b_1, z), \quad (6.49)$$

$$\begin{aligned} w_n I'_m(w_n b) M_{mn}^{\rho >} &= -M_c(l, i)p_n \begin{Bmatrix} K'_m(p_n b_2) \\ I'_m(p_n b_2) \end{Bmatrix} C_{mn}^{\rho \leqslant} + \frac{k^2 j m}{b} M_r(l, i) \begin{Bmatrix} K_m(\xi_n b_2) \\ I_m(\xi_n b_2) \end{Bmatrix} D_{mn}^{\rho \leqslant} \\ &\quad + S_\rho(b_2, z) \end{aligned} \quad (6.50)$$

$$\begin{aligned} \frac{j m}{b} I_m(w_n b) M_{mn}^{\rho >} &= -\frac{j m}{b} M_c(l, i) \begin{Bmatrix} K_m(p_n b_2) \\ I_m(p_n b_2) \end{Bmatrix} C_{mn}^{\rho \leqslant} - k^2 M_r(l, i) \xi_n \begin{Bmatrix} K'_m(\xi_n b_2) \\ I'_m(\xi_n b_2) \end{Bmatrix} D_{mn}^{\rho \leqslant} \\ &\quad + S_\varphi(b_2, z) \end{aligned} \quad (6.51)$$

et

$$-w_n I_m(w_n b) M_{mn}^{\rho >} = -M_s(l, i) p_n \begin{Bmatrix} K_m(p_n b_2) \\ I_m(p_n b_2) \end{Bmatrix} C_{mn}^{\rho \leqslant} + S_z(b_2, z), \quad (6.52)$$

où

$$\begin{aligned} M_c(l, i) = & \frac{2}{h} \left[-\beta_n \int_0^{c_1} \cos(p_n z) \cos(w_l z) dz - q_n \alpha_n \int_{c_1}^{c_2} \cos(q_n z) \cos(w_l z) dz \right. \\ & \left. + q_n \int_{c_1}^{c_2} \sin(q_n z) \cos(w_l z) dz - \gamma_n \int_{c_2}^h \sin(p_n(h-z)) \cos(w_l z) dz \right] \end{aligned} \quad (6.53)$$

$$\begin{aligned} M_s(l, i) = & \frac{2}{h} \left[\beta_n \int_0^{c_1} \sin(p_n z) \sin(w_l z) dz + p_n \alpha_n \int_{c_1}^{c_2} \sin(q_n z) \sin(w_l z) dz \right. \\ & \left. + p_n \int_{c_1}^{c_2} \cos(q_n z) \sin(w_l z) dz + \gamma_n \int_{c_2}^h \cos(p_n(h-z)) \sin(w_l z) dz \right] \end{aligned} \quad (6.54)$$

$$M_r(l, i) = \frac{2}{h} \left[\int_{c_1}^{c_2} \sin(\nu_n z) \cos(w_l z) dz + \delta_n \int_{c_1}^{c_2} \cos(\nu_n z) \cos(w_l z) dz \right] \quad (6.55)$$

et les termes

$$\begin{aligned} S_\rho(\rho, z) = & \frac{2}{h} [R_c^{(iv)}(-\kappa_n, w_l) P_{mn} - R_c^{(iii)}(-v_n, w_l) v_n A_{mn} + R_c^{(iii)}(v_n, w_l) v_n B_{mn} \\ & - R_c^{(ii)}(-v_n, w_l) v_n E_{mn} + R_c^{(ii)}(v_n, w_l) v_n F_{mn} + R_c^{(i)}(\kappa_n, w_l) N_{mn}] \kappa_n J'_m(\kappa_n \rho) \\ & + \frac{2k^2 jm}{\rho h} [R_c^{(iii)}(-r_n, w_l) C_{mn} + R_c^{(iii)}(r_n, w_l) D_{mn} \\ & + R_c^{(ii)}(-r_n, w_l) L_{mn} + R_c^{(ii)}(r_n, w_l) M_{mn}] J_m(s_n \rho) \end{aligned} \quad (6.56)$$

$$\begin{aligned} S_\varphi(\rho, z) = & \frac{2jm}{\rho h} [R_c^{(iv)}(-\kappa_n, w_l) P_{mn} - R_c^{(iii)}(-v_n, w_l) v_n A_{mn} + R_c^{(iii)}(v_n, w_l) v_n B_{mn} \\ & - R_c^{(ii)}(-v_n, w_l) v_n E_{mn} + R_c^{(ii)}(v_n, w_l) v_n F_{mn} + R_c^{(i)}(\kappa_n, w_l) N_{mn}] J_m(\kappa_n \rho) \\ & - \frac{2k^2}{h} [R_c^{(iii)}(-r_n, w_l) C_{mn} + R_c^{(iii)}(r_n, w_l) D_{mn} + R_c^{(ii)}(-r_n, w_l) L_{mn} \\ & + R_c^{(ii)}(r_n, w_l) M_{mn}] J'_m(s_n \rho) \end{aligned} \quad (6.57)$$

$$\begin{aligned} S_z(\rho, z) = & \frac{2}{h} [-R_s^{(iv)}(-\kappa_n, w_l) P_{mn} + R_s^{(iii)}(-v_n, w_l) \kappa_n A_{mn} + R_s^{(iii)}(v_n, w_l) \kappa_n B_{mn} \\ & + R_s^{(ii)}(-v_n, w_l) \kappa_n E_{mn} + R_s^{(ii)}(v_n, w_l) \kappa_n F_{mn} + R_s^{(iv)}(\kappa_n, w_l) N_{mn}] \kappa_n J_m(\kappa_n \rho), \end{aligned} \quad (6.58)$$

avec

$$R_s^{(i, ii, iii, iv)}(\mu, \nu) = \int_{0, c_1, z', c_2}^{c_1, z', c_2, h} e^{\mu(z-z')} \sin(\nu z) dz \quad (6.59)$$

et

$$R_c^{(i,ii,iii,iv)}(\mu, \nu) = \int_{0,c_1,z',c_2}^{c_1,z',c_2,h} e^{\mu(z-z')} \cos(\nu z) dz. \quad (6.60)$$

6.3 Signal courant de Foucault

La dernière étape pour la solution du problème CF et le calcul du signal CF. L'impédance du capteur peut être écrite comme :

$$Z = Z_0 + \Delta Z_{geom} + \Delta Z_{crack}. \quad (6.61)$$

où Z_0 est l'impédance du capteur dans le vide ($Z_0 = j\omega L$, L étant l'inductance du capteur dans le vide), ΔZ_{geom} est le changement de l'impédance due à la pièce sans défaut calculé dans le paragraphe précédent et ΔZ_{crack} est le changement de l'impédance due au défaut qu'il reste à calculer. Une fois que le champ primaire est calculé et la fonction de Green est construite, l'équation intégrale suivante est résolue

$$\mathbf{n} \cdot \mathbf{E}_0(\mathbf{r}) = -j\omega\mu_0 \int_{S_{def}} \varphi \cdot \bar{\mathbf{G}}(\mathbf{r}, \mathbf{r}') \cdot \varphi p(\mathbf{r}') dS' \quad (6.62)$$

où \mathbf{E}_0 est le champ primaire, $\varphi \cdot \bar{\mathbf{G}}(\mathbf{r}, \mathbf{r}') \cdot \varphi$ est la fonction de Green $G^{\varphi\varphi}$, $p(\mathbf{r})$ est la densité surfacique des dipôles et S_{def} est la surface du défaut. L'équation (6.62) est résolue avec la méthode des moments (MoM).

Enfin, la densité surfacique des dipôles calculée par la solution de (6.62) est utilisée pour calculer le signal CF à l'aide du théorème de réciprocité

$$I^2 \Delta Z_{crack} = - \int_{S_{def}} \mathbf{E}_0(\mathbf{r}) \cdot \mathbf{p}(\mathbf{r}) dS \quad (6.63)$$

où I est l'amplitude du courant d'excitation.

6.4 Validations numériques

Nous citons ici quelques résultats pour trois cas testés. Dans tous les cas le signal comparé est la valeur de $\Delta Z_{geom} + \Delta Z_{crack}$ du signal CF.

6.4.1 Demi-espace avec un alésage et un défaut

Le premier cas testé est le cas d'un demi-espace conducteur avec un alésage et un défaut (Fig. 6.6). Les paramètres de la simulation sont donnés dans la Table 6.1

Le signal CF calculé avec l'approche présentée est comparé avec des résultats de la méthode VIM-SIM (logiciel CIVA) ainsi qu'avec la méthode d'éléments finis (FEM - logiciel COMSOL).

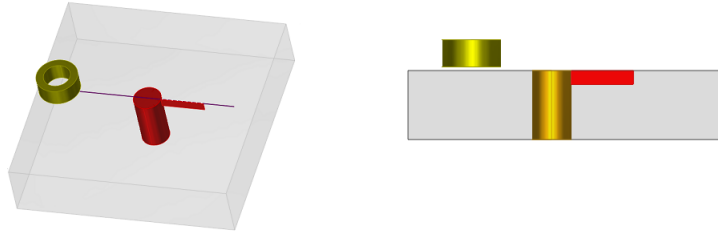


Figure 6.6: Demi-espace avec un alésage et un défaut.

Table 6.1: Paramètres de simulation pour un demi-espace conducteur avec un alésage et un défaut fin

	Coil	Halfspace	Crack	
Inner diameter	6 mm	Conductivity	10 MS/m	
Outer diameter	9.3 mm	Hole diameter	6.25 mm	
Length	4 mm		Length	9.8 mm
Turns	336		Depth	2 mm
Lift-off	0.5 mm		Opening	0.1 mm

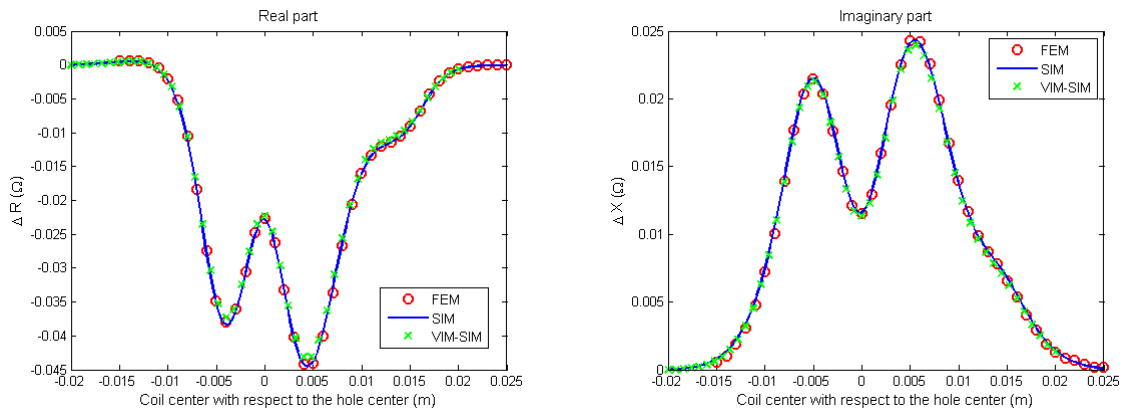


Figure 6.7: Variation de l'impédance vs. position du capteur suivant un scan sur l'ensemble alésage-défaut.

6.4.2 Plaque finie avec un alésage et un défaut

Le deuxième cas testé est le cas d'une plaque conductrice et infinie avec un alésage et un défaut (Fig. 6.8). Les paramètres de la simulation sont donnés dans Table 6.2.

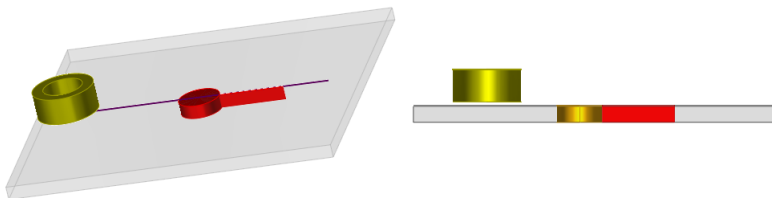


Figure 6.8: Plaque d'épaisseur 2 mm avec un alésage et un défaut.

Table 6.2: Paramètres de simulation pour le problème benchmark 2013 de WFNDEC

Coil	Piece		Crack		
Inner diameter	12 mm	Conductivity	17.34 MS/m	Length	9.8 mm
Outer diameter	24 mm	Thickness	2 mm	Depth	2 mm
Length	4 mm	Hole diameter	20 mm	Opening	0.234 mm
Turns	1650				
Lift-off	1.08 mm				

Les résultats de la méthode SIM sont maintenant comparés avec des mesures expérimentales du problème de Benchmark 2013 de WFNDEC (World Federation of Non-Destructive Evaluation Centers).

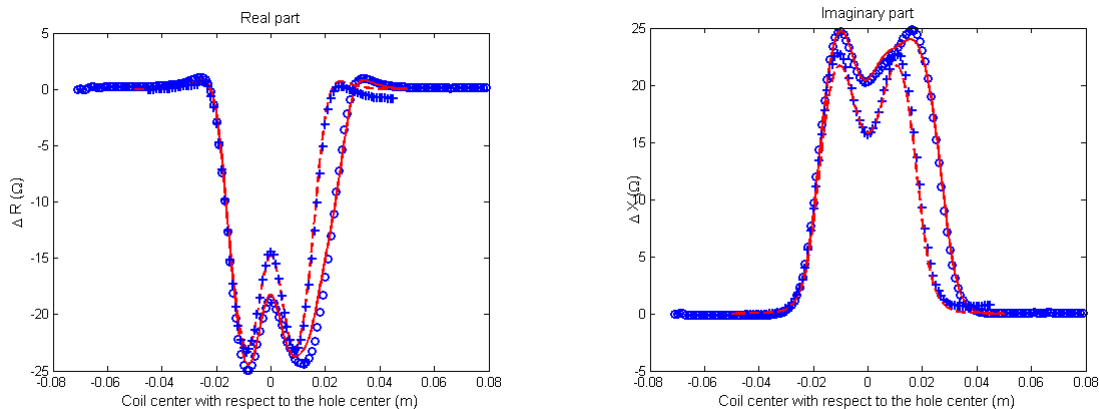


Figure 6.9: Résultats de la méthode SIM et mesures expérimentales de la variation de l'impédance vs. la position du capteur pour la configuration de Table 6.2. La courbe pleine représente les résultats de SIM pour le signal total, la ligne pointillée correspond au signal de l'alésage. Les résultats de SIM sont comparés avec des résultats expérimentaux dans les deux cas (cercles et croix, respectivement).

6.4.3 Tube infini avec un défaut à son bord

Le dernier cas testé est le cas d'un tube conducteur et infini avec un défaut à son bord (Fig. 6.10). Les paramètres de la simulation sont donnés dans Table 6.3.

Table 6.3: Paramètres de simulation pour un tube semi-infini avec un défaut à son bord.

Coil	Piece		Crack		
Inner diameter	3 mm	Conductivity	10 MS/m	Length	3 mm
Outer diameter	5 mm	Thickness	5 mm	Depth	4 mm
Length	4 mm	Hole diameter	6.2 mm	Opening	0.1 mm
Turns	336				
Offset	0.0 mm				

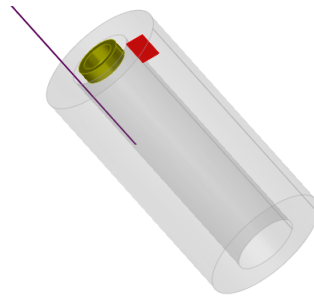


Figure 6.10: Tube d'épaisseur 5 mm avec un défaut fin de dimensions 3 mm x 4 mm situé au bord du tube.

Les résultats de la méthode SIM sont comparés avec ceux de la méthode FEM simulés avec le logiciel COMSOL (6.11).

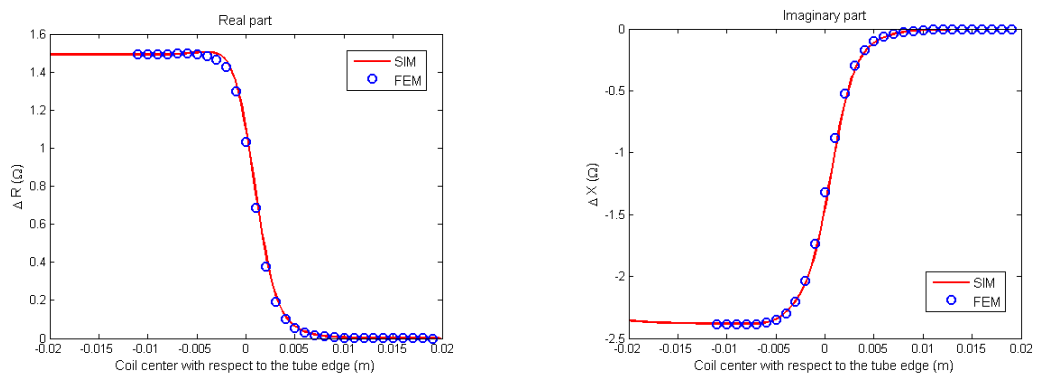


Figure 6.11: Variation de l'impédance vs. position du capteur suivant un scan dans le tube. La fréquence opérationnelle est 10 kHz.

6.5 Conclusion

Un modèle de l'inspection en courants de Foucault de pièces cylindriques a été présenté. Le modèle suit une approche d'équation intégrale qui se compose de trois étapes. Le calcul du champ émis par un capteur dans un domaine en présence d'une pièce cylindrique sans défaut, la construction de l'opérateur de Green attribué à la pièce inspectée et la solution de l'équation intégrale décrivant le problème et le calcul du signal CF avec le théorème de réciprocité. Les résultats obtenus ont été comparés avec des résultats provenant de simulations des modèles FEM et VIM-SIM ainsi que des mesures expérimentales. Les résultats de l'approche présentée et ceux des autres modèles ou des mesures concordent. Le modèle présente des temps de calcul moins élevés par rapport aux autres modèles. Un autre avantage de ce modèle par rapport aux approches existantes est la possibilité d'inspecter les pièces dans l'alésage.

Bibliography

- [AMW81] A. Auld, F. Muennemann, and D. Winslow. Eddy current probe response to open and closed surface flaws. *J Nonddestruct Eval*, 2(1):1–21, March 1981.
- [AR97] R. Albanese and G. Rubinacci. Finite Element Methods for the Solution of 3d Eddy Current Problems. *Advances in Imaging and Electron Physics*, 102:1–86, 1997.
- [AS65] M. Abramowitz and I. Stegun, editors. *Handbook of Mathematical Functions: with Formulas, Graphs, and Mathematical Tables*. Dover Publications, New York, NY, June 1965.
- [Bal89] C. Balanis. *Advanced Engineering Electromagnetics*. Wiley, New York, May 1989.
- [BNH94] J. Bowler, S. Norton, and D. Harrison. Eddycurrent interaction with an ideal crack. II. The inverse problem. *Journal of Applied Physics*, 75(12):8138–8144, June 1994.
- [Bow94] J. Bowler. Eddy-current interaction with an ideal crack. I. The forward problem. *Journal of Applied Physics*, 75(12):8128–8137, June 1994.
- [BT05] J. Bowler and T. Theodoulidis. Eddy currents induced in a conducting rod of finite length by a coaxial encircling coil. *Journal of Applied Physics*, 38(16):2861–2868, August 2005.
- [BT06] J. Bowler and T. Theodoulidis. Coil impedance variation due to induced current at the edge of a conductive plate. *Journal of Physics D: Applied Physics*, 39(13):2862–2868, July 2006.
- [BT09] J. Bowler and T. Theodoulidis. Boundary element calculation of eddy currents in cylindrical structures containing cracks. *IEEE Transactions on Magnetics*, 45(3):1012–1015, March 2009.
- [BTP12] J. Bowler, T. Theodoulidis, and N. Poulakis. Eddy-current probe signals due to a crack at a right-angled corner. *IEEE Transactions on Magnetics*, 48(12):4735–4746, 2012.

- [BTXJ12] J. Bowler, T. Theodoulidis, H. Xie, and Y. Ji. Evaluation of Eddy-Current Probe Signals Due to Cracks in Fastener Holes. *IEEE Transactions on Magnetics*, 48(3):1159–1170, March 2012.
- [Che95] W. Chew. *Waves and Fields in Inhomogenous Media*. IEEE Press, NY, 1995.
- [DL67] L. Delves and J. Lyness. A numerical method for locating the zeros of an analytic function. *Math. Comp.*, 21(100):543–560, 1967.
- [Dun85] W. Dunbar. The volume integral method of eddy current modeling. *J Non-destruct Eval*, 5(1):9–14, March 1985.
- [Dun88] W. Dunbar. The volume integral method of eddy-current modeling: Verification. *J Nondestruct Eval*, 7(1-2):43–54, June 1988.
- [FN93] M. Filtz and A. Nethe. Bemerkungen zur Lösung des dreidimensionalen Wirbelstromproblems in Kreiszylindern endlicher Länge. *Archiv für Elektrotechnik*, 76(3):195–200, May 1993.
- [Gri99] D. Griffiths. *Introduction to Electrodynamics*. Prentice Hall, Upper Saddle River, N.J, January 1999.
- [Jac98] J. Jackson. *Classical Electrodynamics*. Wiley, New York, 3rd edition, August 1998.
- [KA04] J. Knopp and J. Aldrin. Numerical and Experimental Study of Eddy Current Crack Detection around Fasteners in MultiLayer Structures. *AIP Conference Proceedings*, 700(1):336–343, 2004.
- [KA09] J. Knopp and J. Aldrin. Computational methods in eddy current crack detection at fastener sites in multi-layer structures. *Nondestructive Testing and Evaluation*, 24(1):103–120, 2009.
- [KLL14] J. Kim, M. Le., and J. Lee. Non-destructive evaluation of far-side corrosion around the multi-layered rivet by using the solid-state hall sensor array. In *IEEE Sensors Applications Symposium (SAS)*, pages 42–46, 2014.
- [Lyn67] J. Lyness. Numerical algorithms based on the theory of complex variable. In *Proceedings of the 1967 22nd National Conference*, ACM '67, pages 125–133, New York, 1967.
- [MRT⁺13] R. Miorelli, C. Reboud, T. Theodoulidis, N. Poulakis, and D. Lesselier. Efficient modeling of ECT signals for realistic cracks in layered half-space. *IEEE Transactions on Magnetics*, 49(6):2886–2892, June 2013.

- [MRT14a] R. Miorelli, C. Reboud, and T. Theodoulidis. 2013 eddy current benchmark problem: Solution via a coupled integral approach. In *AIP Conference Proceedings*, volume 1581, pages 2086–2092. AIP Publishing, February 2014.
- [MRT⁺14b] R. Miorelli, C. Reboud, T. Theodoulidis, J. Martinos, N. Poulakis, and D. Lesselier. Coupled approach VIM-BEM for efficient modeling of ECT signal due to narrow cracks and volumetric flaws in planar layered media. *NDT & E International*, 62:178–183, March 2014.
- [MRTV08] M. Morozov, G. Rubinacci, A. Tamburrino, and S. Ventre. Evaluation of subsurface cracks in riveted aluminium joints using industrial eddy current instrumentation. In *Electromagnetic Non-Destructive Evaluation (XI), Studies in Applied Electromagnetics and Mechanics*, volume 31, pages 187–194. IOS Press, 2008.
- [PCP⁺08] S. Paillard, Y. Choua, G. Pichenot, Y. Bihan, M. Lambert, H. Voillaume, and N. Dominguez. Modelling of flawed riveted structure for EC inspection in aeronautics. In *Electromagnetic Non-Destructive Evaluation (XI), Studies in Applied Electromagnetics and Mechanics*, volume 31, pages 217–224. IOS Press, 2008.
- [PL06] J. Pávó and D. Lesselier. Calculation of eddy current testing probe signal with global approximation. *IEEE Transactions on Magnetics*, 42(4):1419–1422, 2006.
- [SPL⁺08] A. Skarlatos, G. Pichenot, D. Lesselier, M. Lambert, and B. Duchene. Electromagnetic modeling of a damaged ferromagnetic metal tube by a volume integral equation formulation. *IEEE Transactions on Magnetics*, 44(5):623–632, 2008.
- [ST12] A. Skarlatos and T. Theodoulidis. Solution to the eddy-current induction problem in a conducting half-space with a vertical cylindrical borehole. *Proceedings of the Royal Society of London A: Mathematical, Physical and Engineering Sciences*, 468(2142):1758–1777, June 2012.
- [ST15] A. Skarlatos and T. Theodoulidis. Calculation of the eddy-current flow around a cylindrical through-hole in a finite-thickness plate. *IEEE Transactions on Magnetics*, PP(99):1–1, 2015.
- [Str41] A. J. Stratton. *Electromagnetic Theory*. McGraw - Hill, New York, 1941.
- [TB08] T. P. Theodoulidis and J. R. Bowler. Impedance of an induction coil at the opening of a borehole in a conductor. *Journal of Applied Physics*, 103(2):1–9, January 2008.

- [The10] T. Theodoulidis. Developments in efficiently modelling eddy current testing of narrow cracks. *NDT & E International*, 43(7):591–598, 2010.
- [TK06] T. Theodoulidis and E. Kriegis. *Eddy Current Canonical Problems*. Tech Science Press, Forsyth, GA, April 2006.
- [UM04] S. Udpa and P. Moore. *Nondestructive Testing Handbook*, volume 5. American Society for Non Destructive Testing, New York, 2004.
- [YZD⁺12] G. Yang, Z. Zeng, Y. Deng, X. Liu, L. Udpa, A. Tamburrino, and S. S. Udpa. 3D EC-GMR sensor system for detection of subsurface defects at steel fastener sites. *NDT & E International*, 50:20–28, 2012.

Titre : Modélisation du CND par courants de Foucault des pièces cylindriques avec des discontinuités axiales à l'aide d'une formulation intégrale dédiée

Mots clés : CND, courants de Foucault, surface integral method (SIM), TREE, pièces alésées, tubes

Résumé : Le contrôle non destructif (CND) de pièces pour des applications dans l'industrie a mené au besoin de modèles rapides et précises. Tels modèles servent au développement des méthodes d'inspection, à l'optimisation des capteurs utilisés aux essais, à l'évaluation des courbes de Probabilité de Détection (POD) ainsi qu'à la caractérisation de défauts. Cette thèse se focalise au CND par Courants de Foucault (CF) de pièces cylindriques avec des discontinuités selon z et contenant un défaut fin. Un modèle pour l'inspection de telles pièces a été développé afin de traiter des applications comme l'inspection des pièces alésées trouvées en aéronautique et des tubes des générateurs de vapeur utilisés dans l'industrie nucléaire. Ce modèle est basé sur une formulation d'équation intégrale. Plus précisément, la variation de l'impédance du capteur, dit signal CF, est calculée à partir d'une équation intégrale sur la surface du défaut. La formulation suivie est basée sur la méthode d'intégration surfacique (SIM). Cette formulation nécessite, d'un côté, le calcul du champ électrique en absence du défaut et, de l'autre côté, l'expression d'une fonction de Green qui correspond à la géométrie de la pièce sans défaut.

Les deux problèmes électromagnétiques sont résolus en utilisant la méthode Truncation Region Eigenfunction Expansion (TREE). La méthode TREE est un outil performant pour la résolution des problèmes électromagnétiques qui prend en compte la décroissance rapide de l'intensité du champ afin de tronquer le domaine d'intérêt à une distance, où le champ est négligeable. Le modèle est validé en comparant le signal CF calculé avec des résultats obtenus par une approche combinant la méthode d'intégration volumique (VIM) et SIM, dite l'approche VIM-SIM (implémentée dans la plateforme CIVA) ainsi qu'avec le modèle d'éléments finis (FEM). Nous avons traité trois configurations différentes : un demi-espace conducteur alésé avec un défaut fin, une plaque conductrice avec un alésage et un défaut, et un tube semi-infini avec un défaut fin à la proximité de son bord. La comparaison des résultats montre un très bon accord entre les trois modèles. Le temps de calcul avec le modèle SIM est considérablement inférieur aux temps de calcul des autres modèles. En outre, le modèle SIM donne la possibilité d'effectuer le balayage du capteur dans le tube ou l'alésage dans le cas des pièces alésées.

Title : Eddy-current testing modeling of axisymmetric pieces with discontinuities along the axis by means of an integral equation approach

Keywords : NDT, eddy-currents, surface integral method (SIM), TREE, riveted pieces, tubes

Abstract: Nondestructive Testing (NDT) of parts for industrial applications such as in nuclear and aeronautical industry has led to the need for fast and precise models. Such models are useful for the development of the inspection methods, the optimisation of probes, the evaluation of the Probability of Detection (POD) curves or for the flaw characterisation.

This PhD thesis focuses on the eddy-current NDT of layered cylindrical pieces with discontinuities in the z direction and containing a narrow crack. A model for the inspection of such pieces is developed in order to be applied on the inspection of fastener holes met in aeronautics and of steam generator tubes in nuclear sector. The model is based on an integral equation formalism. More precisely, for the calculation of the impedance change one needs to solve an integral equation over the surface of the narrow crack, which is represented by a surface electric dipole distribution. This is the method known as surface integration method (SIM). This formulation requires, on the one hand, the calculation of the electric field in the absence of the flaw, the so-called primary field, and, on the other hand, the Green's function expression corresponding to the geometry of the flawless piece.

Both electromagnetic problems are solved by means of the Truncation Region Eigenfunction Expansion (TREE) method. The TREE method is a powerful tool for the solution of electromagnetic problems which uses the rapid decrease of the field in order to truncate the region of interest at a distance where the field is negligible.

The model is validated by comparing the results of the coil impedance variation with those obtained by an approach that combines the volume integral method (VIM) with SIM, known as VIM-SIM method, implemented in the commercial software CIVA and the finite element method (FEM) implementation in COMSOL software. Three different configurations have treated. The more general geometry of a conducting half-space with a borehole, a conducting plate with a borehole and a crack and a conducting semi-infinite tube with a crack near the edge. The results of the three models show good agreement between them. The computational time of the SIM model is significantly lower compared to previous models. Furthermore, another advantage of the SIM model is that it provides the possibility of a scan inside the borehole.

